Alma Mater Studiorum – Università di Bologna

School of Science
Department of Physics and Astronomy
Master Degree Programme in Astrophysics and Cosmology

X-ray View of Hyper-Luminous Quasars at z ~ 2 – 4: the WISSH project

Graduation Thesis

Presented by:
Cecilia Degli Agosti

Supervisor:
Chiar.mo Prof. Cristian Vignali

Co-supervisor:
Dr. Enrico Piconcelli

Academic year 2022 – 2023

[...] Perché siamo carne da accarezzare
E progetti possibili da realizzare [...]

Dal tuo sentire al mio pensare, Fiorella Mannoia

Abstract

Accreting supermassive black holes (SMBHs) are known to be among the most powerful objects in the Universe. This is especially true if we look back to the *cosmic noon* era, i.e. at redshifts $z \approx 2-4$, when the BH accretion rate density is at its maximum. At this epoch, Hyper-Luminous Quasi-Stellar Objects (HyLQSOs) shine at the brightest end of the quasar luminosity function ($L_{bol} >$ a few 10^{47} erg s^{-1}) and are expected to produce the most energetic multiphase winds at any scale, as their kinetic power is thought to increase with L_{bol}. It is generally accepted that such powerful outflows provide the most efficient feedback that impacts the host galaxy evolution, coupling with the ISM and possibly quenching star formation. The cosmic noon is, therefore, the golden epoch of the AGN-galaxy co-evolution; as such, it is fundamental to deepen our knowledge of the HyLQSOs, where any feedback effect is at its maximum.

The low flux (due to their distance) and low number density of these extreme objects make it difficult to pursue a systematic study. Thus, the spectral and wind properties of HyLQSOs are still poorly investigated. In this context, the WISSH project aims at filling this observational gap through a proper investigation of the multi-wavelength properties of 85 WISE/SDSS selected Type 1 (i.e. unobscured) HyLQSOs at the cosmic noon. The overall work on WISSH sources, including the present thesis project, leads to gather an unprecedent sample of HyLQSOs at the cosmic noon with a multi-wavelength coverage.

The present thesis project focuses on the X-ray properties of the WISSH sample. Specifically, we analyse new proprietary Chandra data for 44 sources, along with archival Chandra and XMM-Newton data for the remaining objects. Once quasar detection is carried out, the observed $0.5-10$ keV flux is derived. The slope of the primary power-law (Γ) and constraints on possible intrinsic column density (N_H) are measured for the sources with a sufficient number of counts. The X-ray spectral index is broadly consistent with the expected $\Gamma \approx 1.8-2$. About 24 % of the sources (both BAL - Broad Absorption Line - and non-BAL) for which N_H can be estimated exhibits at least moderate obscuration ($N_H \geq 10^{22}$ cm^{-2}). Among

BAL QSOs, this result is justified by the presence of wind absorption; however, it is unexpected in Type 1 non-BAL objects. The quasars of the sample have an intrinsic $2-10$ keV luminosity in the range $L_{2-10} \approx 7 \times 10^{43} - 2 \times 10^{46}$ erg s^{-1}.

All of these results must be considered in a broad-band perspective, as data in different spectral bands are available for most of the WISSH sources. In particular, the bolometric correction (k_{bol}) and X-ray - to - optical index (α_{OX}) are derived from the bolometric (L_{bol}) and monochromatic 2500 Å (L_{2500}) luminosities.

$$k_{bol} = \frac{L_{bol}}{L_{2-10}} \qquad \alpha_{OX} = \frac{\mathrm{Log}(L_{2\,keV}/L_{2500})}{\mathrm{Log}(\nu_{2\,keV}/\nu_{2500})}$$

where $L_{2\,keV}$ is the monochromatic luminosity at 2 keV, and $\nu_{2\,keV}$ and ν_{2500} are the frequencies corresponding to 2 keV and 2500 Å, respectively. The comparison between the observed ($\alpha_{OX,obs}$) and expected (from Martocchia et al. 2017 best fit relation - $\alpha_{OX,M17}$) X-ray - to - optical indices leads to the definition of $\Delta(\alpha_{OX}) = \alpha_{OX,obs} - \alpha_{OX,M17}$.

- Studying the $L_{bol} - k_{bol}$, $L_{2500} - \alpha_{OX}$ and $L_{6\,\mu m} - L_{2-10}$ planes, WISSH QSOs arrange anomalously with respect to literature relations (e.g. Duras et al. 2020, Martocchia et al. 2017, Stern 2015), i.e. covering a wide range of k_{bol}, α_{OX} and L_{2-10} for a given bolometric or monochromatic luminosity. The large spread of X-ray properties is in contrast with the homogeneity of WISSH QSOs in terms of L_{bol} and optical classification. This evidence highlights a different coupling in the accretion disk - corona, possibly occurring in hyper-luminous objects;

- About 22 % of WISSH sources can be classified as "X-ray weak" quasars, i.e. characterised by a lower relative contribution of the X-ray emission to the bolometric luminosity compared to lower-luminosity samples. This result is based on $\Delta(\alpha_{OX})$ falling below the adopted threshold $\Delta(\alpha_{OX}) = -0.2$ by Luo et al. 2015. As expected from literature (e.g. Brandt et al. 2000), the majority of X-ray weak sources are BAL QSOs.

For the sources with an available Hβ-derived black hole mass estimate, Eddington ratios $\lambda_{Edd} = L_{bol}/L_{Edd}$ are evaluated in the range $\sim 0.1 - 2.8$ (i.e. highly accreting).

- Previously found correlations with the spectral index (e.g. Brightman et al. 2013, Liu et al. 2021, Trakhtenbrot et al. 2017) do not seem to work at $\lambda_{Edd} \gtrsim 1$, where data are highly dispersed, thus preventing an immediate derivation of Γ from the Eddington ratio;

- Comparing $\lambda_{\rm Edd}$ and $N_{\rm H}$, WISSH blue quasars emerge to occupy the "forbidden region" of the plane (i.e. high-$\lambda_{\rm Edd}$/high-$N_{\rm H}$ conditions), where intense feedback outflows are expected to occur, which set QSOs free from obscuring material. Such transitional state is identified by Fabian et al. 2008, and is typically associated with dust-obscured red sources. Thus, a different origin of the obscuration is suggested between blue and red sources.

The complete analysis of the X-ray data presented in this thesis represents a fundamental step in the study of AGN nuclear processes and their relation with feedback impacting the host galaxy. Future works will focus on drawing a coherent picture of quasar nuclear activity, linking multi-wavelength properties. Moreover, possible cosmological evolution of the feedback and quasar emission will be investigated through the comparison of WISSH sample with higher-redshift ones (mainly, the HYPERION quasar sample at $z > 6$ - Zappacosta et al. 2023). Finally, deeper X-ray observations of the WISSH sample are envisaged, in order to perform a more accurate X-ray spectral fitting and possibly detect UFOs (Ultra Fast Outflows) and determine their physical properties.

The thesis is organised as follows. In Chapter 1 the AGN phenomenon is presented in its emission and feedback aspects, along with its classification; Chapter 2 reports an overview of the results published so far on WISSH quasars; XMM-Newton and Chandra are introduced in Chapter 3, along with data reduction; in Chapter 4 WISSH X-ray data and their analysis are described; the results are presented in Chapter 5, with the derivation of various fundamental parameters ($k_{\rm bol}$, $\alpha_{\rm OX}$ and $\lambda_{\rm Edd}$).

Sommario

I buchi neri supermassicci (SMBH) in accrescimento sono tra gli oggetti più potenti dell'universo, in particolare se si fa riferimento al *cosmoc noon*, ovvero $z \approx 2-4$, quando la densità del tasso di accrescimento è massima. A quest'epoca, gli Hyper-Luminous Quasi-Stellar Objects (HyLQSO) brillano all'estremo più luminoso della funzione di luminosità dei quasar ($L_{bol} >$ qualche 10^{47} erg s^{-1}) e si prevede che producano i venti multifase più energetici a tutte le scale, poiché ci si aspetta che la loro potenza cinetica cresca con L_{bol}. È generalmente accettato che outflow così potenti forniscano feedback efficiente che impatta sull'evoluzione della galassia ospite, accoppiandosi con l'ISM ed eventualmente arrestando la formazione stellare. Il cosmic noon è dunque l'epoca d'oro della co-evoluzione AGN-galassia; in quanto tale, è fondamentale approfondire la nostra conoscenza sugli HyLQSO, dove qualsiasi effetto del feedback è massimo.

Il ridotto flusso (a causa della distanza) e densità numerica di queste sorgenti estreme rendono difficile perseguirne uno studio sistematico. Dunque, le proprietà spettrali e dei venti degli HyLQSO sono ancora poco indagate. In questo contesto, il progetto WISSH si propone di riempire il vuoto osservativo attraverso un adeguato studio delle proprietà multi-banda di 85 HyLQSO di tipo 1 (ovvero, non oscurati) al cosmic noon, selezionati nei cataloghi WISE e SDSS. Il lavoro complessivo sulle sorgenti WISSH, compresa la presente tesi, portano a comporre un campione senza precedente di HyLQSO al cosmic noon con una copertura multi-banda.

Il presente progetto di tesi si concentra sulle proprietà X-ray di tale campione: vengono analizzati nuovi dati Chandra di proprietà per 44 sorgenti, e dati Chandra e XMM-Newton di archivio per quelle rimanenti. Una volta verificata la detection del quasar, viene derivato il flusso osservato a $0.5-10$ keV. La pendenza della legge di potenza primaria (Γ) e i vincoli su eventuali densità di colonna intrinseche (N_H) vengono misurati per le sorgenti con un sufficiente numero di conteggi. L'indice spettrale X-ray è in generale consistente con quanto aspettato ($\Gamma \approx 1.8-2$). Circa il 24 % delle sorgenti (sia BAL - Broad Absorption Line - che non-BAL) per cui è possibile ottenere una stima di N_H mostra un livello di oscuramento almeno

moderato ($N_H \geq 10^{22}$ cm^{-2}). Tra i BAL QSO, questo risultato è giustificato dalla presenza di assorbimento da parte dei venti; tuttavia, non è aspettato in oggetti non-BAL di tipo 1. I quasar osservati hanno una luminosità intrinseca a $2-10$ keV nell'intervallo $L_{2-10} \approx 7 \times 10^{43} - 2 \times 10^{46}$ erg s^{-1}.

Tutti questi risultati devono essere valutati in una prospettiva multi-banda, poichè per la maggior parte delle sorgenti WISSH sono disponibili dati in diverse bande spettrali. In particolare, conoscendo la luminosità bolometrica (L_{bol}) e monocromatica a 2500Å (L_{2500}), si derivano la correzione bolometrica (k_{bol}) e l'indice X-ray - a - ottico (α_{OX}).

$$k_{bol} = \frac{L_{bol}}{L_{2-10}} \qquad \alpha_{OX} = \frac{\mathrm{Log}(L_{2\,keV}/L_{2500})}{\mathrm{Log}(\nu_{2\,keV}/\nu_{2500})}$$

dove $L_{2\,keV}$ è la luminosità monocromatica a 2 keV, e $\nu_{2\,keV}$ e ν_{2500} sono le frequenze corrispondenti a 2 keV e 2500 Å, rispettivamente. Attraverso il confronto tra i valori osservati ($\alpha_{OX,obs}$) e aspettati (dalla relazione di best fit di Martocchia et al. 2017 - $\alpha_{OX,M17}$) dell'indice X-ray - a - ottico, si definisce $\Delta(\alpha_{OX}) = \alpha_{OX,obs} - \alpha_{OX,M17}$.

- Studiando i piani $L_{bol} - k_{bol}$, $L_{2500} - \alpha_{OX}$ e $L_{6\,\mu m} - L_{2-10}$, i quasar WISSH si dispongono in modo anomalo rispetto alle relazioni di letteratura (e.g. Duras et al. 2020, Martocchia et al. 2017, Stern 2015), coprendo un ampio intervallo di k_{bol}, α_{OX} e L_{2-10} per una data luminosità bolometrica o monocromatica. Ciò evidenzia un diverso accoppiamento tra il disco di accrescimento e la corona, che potrebbe verificarsi negli HyLQSO;

- Circa il 22 % delle sorgenti WISSH possono essere classificate come "X-ray weak", ovvero caratterizzate da un contributo relativo dell'emissione X-ray alla luminosità bolometrica che è minore rispetto a campioni di più bassa luminosità. Ciò si basa sui valori di $\Delta(\alpha_{OX})$, che ricadono al di sotto della soglia stabilita di $\Delta(\alpha_{OX}) = -0.2$ (Luo et al. 2015). Come aspettato dalla letteratura (e.g. Brandt et al. 2000), la maggior parte dei quasar X-ray weak sono BAL.

Per le sorgenti di cui è disponibile una stima della massa del buco nero derivata da Hβ, il rapporto di Eddington $\lambda_{Edd} = L_{bol}/L_{Edd}$ viene stimato in un intervallo $\sim 0.1 - 2.8$ (ovvero un elevato rate di accrescimento).

- Le correlazioni precedentemente trovate con l'indice spettrale (e.g. Brightman et al. 2013, Liu et al. 2021, Trakhtenbrot et al. 2017) non sembrano sussistere a $\lambda_{Edd} \gtrsim 1$, dove i dati sono molto dispersi. Ciò impedisce un'immediata derivazione di Γ dal rapporto di Eddington;

- Confrontando $\lambda_{\rm Edd}$ e $N_{\rm H}$, emerge che i quasar blu si trovano nella "regione proibita" del piano (corrispondente a elevato $\lambda_{\rm Edd}$ e $N_{\rm H}$), dove è aspettato che si manifestino intensi outflow. Tale fase di transizione è stata identificata da Fabian et al. 2008, ed è tipicamente associata alle sorgenti rosse. Pertanto, si suggerisce una diversa origine dell'oscuramento tra sorgenti blu e rosse.

L'analisi completa dei dati X-ray presentata in questa tesi rappresenta un passo fondamentale nello studio dei processi nucleari degli AGN e della loro relazione con il feedback che influenza la galassia ospite. I lavori futuri si concentreranno sul delineare un disegno coerente dell'attività nucleare dei quasar, collegando proprietà multi-banda. In aggiunta, si investigherà una possibile evoluzione cosmologica del feedback e dell'emissione dei quasar attraverso il confronto del campione WISSH con altri a più alto redshift (principalmente, il campione di quasar HYPERION a $z > 6$ - Zappacosta et al. 2023). Infine, si prospettano osservazioni X-ray più profonde del campione WISSH, al fine di eseguire un fit spettrale X-ray più accurato ed eventualmente rilevare gli UFO (Ultra Fast Outflows) e determinarne le proprietà fisiche.

La presente tesi è organizzata come segue. Nel Capitolo 1 viene presentato il fenomeno degli AGN dal punto di vista dell'emissione e del feedback, assieme alla sua classificazione; il Capitolo 2 riporta un sommario dei risultati finora pubblicati sui quasar WISSH; XMM-Newton e Chandra vengono introdotti nel Capitolo 3, assieme alla rispettiva riduzione dati; nel Capitolo 4 sono descritti i dati X-ray delle sorgenti WISSH e la loro analisi; i risultati di tale analisi vengono presentati nel Capitolo 5, con la derivazione di vari parametri fondamentali ($k_{\rm bol}$, $\alpha_{\rm OX}$ and $\lambda_{\rm Edd}$).

Contents

1

Introduction

Supermassive black holes (SMBHs - $M_{BH} \geq 10^6\ M_\odot$) found in the central regions of galaxies started being seriously investigated in 1963, with the famous article by Schmidt 1963, where the discovery of the first QUASi-stellAR object (quasar) was presented. Although previous observations (e.g. Seyfert 1963, Bolton et al. 1949, Baade et al. 1954) of what would now be called Active Galactic Nuclei (AGN) had been done, they were never recognised as powerful extra-galactic sources. Since then, huge advances have been done: nowadays, AGN sustain a dynamic and pioneering research field, involving institutes and scholars from all-over the world. Moreover, a various "zoo" of AGN manifestations is now known.

As their name says, Active Galactic Nuclei are exceptionally luminous galactic central regions, often outshining the host galaxy itself. Nonetheless, they constitute about $1 - 10\,\%$ of all galaxies. Their emission is powered by accretion on SMBHs and can reach bolometric luminosities up to $L_{bol} \sim 10^{48}\ \mathrm{erg\,s^{-1}}$, making them the most energetic non-explosive sources in the Universe. AGN radiation spans the whole electromagnetic spectrum (Padovani et al. 2017), covering about 20 orders of magnitude in frequency.

1.1 AGN Spectral Energy Distribution

Different wavelengths shed light on various physical phenomena occurring in active galactic centers. A complete Spectral Energy Distribution (SED), from radio to γ-ray frequencies, where emission components are individually shown, is reported in Figure 1.1.

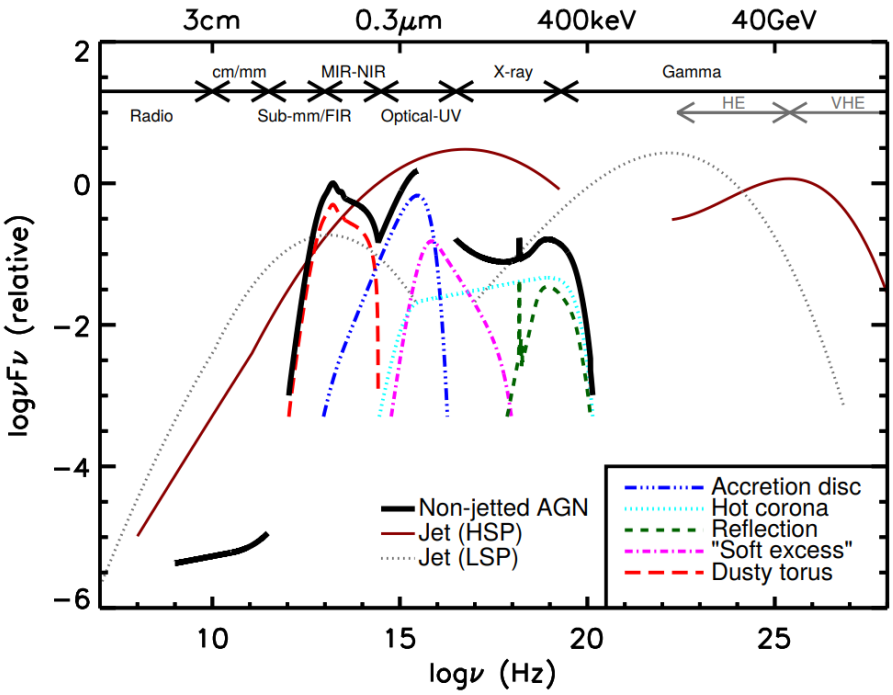

Figure 1.1: From Padovani et al. 2017 - A schematic representation of an AGN spectral energy distribution (SED), loosely based on the observed SEDs of non-jetted quasars (e.g. Elvis et al. 1994, Richards et al. 2006). The black solid curve represents the total emission and the various coloured curves (shifted down for clarity) represent the individual components. The intrinsic shape of the SED in the mm-far infrared (FIR) regime is uncertain; however, it is widely believed to have a minimal contribution (to the overall galaxy SED) compared to star formation (SF), with the exception of the most intrinsically luminous quasars and powerful jetted AGN. The primary emission from the AGN accretion disk peaks in the optical/UV region. The jet SED is also shown for a High Synchrotron Peaked blazar (HSP, based on the SED of Mrk 421) and a Low Synchrotron Peaked blazar (LSP, based on the SED of 3C 454.3).

1.1.1 Optical/UV emission from the accretion disk

The main contribution to AGN luminosity, together with X-ray one, is optical/UV black body emission from accretion disk (AD). It is represented in Figure 1.1 by the blue dash-dotted curve, often renamed “big blue bump”.

Matter accreting on SMBHs is forced into a disk-like shape by viscous friction acting between particles, although the physical mechanism responsible for viscosity is still unclear. Viscous torque determines angular momentum transport outward, allowing therefore gas particles to slide towards the central compact object. Such inward motion implies matter’s potential energy to be converted into kinetic energy. As gravitational force is much larger than viscous one, the disk is almost Keplerian and circles differentially. Consequently, rotation slows down at increasing distances from the black hole and kinetic energy is transformed into internal energy (i.e. heat) by internal friction between different annuli.

Following Shakura and Sunyaev 1973 model for an optically thick and geometrically thin (vertical size $\ll$ radial size) accretion disk, its temperature dependence on radius (T(r)) is

$$\mathrm{T(r)} \propto \mathrm{r}^{-\frac{3}{4}} \tag{1.1}$$

thus, AD emission increases inwards. The resulting spectrum can be considered the superposition of black bodies consisting of rings at different temperatures. Moreover,

$$\mathrm{T(r)} \propto \mathrm{M}_{\mathrm{BH}}^{-\frac{1}{4}} \tag{1.2}$$

thus, given the typical SMBH mass, thermal disk mostly emits in the optical/UV frequency range. The AD structure presented so far corresponds to high accretion rate and efficient radiation processes.

On the other hand, radiatively inefficient accretion flows result in ADAF (Advection-Dominated Accretion Flow) solutions. In these regimes, not all the internal energy is carried to the surface (where it can be radiated), part is trapped inside the disk and then carried toward the BH. As radiative process is inefficient, gas does not cool and the disk inflates reducing its particles density: AD is now an optically thin and geometrically thick structure.

As evident from the schematic representation in Figure 1.2, accretion disks typically do not exceed $10^{-3}-10^{-2}$ pc. Depending on BH type, the AD inner radius ranges $1.23-6$ $\mathrm{R_g}$, from maximally rotating Kerr BH to non-rotating Schwarschild BH. The gravitational radius

$$\mathrm{R_g} = \frac{\mathrm{GM}}{\mathrm{c}^2} = 1.5 \times 10^5 \, \frac{\mathrm{M_{BH}}}{\mathrm{M_\odot}} \tag{1.3}$$

is equal to $\sim$ few 10^{13} cm for $\mathrm{M_{BH}} = 10^8$ $\mathrm{M_\odot}$.

1.1.2 Mid-IR emission from the dusty torus

Optical/UV radiation emitted by AD partially leaves the AGN unaltered, but is partly absorbed by the dusty torus at scales of $0.1 - 10$ pc from the central SMBH. Dust grains heat up and re-emit absorbed energy at mid-infrared (mid-IR) wavelengths, producing the red dashed bump in Figure 1.1.

Thus, the torus is thought to provide AGN obscuration in Type 2 sources (i.e. obscured - see Section 1.2). Its inflated structure, due to internal radiation pressure overcoming vertical component of the BH gravity, is typically co-spatial with the accretion disk. Both smooth and clumpy models exist to describe the toroidal region. In the former case, obscuration is a matter of geometry, depending on

whether the line of sight (LoS) intercepts the structure. In the latter case, any inclination angle over the equatorial plane corresponds to a non-null probability for nuclear regions to be obscured. Therefore, clumpy model resolves puzzling observations of obscured broad-line AGN and unobscured narrow-line objects.

Some authors (e.g. Elitzur 2008, Elitzur et al. 2006) propose a dynamical origin for the torus: the hydromagnetic disk wind scenario. It would be constituted by outflowing clouds, and hence being a continuation of the inner Broad Line Region (BLR - see Section 1.2) rather than a separated component. In this prediction, the torus disappears at $L_{bol} < 10^{42}$ erg s^{-1} because the accretion rate can not sustain the required cloud outflow rate anymore.

In AGN mid-IR spectral component, a characteristic line at 9.7 μm can be seen as either an emission or absorption feature, the former in Type 1 sources (i.e. unobscured - see Section 1.2) and the latter in Type 2. It is due to the typical torus composition of silicate (together with graphite), which also determines its inner edge as the dust sublimation radius.

Most recent observations in the millimetre and infrared bands draw a much complex scenario, in which multiple components are possible (e.g. NGC 1068 - Garcia-Burillo et al. 2019; Circinus - Tristram et al. 2014) and the torus can be oriented in any way with respect to the disk and host galaxy. Thus, the donut-like structure is not an issue anymore.

1.1.3 X-ray emission from corona - accretion disk coupling

A hot ($\sim 10^{8-9}$ K) region called "corona" is located above (or around) the accretion disk. The simplest proposed model, called "lamp-post model", describes the corona as a point source located above the AD (see the yellow dot in Figure 1.2). Nonetheless, its geometry and heating mechanisms are still unknown. It is thought to give rise to the main X-ray component of AGN SED (light blue dotted curve in Figure 1.1), up-scattering AD radiation through Inverse Compton (IC) processes.

Part of AD thermal photons intercepts the corona, whose electrons are more "energetic" than photons. Thus, particles interact through IC processes: electrons lose energy, and radiation is scattered towards higher frequencies. Newly emitted photons become seeds for subsequent IC interactions, the overall Comptonisation phenomenon therefore results in the light blue dotted power-law profile presented in Figure 1.1.

Assuming the hot corona to emit isotropically, about half of its radiation is directed outward, while the other half returns to the accretion disk. Depending on the photons energy (E_{ph}), they interact differently with AD electrons:

$E_{ph} \leq 10$ keV Photoelectric absorption processes are dominant, resulting in the low-energy spectral cut-off;

10 keV $< E_{ph} <$ 40 keV This is the Thomson scattering regime. Coronal radiation is therefore deviated (partly upward) on its path, conserving its energy, thus the slope of the original power-law;

$E_{ph} \geq 40$ keV At these energies, scattering is based on Klein-Nishina cross section, rather than Thomson one, and is mainly directed forward. Thus, coronal emission penetrates deeper in the disk loosing energy, and photoelectric absorption is again important. It results in the high-energy spectral cut-off.

All of these phenomena produce the green dashed reflection profile in Figure 1.1.

During reflection processes of coronal photons by the AD, they may be absorbed by neutral or ionised iron atoms. If one of the innermost electrons is released, the atom is either ionised and excited. As a consequence, one of the electrons occupying the outer shells de-excites losing potential energy in the form of radiation. An emission line is therefore produced in the spectrum: the most prominent emerges when an electron in the L-shell de-excites to the K-shell. In this case, a 6.4 keV photon is released and the corresponding Fe Kα emission line arises from the continuum.

1.1.4 Radio emission from the jets

A small fraction ($< 10\,\%$) of active galaxies exhibits extended radio jets with various morphology. Ordered magnetic field is thought to be fundamental to jet launching (e.g. Blandford and Payne 1982, Blandford and Znajek 1977). Jets magnetic field "spine-sheet" layout projected on the plane of the sky emerges from polarisation studies. Longitudinal and transverse $\vec{B}$ vectors are visible along the edges and in jet's central regions, respectively. It is theorised to reflect a 3D helical structure. In combination with relativistic electrons, accelerated by efficient accretion on the central SMBH, it results in synchrotron emission from jets. Being a non-thermal process, it is parametrised through a power-law model:

$$S_\nu \propto \nu^{-\alpha} \tag{1.4}$$

where S_ν is flux density at frequency ν and α is spectral index.

FR II sources (see Section 1.2) also display *lobes* and *hot spots* shining at radio wavelengths. Their X-ray emission is supposed to be due to Inverse Compton scattering of CMB photons and/or Synchrotron Self Compton (SSC).

As evident in Figure 1.1 (brown solid and gray dotted curves), the emission from jetted sources extends widely beyond radio regime, covering the whole electromagnetic spectrum.

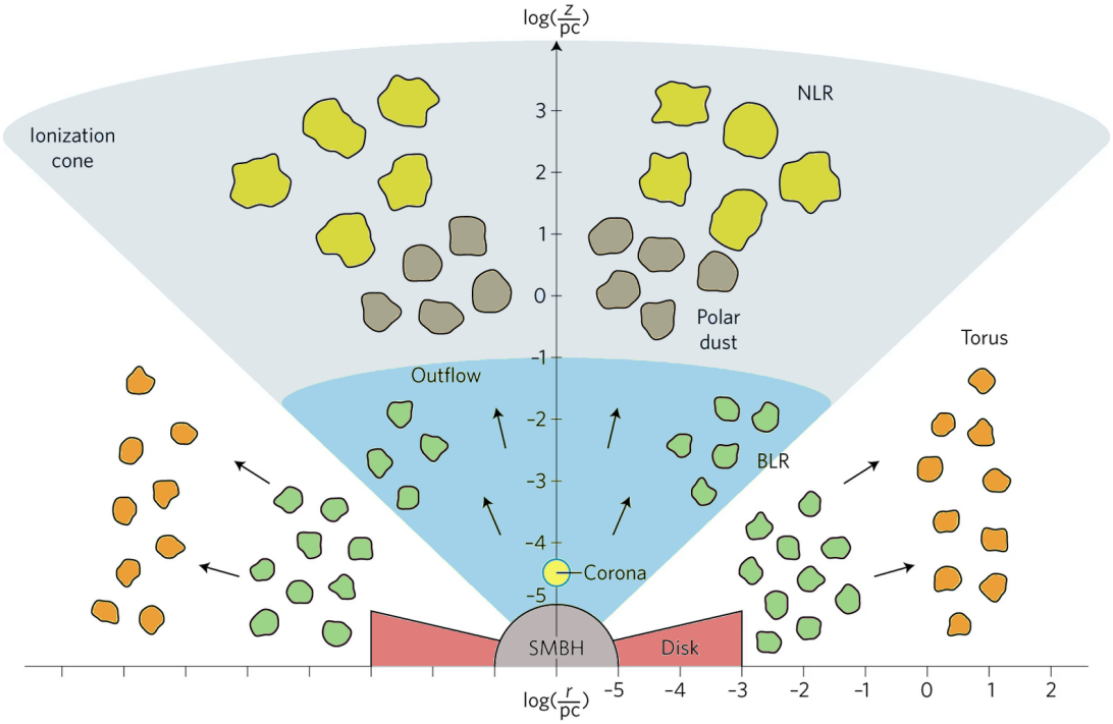

Figure 1.2: From Bianchi et al. 2022 - A schematic view of the inner parts of a non-jetted AGN indicating, from the centre to host-galaxy scales, the SMBH, the accretion disk and the corona, the BLR, the torus, and the NLR. Different colours indicate different compositions or densities.

1.2 AGN classification

AGN are typically classified based on

- Broad/narrow emission lines (e.g. Antonucci 1993, Urry and Padovani 1995, Netzer 2015);
- Radiative efficiency (e.g. Heckman et al. 2014);
- Relativistic jets (e.g. Padovani 2016)

resulting in numerous overlapping classes.

Optical spectra of Active Nuclei exhibit broad ($\gtrsim$ 1000s km s^{-1}) and/or narrow ($\approx$ 300 $-$ 1000 km s^{-1}) emission lines. Based on these evidences, Type 1 and Type 2 sources are defined as broad-line and narrow-line galaxies, respectively;

the same classification also apply to radio-loud objects. Both Seyfert galaxies and quasars can be classified as such, as their separation is not a physical one, but historically accepted to be determined by the absolute magnitude in the optical B band ($M_B \approx -23$): the former are lower luminosity versions of the latter. Eventual broadening of spectral lines is due to higher clouds velocity, thus stronger Doppler effect, when looking at gas closer to the central black hole. The source of broad emission lines is the Broad Line Region ($n_e \gtrsim 10^8$ cm^{-3}), thought to be located between the SMBH and the inner wall of the dusty torus (see Figure 1.2). In Type 2 objects, nuclear emission is reprocessed by lower density ($n_e \approx 10^3 - 10^5$ cm^{-3}) medium of the Narrow Line Region (NLR), which allows forbidden transitions to occur. NLR is thought to have sizes of hundreds of parsecs and be located above (and below) the plane of the dust (see Figure 1.2).

Radiative efficiency deals with AGN bolometric luminosity (L_{bol}) compared to the Eddington limit (L_{Edd}), that is to say the Eddington ratio:

$$\lambda_{Edd} = \frac{L_{bol}}{L_{Edd}} \qquad \text{where } L_{Edd} = 1.26 \times 10^{38} \frac{M_{BH}}{M_\odot} \text{ erg s}^{-1} \tag{1.5}$$

Eddington luminosity is the maximum isotropic luminosity a body can achieve when the outgoing radiation pressure, due to electron scattering, balances the gravitational force due to the central SMBH mass. Efficient sources are characterised by $\lambda_{Edd} > 0.01$ (e.g. Heckman et al. 2014) and, as described in Section 1.1.1, are typically associated with an optically thick and geometrically thin disk. Conversely, radiative inefficient accretion corresponds to $\lambda_{Edd} < 0.01$ and ADAF disk solutions.

A small fraction ($< 10\,\%$) of active galaxies exhibits extended radio jets with various morphology. They are divided by Fanaroff and Riley 1974 based on the ratio between the separation of the highest surface brightness regions on opposite sides of the central galaxy, and the extent of the source measured from the lowest surface brightness contour. It results in two categories: Fanaroff-Riley I (FR I) and FR II, also called edge-darkened and edge-brightened, respectively (see Figure 1.3). FR I are characterised by low-accretion efficiency, with jets which decelerate becoming sub-relativistic on scales of 100s pc to kpc. Thus, on these extent electrons are accelerated by shocks and emit synchrotron radiation. Moving outward, diffused lobes are found which fade with distance. FR II sources correspond to high-accretion efficiency allowing electrons to be accelerated up to the outermost edges of the jets, which are at least moderately relativistic and supersonic up to Mpc scales. The loci where plasma ejected by the AGN interacts with the surrounding medium are called "hot spots", which are the most luminous regions

in the jets, not present in FR I AGN. Moving backward from the hot spots to the central BH, fading lobes are present, composed by older and less energetic electrons.

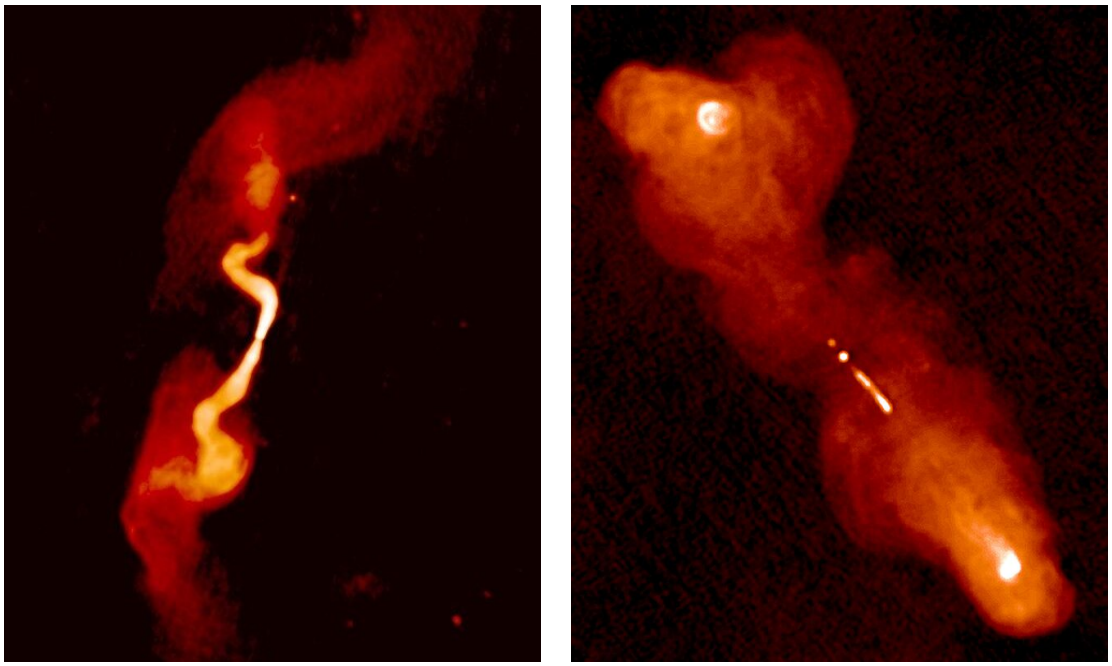

Figure 1.3: Radio images of galaxy 3C31 (NGC 383) *(left)* and Seyfert galaxy 3C219 *(right)* taken with the Very Large Array (VLA). They represent prototypes of FR I and FR II sources, respectively (Credits: NRAO/AUI/NSF).

Following the classification presented so far, Seyfert galaxies and QSOs represent radiatively efficient classes of non-jetted sources. Their jetted counterparts are radio QSOs and High-Excitation Radio Galaxies (HERGs), the latter being well represented by FR II objects. On the radiatively inefficient side, non-jetted AGN are all grouped as Low-Ionisation Nuclear Emission-line Region galaxies (LINERs), while Low-Excitation Radio Galaxies (LERGs) and BL Lacs represent jetted sources. The former class is well represented by FR I objects. A summary can be found in Table 1.1.

BL Lacs (inefficient accretion), along with Flat Spectrum Radio Quasars (FSRQs, efficient accretion), constitute the *blazar* category, which is characterised by extremely small inclination angles ($\lesssim 15 - 20\,^{\circ}$) of the jets with respect to the line of sight. BL Lacs present an almost featureless optical spectrum, while FSRQs display strong and broad emission lines like standard quasars. Flat ($\alpha < 0.5$) and Steep ($\alpha \geq 0.5$) Spectrum definitions (e.g. Wall 1975, Peacock et al. 1981, Willott et al. 2001, Kimball et al. 2008) are based on radio spectral index (α in Equation 1.4) and roughly correspond to compact and extended objects.

	Strong(er) jet	**Weak(er) jet**
Radiatively efficient ($\lambda_{\mathbf{Edd}} > \mathbf{0.01}$)	HERGs (mostly FR II)	non-jetted Seyferts and QSOs (both Type 1 and 2)
Radiatively inefficient ($\lambda_{\mathbf{Edd}} < \mathbf{0.01}$)	LERGs (mostly FR I) BL Lacs	LINERs

Table 1.1: Adapted from Padovani et al. 2017 - AGN classification summary, based on radiative efficiency and relativistic jet strength.

1.3 AGN Unified model

Multiple observations point towards classes presented in Section 1.2 to be ascribed to the line of sight:

1. Some Seyfert 2 galaxies' polarised spectra show the features observed in Type 1 AGN (e.g. Antonucci et al. 1985);

2. Different authors (e.g. Cohen 1983, Whittle 1985) highlight narrow-line properties of Seyfert 1 and 2 objects to be statistically indistinguishable.

In this context, Type 1 and 2 characteristics can be approximately reduced to a matter of inclination of the AGN system with respect to the line of sight, as shown in Figure 1.4. In unobscured sources, torus is seen face on, therefore it does not hide central engine and BLR; conversely, the solely NLR is visible in Type 2 objects due to dust intervening along the LoS. Thus, despite classifications presented in Section 1.2, all AGN are thought to be intrinsically the same object.

Osterbrock 1978 firstly proposed an optical unification to explain the nature of Seyfert 2 galaxies. During the same year, Blandford et al. 1978 suggested blazars to be standard QSOs seen along jets' axis: the same integral view applies also jetted sources!

Search for a unified model is encouraged by the *"belief that any description of nature must be made as simple as possible in the absence of evidence to the contrary"* (Peterson 1997). Nonetheless, numerous issues still need to be properly understood. A couple of examples:

1. Seyfert 2 galaxies typically do not display polarised continua despite being expected as a consequence of photons' interaction with NLR. However, this evidence does not rule out the presence of BLR or occurrence of multiple depolarising scattering;

2. Assuming jets to be randomly oriented with respect to the LoS, many are expected to have radio axis close to the plane of the sky. In this case, jet and counter-jet should exhibit similar surface brightness, in contradiction to observations. Due to Doppler de-beaming of the counter-jet, oriented opposite to the observer, only one jet is typically visible.

Moreover, further important factors should be taken into consideration (e.g. galaxy morphology, gas/dust content).

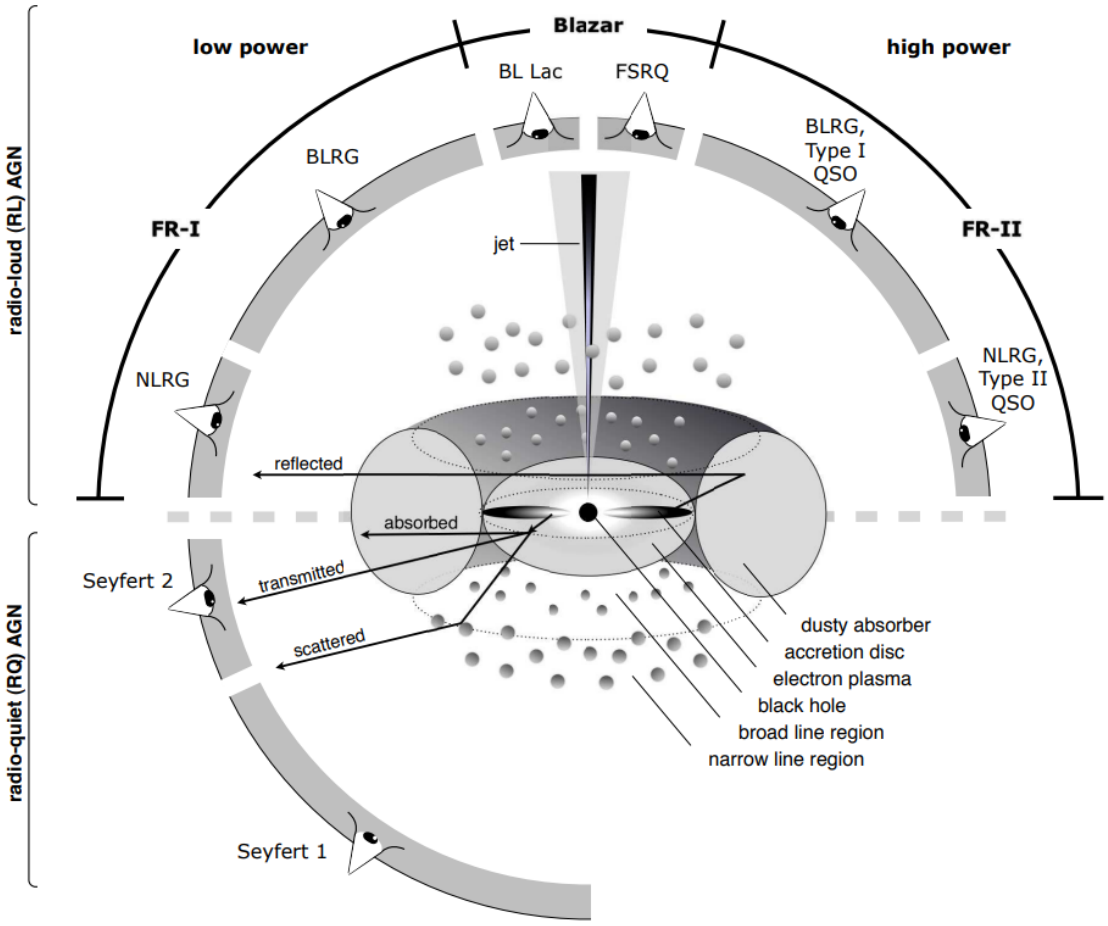

Figure 1.4: From Beckmann et al. 2012 - Schematic representation of current understanding of the AGN phenomenon in the unified scheme. The type of object depends on the viewing angle, whether or not the AGN produces a significant jet emission, and how powerful the central engine is. Note that radio loud objects are generally thought to launch symmetric jet emission, but FR II galaxies often display just one, due to relativistic de-beaming of the counter-jet.

1.4 Active Galactic Nuclei feedback

Cosmological need of AGN feedback is claimed to reduce baryon - to - stars conversion efficiency in massive galactic haloes. In Figure 1.5 three different simulations (grey, violet and black lines: without any feedback contribution, including star formation (SF) feedback and taking into consideration both SF and AGN feedback, respectively - Somerville et al. 2008) are compared to a semi-empirical model (green solid curve - Moster et al. 2012) in the $\mathrm{Log}(\mathrm{M_{halo}}) - \frac{\mathrm{M_{stellar}}}{\mathrm{M_{halo}}}$ plane. It is evident that at low halo masses the impact of star formation is sufficient to reproduce observed properties (violet simulation), but for $\mathrm{M_{halo}} \gtrsim 10^{12}\ \mathrm{M_{\odot}}$ AGN feedback is also required (black simulation).

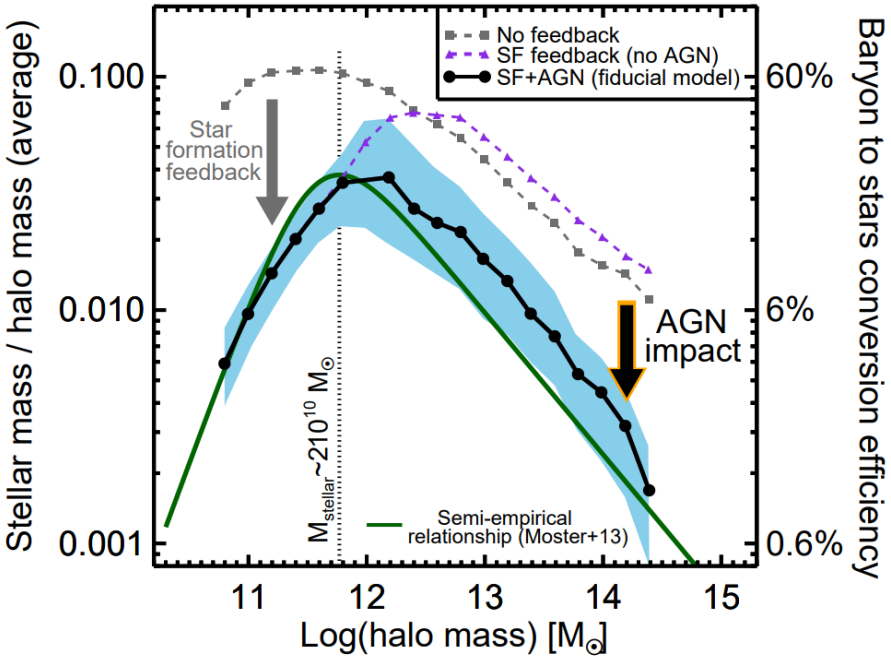

Figure 1.5: From Harrison 2017 - The ratio of stellar mass to halo mass as a function of halo mass for three different runs of a simulation (Somerville et al. 2008) and for the semi-empirical relationship (Moster et al. 2012). The shaded region shows the 16th and 84th percentiles of the fiducial model that includes energy injection from AGN and star formation. The right y-axis shows the efficiency for turning baryons into stars ($\mathrm{M_{stellar}}/\mathrm{f_b}\,\mathrm{M_{halo}}$, where the factor of $\mathrm{f_b} = 0.17$ is the cosmological baryon fraction). The impact of including star formation feedback in the model is to reduce the efficiency of converting baryons into stars in low-mass haloes. For massive haloes, energy injection from AGN is required in order to reduce these efficiencies. Such effects are required in most models in order to reproduce many observable properties of the massive galaxy population.

Active nuclei affect star formation injecting energy ($\mathrm{E_{BH}}$) into the host galaxy, thus heating gas or expelling it, opposite to SF process conditions. It can be easily

seen that the AGN could have huge impact on its host galaxy:

$$\frac{E_{BH}}{E_{host}} \approx \frac{\eta\, M_{BH}\, c^2}{M_{host}\, \sigma^2} = 2 \times 10^{-4} \left(\frac{c}{\sigma}\right)^2 \tag{1.6}$$

where E_{host} and M_{host} are host galaxy binding energy and mass, respectively; $\eta \approx 0.1$ is accretion radiative efficiency; σ is stars velocity dispersion of galactic bulge; c is the speed of light. As $\sigma \approx 200 - 300$ km s^{-1} and c $\approx 3 \times 10^5$ km s^{-1}, $E_{BH}/E_{host} \gg 1$ and the injected energy would be enough to destroy host galaxy. Feedback process is therefore expected to be inefficient, so that galaxies are preserved.

Cooling prevention and gas expulsion correspond to two feedback modes presented in literature: the kinetic and radiative scenario, respectively.

Kinetic (jet) mode is associated with low Eddington ratios ($\lambda_{Edd} < 0.01$). Parsec-scale jets are produced and plasma interacts with the surrounding interstellar medium (ISM) through mechanical action (*left panel* in Figure 1.6[1]). In clusters of galaxies, radio jets can remove the X-ray emitting gas creating "cavities". They clearly emerge in Figure 1.7, where X-ray emission (blue) makes space to the jet radio one (red);

Radiative (quasar) mode is typical of efficient-accretion sources ($\lambda_{Edd} > 0.01$). Radiation pressure drives the interaction of accretion disk winds with ISM (*right panel* in Figure 1.6.)

The AGN outflows sustained by radiation pressure sweep ISM of the host galaxy while expanding, and a shock is produced at the interface between wind and streamed material. Depending on whether the shocked gas rapidly cools or not, two regimes can be defined:

- Momentum-driven;
- Energy-driven,

respectively. Moreover, an inner reverse shock is generated as a consequence of the wind-ISM interaction, which slows the outflow itself.

Following many literature works (e.g. King 2003, King 2005, King 2010, Fabian et al. 2012, Faucher-Giguère and Quataert 2012, Costa et al. 2014, King and Pounds 2015, Chartas et al. 2020), the two regimes are presented in the following Sections.

[1] `https://tinyurl.com/agn-feedback`

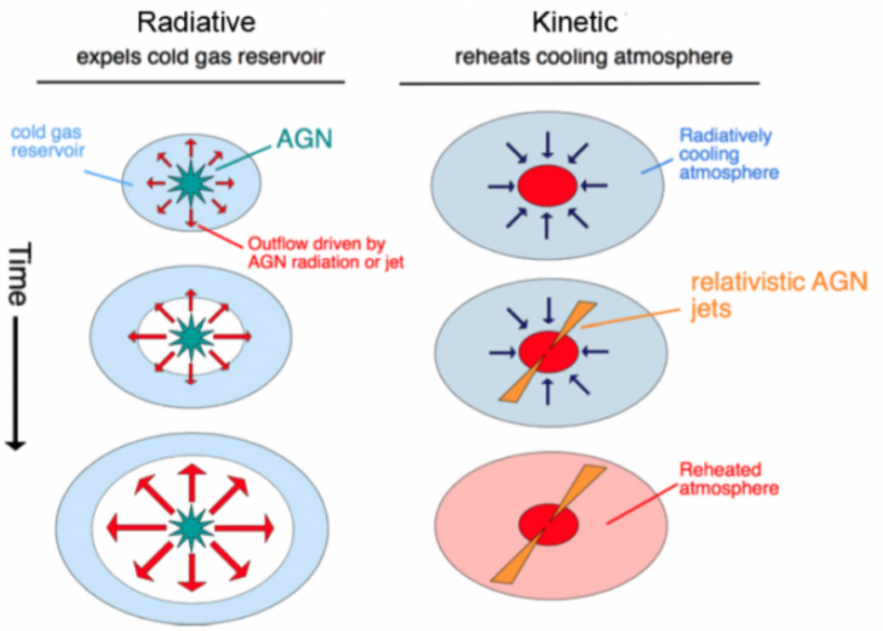

Figure 1.6: Schematic representation of radiative *(left)* and kinetic *(right)* feedback modes.

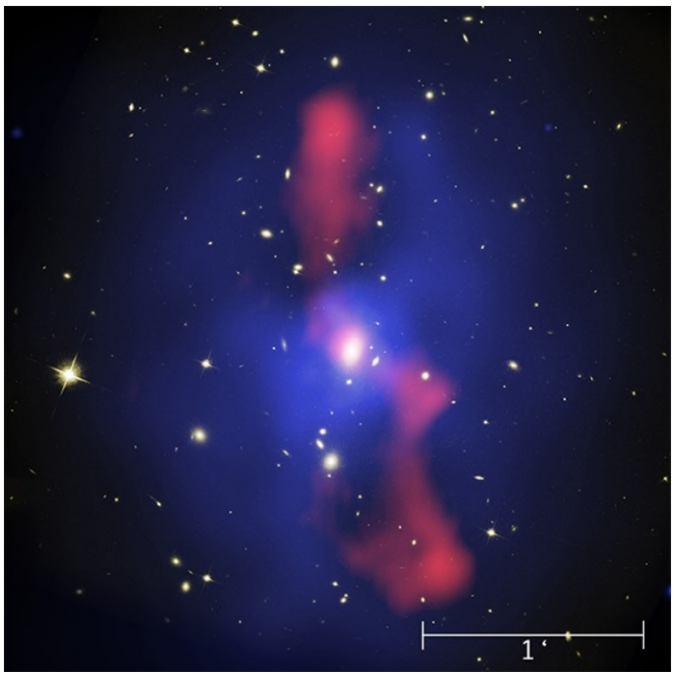

Figure 1.7: From McNamara et al. 2009 - Image of the inner 200 arcsec (700 kpc) of the MS0735.6+7421 cluster combining the X-ray (blue), I-band (white), and radio wavelengths (red).

1.4.1 Momentum-driven winds

In the momentum-driven scenario, only momentum is conserved from the wind to the swept-up interstellar medium: only ram pressure is transmitted, while energy

is radiated. Thus, shock region is very narrow (as evident from Figure 1.8), as gas quickly looses heat and is compressed: it actually becomes isothermal. Emitting processes involved in gas cooling are the IC with SMBH radiation field (e.g. Ciotti and Ostriker 1997) and the free-free one. Inverse Compton interaction is efficient as immediate postshock temperature is $\sim 10^{10} - 10^{11}$ K, compared to $\sim 10^7$ K of nuclear radiation. Once the IC cooling has compressed ISM, the free-free process becomes dominant as it goes as the square of the density.

Conserved ram pressure (or outflow momentum rate) can be defined as

$$\dot{p}_{out} = \dot{M}_{out} v_{out} \approx \frac{L_{Edd}}{c} \tag{1.7}$$

where $\dot{M}_{out}$ and v_{out} are the mass outflow rate and postshock wind velocity, respectively. Outflow mechanical luminosity is therefore

$$L_{out} = \frac{1}{2} \dot{M}_{out} v_{out}^2 = \frac{L_{Edd}}{c} \frac{v_{out}}{2} \approx 0.05\, L_{Edd} \tag{1.8}$$

assuming $v_{out} \approx 0.1c$, which is typical of X-ray emitting nuclear Ultra Fast Outflows (UFOs), traced by highly ionised and blueshifted Fe K-shell absorption lines of ionised gas. These are mildly relativistic ($v_{UFO} \gtrsim 0.1c$) disk winds, transporting $0.01 - 1\ M_\odot\, yr^{-1}$ (e.g. Tombesi et al. 2010, Tombesi et al. 2012).

Starting from equation of motion of the swept-up shell

$$\frac{d}{dt}[M_g(R)\dot{R}] + \frac{G M_g(R)[M_{BH} + M(R)]}{R^2} = \frac{L_{Edd}}{c} \tag{1.9}$$

where $M_g(R)$ and $M(R)$ are swept-up gas and total mass when shell radius is R, respectively; G is the universal gravitational constant. At sufficiently large distance from the nucleus, M(R) is the dominant term: swept-up mass is larger than the wind one. Then, Equation 1.9 becomes

$$\frac{d}{dt}[M_g(R)\dot{R}] = \frac{L_{Edd}}{c} \tag{1.10}$$

Moreover, imposing shocked gas to be able to escape to infinity, the analytic solution is

$$R^2 = \frac{G L_{Edd}}{2 f_g \sigma^2 c} t^2 \tag{1.11}$$

where $f_g \approx 0.16$ (e.g. Spergel et al. 2003) is the gas fraction and σ is the gas

velocity dispersion. Then,

$$v_{out} \approx \frac{R}{t} = \sqrt{\frac{GL_{Edd}}{2f_g \sigma^2 c}} \tag{1.12}$$

which holds for momentum-driven regimes only. Re-calling Equation 1.8, it can be re-written as

$$L_{out} = \frac{1}{2}\dot{M}_{out} v_{out}^2 \propto \frac{\sigma}{c} L_{Edd} \tag{1.13}$$

In Equation 1.13 the σ/c term emerges, which is the outflow mechanical luminosity fraction actually injected into ISM:

$$E_{mom} \approx \frac{\sigma}{c} L_{out} \approx 0.1\, E_{gas} \tag{1.14}$$

As anticipated, momentum-driven AGN feedback is an inefficient process and only $\sim 10\,\%$ of the bulge gas binding energy is injected by the outflow, not compromising galaxy stability. As there is no danger that the black hole drives away the gas suppressing accretion, this regime is a stable environment for BH mass growth.

Moreover, King 2003 demonstrate that momentum-driven winds affecting galactic bulge are able to reproduce the observed $M_{BH} - \sigma$ relation. It is parametrised as follows:

$$M_{BH} \approx 3 \times 10^8\, M_\odot\, \sigma_{200}^{\alpha} \tag{1.15}$$

where σ (σ_{200}) is stellar velocity dispersion (in units of 200 $km\,s^{-1}$) in the galactic bulge and $\alpha \approx 4.4$ (e.g. Ferrarese et al. 2000, Gebhardt et al. 2000).

Following King 2003, it is shown below that momentum-driven regime is sustained out to just few kiloparsecs. This is just as one would expet, given that such flow allows stable black hole mass growth. He assumes the SMBH radiation density to be

$$U_{rad} = \frac{L_{Edd}}{4\pi R^2 c b} \tag{1.16}$$

where the Eddington luminosity is classically defined as $L_{Edd} = 4\pi G M_{BH} c/\kappa$ (κ is the electron scattering opacity), R is the distance from the black hole and b represents wind coverage. Then, Compton cooling time for shocked gas' electrons interacting with nuclear photons is

$$\begin{aligned} t_C &= \frac{3 m_e c}{8\pi\sigma_T U_{rad}} \frac{m_e c^2}{E} = \frac{2}{3}\frac{cR^2}{GM_{BH}}\left(\frac{m_e}{m_p}\right)^2\left(\frac{c}{v_{out}}\right)^2 b = \\ &\approx 10^5 \times R_{kpc}^2 \left(\frac{c}{v_{out}}\right)^2 b\, M_8^{-1}\ yr \end{aligned} \tag{1.17}$$

where m_e and m_p are electron and proton masses, respectively; σ_T is the Thomson cross section for electron scattering; $E \approx 3/16\, m_p v_{out}^2$ is the electron energy in postshock gas. R_{kpc} and M_8 are R and M_{BH} in units of kpc and $10^8\, M_\odot$, respectively. Heating losses are efficient as long as t_C is shorter than the wind flow time $t_{flow} = R/v_s$, where v_s is velocity of the expanding shock. Once the shock size reaches radius R_C, corresponding to $t_C = t_{flow}$, gas is no longer efficiently cooled, residual thermal pressure accelerates swept-up ISM and shock region expands. The outflow enters the energy-driven regime.

1.4.2 Energy-driven winds

Opposite to rapid cooling, characterising momentum-driven outflows, energy-driven ones are almost adiabatic. Energy is conserved from the AGN wind to swept-up gas and cooling is therefore prevented. It results in an expanding shock region which becomes much thicker than in momentum-driven scenario (see comparison in Figure 1.8). Thus, adiabatic winds are more violent, indeed energy injected in the ISM (E_{mom}) is larger than galactic bulge gas binding energy (E_{gas}):

$$E_{mom} \approx L_{out} \approx 100\, E_{gas} \tag{1.18}$$

As a result, the central engine could clean galactic bulge from gas, quenching accretion.

Theory and observations differ (galaxies are actually seen) on how wind's energy is transmitted to the ISM. Contrarily to momentum-driven winds, in energy-conserving ones, the quantity E_{mom} is injected in the form of heating, rather than kinetic energy of the surrounding medium. Thus, this outflows could alter the conditions needed to star formation, quenching the process, but not disrupt the galaxy.

1.4.3 Observational evidences of feedback

Studying sources where both small-scale high-velocity winds and large-scale lower-velocity ones are observable may shed light on the two aforementioned scenarios. Different relations between outflow velocity and momentum boost ($\dot{p}_{out}/\frac{L_{bol}}{c}$) are indeed expected. Being observed in the innermost regions, UFOs may be momentum-conserving flows, not clearing galactic bulge from accreating gas. On the other hand, galaxy-scale molecular winds are predicted to be energy-driven, as cooling processes are no more efficient at those radii. Figure 1.9 illustrates several examples of how data locates with respect to the predicted trends. Filled

and empty symbols represent molecular outflows and UFOs, respectively; the two regimes are also highlighted by the indigo rectangles. Black dashed line corresponds to the $v_{out} - \dot{p}_{out}/\frac{L_{bol}}{c}$ relation for an energy conserving wind, while the red dotted line for a momentum-driven one. It emerges that the relation between UFO and galaxy-scale molecular outflow is very complex and may significantly differ from typical expectations of the models of energy-conserving expansion.

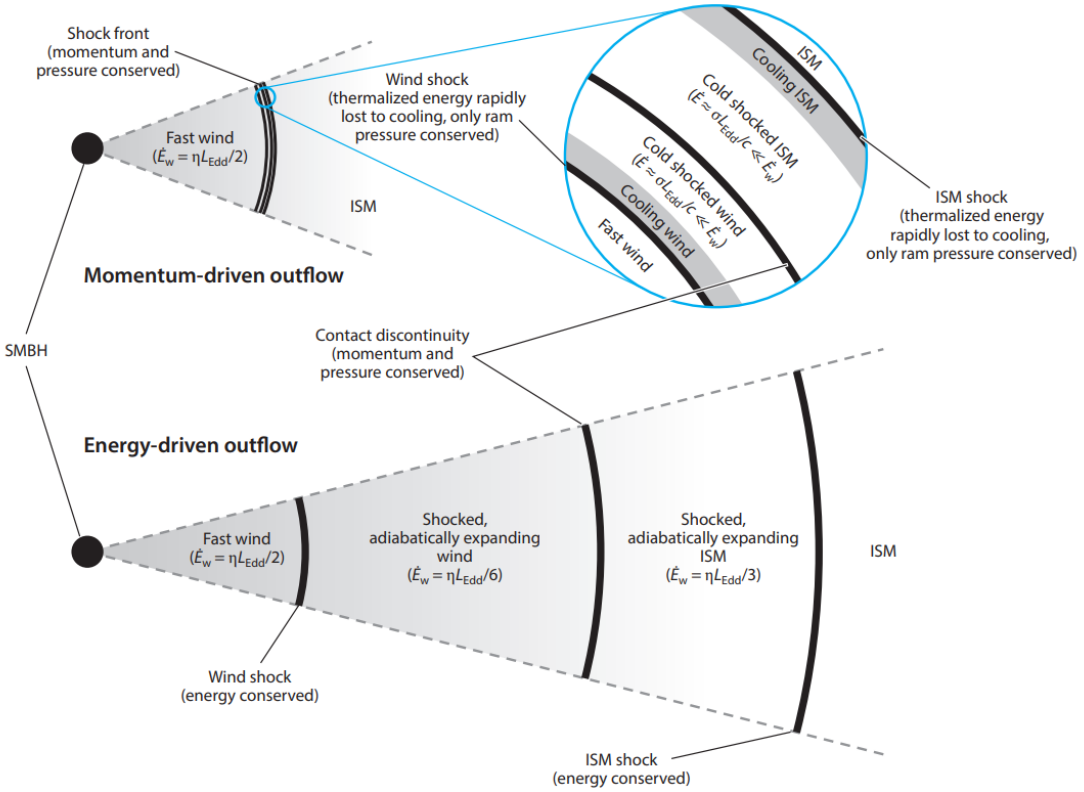

Figure 1.8: From King and Pounds 2015 - Schematic picture of *(top)* momentum-driven and *(bottom)* energy-driven outflows. In both cases, a fast wind (~ 0.1c) impacts the interstellar gas of the host galaxy, producing an inner reverse shock that slows the wind and an outer forward shock that accelerates the swept-up gas. In the momentum-driven case, the shocks are very narrow and rapidly cool to become effectively isothermal; only the ram pressure is communicated to the outflow, leading to very low kinetic energy $\sim (\sigma/c)\, L_{Edd}$. In an energy-driven outflow, the shocked regions are much wider and do not cool; they expand adiabatically, communicating most of the kinetic energy of the wind to the outflow (in simple cases divided in a ratio of approximately 1:2 between the shocked wind and the swept-up gas). The outflow radial momentum flux is therefore larger than that of the wind. Momentum-driven conditions hold for shocks confined to within ~ 1 kpc of the AGN and likely establish the $M-\sigma$ relation (e.g. King 2003, King 2005). Once the supermassive black hole mass attains the critical $M-\sigma$ value, the shocks move further from the AGN, and the outflow becomes energy driven. This produces the observed large-scale molecular outflows that probably sweep the galaxy clear of gas.

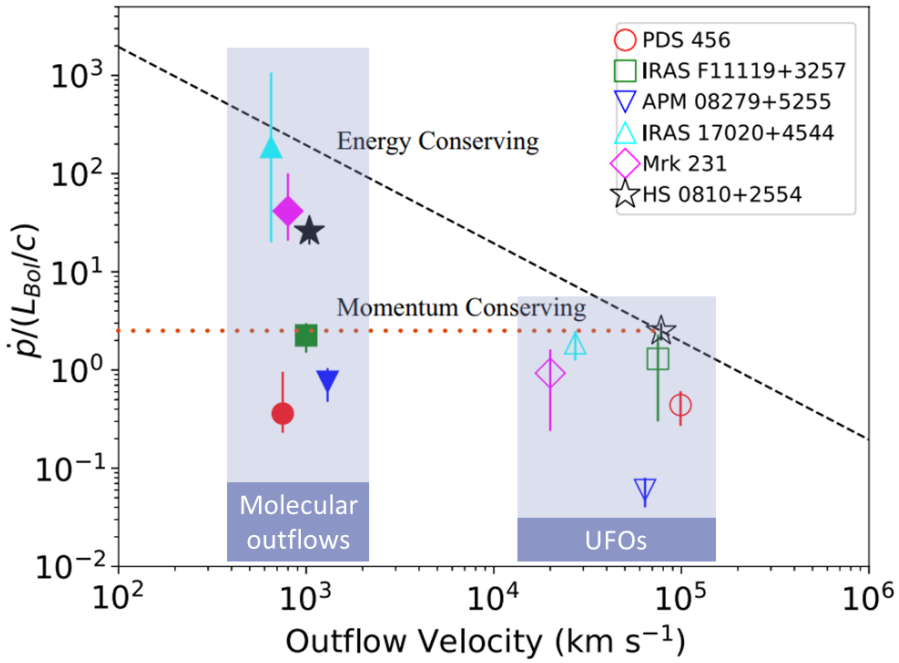

Figure 1.9: From Chartas et al. 2020 - The momentum boost $\dot{p}/\frac{L_{bol}}{c}$ as a function of outflow velocity. The filled and unfilled symbols correspond to the molecular and ultrafast outflows, respectively. The dashed and dotted lines represent the dependence of the momentum boost with outflow velocity for energy-conserving and momentum conserving outflows, respectively, for HS 0810+2554. The data for AGN other than HS 0810+2554 have been obtained from the literature (e.g. Bischetti et al. 2019, Tombesi et al. 2015, Veilleux et al. 2017, Feruglio et al. 2015, Feruglio et al. 2017). For consistency, published results have been adjusted assuming the same conversion factor of $\alpha_{CO} = 0.8\,M_{\odot}\ (K\,km\,s^{-1}\,pc^{2})^{-1}$ for estimating the total molecular gas mass.

2

The WISSH project

Cross-correlating the WISE all-sky source catalogue (Wright et al. 2010) and the SDSS DR7 catalogue (Schneider et al. 2010), Weedman et al. 2012 compiled a sample containing 100 Type 1 AGN with a flux density $S_{22\mu m} > 3$ mJy at $z > 1.5$. The WISSH sample has been obtained removing lensed sources and those with a contaminated photometry. WISSH stays for WISE/SDSS-selected Hyper-luminous quasars, and is composed of 85 radio-quiet objects with bolometric luminosity $L_{Bol} \approx 2 \times 10^{47} - 10^{48}$ erg s^{-1} at $z \approx 1.7 - 4.7$. WISE and SDSS are an infrared all-sky survey and optical survey covering $\sim 1/4^{th}$ of the sky, respectively. In Table 2.1, WISSH quasars are listed along with their identification number, coordinates and redshifts.

Based on archival and proprietary data, all of the WISSH sources have now a multi-wavelength coverage from radio to X-rays, thus allowing the AGN phenomenon to be studied in all of its manifestations. Since 2017, optical/UV spectral features (Bischetti et al. 2017, Vietri et al. 2018, Zappacosta et al. 2020, Vietri et al. 2022), star formation rate (SFR) (Duras et al. 2017), accretion disk-corona system (Martocchia et al. 2017 - M17 hereafter), overdensities in the region of the quasars (Bischetti et al. 2018), BAL fraction (Bruni et al. 2019), AGN Circum-Galactic Medium (CGM - Travascio et al. 2020), molecular gas content in the host galaxies (Bischetti et al. 2021), and the mean SED (Saccheo et al. 2023) of these extreme sources have been studied. WISSH papers published so far are summarised in Table 2.2.

In the following, the main known properties of the WISSH sample are presented. They will be linked with newly reported X-ray results, in order to build a more comprehensive understanding of the AGN system and the physical processes that it involves.

ID	RA	DEC	z
WISSH01	00 45 27.68	+14 38 16.1	1.9897[d]
WISSH02	01 24 03.77	+00 44 32.6	3.822[d]
WISSH03	01 25 30.85	−10 27 39.8	3.3588[d]
WISSH04	02 09 50.71	−00 05 06.4	2.870[c]
WISSH05	02 16 46.94	−09 21 07.2	3.7387[d]
WISSH06	04 14 20.90	+06 09 14.2	2.6324[e]
WISSH07	07 35 02.30	+26 59 11.5	1.999[d]
WISSH08	07 45 21.78	+47 34 36.1	3.225[a]
WISSH09	07 47 11.14	+27 39 03.3	4.126[e]
WISSH10	08 01 17.79	+52 10 34.5	3.257[b]
WISSH11	08 18 55.77	+09 58 48.0	3.6943[f]
WISSH12	08 46 31.52	+24 11 08.3	4.7218[d]
WISSH13	09 00 33.50	+42 15 47.0	3.294[a]
WISSH14	09 04 23.37	+13 09 20.7	2.9765[d]
WISSH15	09 28 19.29	+53 40 24.1	4.466[d]
WISSH16	09 41 40.17	+32 57 03.2	3.454[d]
WISSH17	09 47 34.19	+14 21 16.9	3.031[e]
WISSH18	09 50 31.63	+43 29 08.4	1.7696[d]
WISSH19	09 58 41.21	+28 27 29.5	3.434[b]
WISSH20	09 59 37.11	+13 12 15.4	4.0781[d]
WISSH21	10 13 36.37	+56 15 36.3	3.6507[d]
WISSH22	10 14 47.18	+43 00 30.1	3.1224[d]
WISSH23	10 15 49.00	+00 20 20.0	4.407[c]
WISSH24	10 20 40.61	+09 22 54.2	3.6584[d]
WISSH25	10 25 41.78	+24 54 24.2	2.3917[d]
WISSH26	10 26 32.97	+03 29 50.6	3.8808[d]
WISSH27	10 27 14.77	+35 43 17.4	3.1182[d]
WISSH28	10 48 46.63	+44 07 10.8	4.408[d]
WISSH29	10 51 22.46	+31 07 49.3	4.2742[d]
WISSH30	10 57 56.25	+45 55 53.0	4.1306[d]
WISSH31	11 03 52.74	+10 04 03.1	3.6004[d]
WISSH32	11 06 07.47	−17 31 13.5	2.572[e]
WISSH33	11 06 10.72	+64 00 09.6	2.221[b]
WISSH34	11 10 17.13	+19 30 12.5	2.502[e]
WISSH35	11 10 38.63	+48 31 15.6	2.9741[d]
WISSH36	11 10 55.21	+43 05 10.0	3.8492[d]
WISSH37	11 11 19.10	+13 36 03.9	3.490[b]
WISSH38	11 22 58.77	+16 45 40.3	3.0398[f]
WISSH39	11 30 17.37	+07 32 12.9	2.659[d]
WISSH40	11 57 47.99	+27 24 59.6	2.217[b]
WISSH41	11 59 06.52	+13 37 37.7	4.0084[d]
WISSH42	12 00 06.25	+31 26 30.8	2.9947[d]
WISSH43	12 01 44.36	+01 16 11.6	3.248[b]
WISSH44	12 01 47.90	+12 06 30.2	3.512[a]
WISSH45	12 04 47.15	+33 09 38.7	3.638[d]
WISSH46	12 10 27.62	+17 41 08.9	3.831[g]
WISSH47	12 15 49.81	−00 34 32.1	2.6987[d]
WISSH48	12 19 30.77	+49 40 52.2	2.6928[d]
WISSH49	12 20 16.87	+11 26 28.1	1.8962[d]
WISSH50	12 36 41.45	+65 54 42.1	3.424[b]
WISSH51	12 37 14.60	+06 47 59.5	2.7891[d]
WISSH52	12 45 51.44	+01 05 05.0	2.8068[d]
WISSH53	12 49 57.23	−01 59 28.8	3.6286[d]
WISSH54	12 50 05.72	+26 31 07.5	2.0476[e]
WISSH55	12 50 50.88	+20 46 58.7	3.543[e]
WISSH56	13 05 02.28	+05 21 51.1	4.101[d]
WISSH57	13 10 11.60	+46 01 24.4	2.1423[d]
WISSH58	13 26 54.96	−00 05 30.1	3.303[a]
WISSH59	13 28 27.06	+58 18 36.8	3.140[d]
WISSH60	13 33 35.78	+16 49 03.9	2.099[h]
WISSH61	14 21 23.97	+46 33 18.0	3.454[b]
WISSH62	14 22 43.02	+44 17 21.2	3.648[b]
WISSH63	14 26 56.18	+60 25 50.8	3.1972[d]
WISSH64	14 33 52.21	+02 27 13.9	4.728[c]
WISSH65	14 41 05.53	+04 54 54.9	2.080[h]
WISSH66	14 47 09.24	+10 38 24.5	3.7042[d]
WISSH67	14 51 25.31	+14 41 36.0	3.094[e]
WISSH68	15 06 54.55	+52 20 04.7	4.0995[d]
WISSH69	15 13 52.52	+08 55 55.7	2.8883[d]
WISSH70	15 21 56.48	+52 02 38.5	2.218[b]
WISSH71	15 38 30.55	+08 55 17.0	3.567[b]
WISSH72	15 44 46.34	+41 20 35.7	3.5513[d]
WISSH73	15 49 38.72	+12 45 09.1	2.365[a]
WISSH74	15 54 34.17	+11 09 50.6	2.930[e]
WISSH75	15 55 14.85	+10 03 51.3	3.529[c]
WISSH76	15 59 12.34	+48 28 19.9	3.419[d]
WISSH77	15 59 52.67	+19 23 10.4	3.9532[f]
WISSH78	16 21 16.92	−00 42 50.8	3.7285[d]
WISSH79	16 33 00.13	+36 29 04.8	3.5747[d]
WISSH80	16 39 09.10	+28 24 47.1	3.846[c]
WISSH81	16 50 53.78	+25 07 55.4	3.337[e]
WISSH82	17 01 00.60	+64 12 09.3	2.753[c]
WISSH83	21 23 29.46	−00 50 52.9	2.282[b]
WISSH84	22 38 08.07	−08 08 42.1	3.1422[d]
WISSH85	23 46 25.66	−00 16 00.4	3.511[b]

Table 2.1: The WISSH sample: ID, coordinates and redshifts. Redshifts are provided by [a]Bischetti et al. 2017, [b]Vietri et al. 2018, [c]Bischetti et al. 2021, [d]Hewett et al. 2010, [e]Pâris et al. 2014, [f]primary z by Lyke et al. 2020, [g]Yi et al. 2020, [h]Vietri et al. 2020.

2.1 NLR and BLR winds

By construction, all 85 quasars have photometric observations in the SDSS *ugriz* filters and in the four WISE bands at 3.3 μm, 4.6 μm, 12 μm and 22 μm. For $\sim 80\,\%$ of the sample, 2MASS photometry in the J, H and K bands has been collected, while the remaining sources have been targeted with TNG-NICS. Spectroscopic data from LBT/LUCI and VLT/SINFONI are also available for 18 quasars.

Through spectroscopic analysis of [OIII] and CIV emission lines, Bischetti et al. 2017 and Vietri et al. 2018 studied BLR and NLR winds occurring in WISSH QSOs.

I.	Powerful ionised outflows in hyper-luminous quasars	Bischetti et al. 2017
II.	Giant star nurseries in hyper-luminous quasars	Duras et al. 2017
III.	X-ray properties of hyper-luminous quasars	Martocchia et al. 2017
IV.	Broad line region versus kiloparsec-scale winds	Vietri et al. 2018
V.	ALMA reveals the assembly of a giant galaxy around a z = 4.4 hyper-luminous QSO	Bischetti et al. 2018
VI.	Fraction and properties of BAL quasars in the hyper-luminosity regime	Bruni et al. 2019
VII.	The impact of extreme radiative field in the accretion disk and X-ray corona interplay	Zappacosta et al. 2020
VIII.	Outflows and metals in the circum-galactic medium around the hyper-luminous $z \sim 3.6$ quasar J1538+08	Travascio et al. 2020
IX.	Cold gas content and environment of luminous QSOs at $z \sim 2.4 - 4.7$	Bischetti et al. 2021
X.	Discovery of a multi-component and highly variable UV ultra-fast outflow in a z = 3.6 quasar	Vietri et al. 2022
XI.	The mean spectral energy distribution and bolometric corrections of the most luminous quasars	Saccheo et al. 2023

Table 2.2: WISSH papers

Two different sub-populations are identified in the WISSH sample: *[OIII]* quasars and *Weak [OIII]* quasars. The *[OIII]* sample exhibits prominent [OIII] emission lines with [OIII] and CIV Rest-frame Equivalent Width $\mathrm{REW_{[OIII]}} > 5$ Å and $\mathrm{REW_{CIV}} \approx 20 - 40$ Å, respectively, and modest CIV velocity shifts with respect to the systemic redshift ($\mathrm{v_{CIV}^{peak}} \leq 2000\ \mathrm{km\,s^{-1}}$). Conversely, the *Weak [OIII]* sample is characterised by weak or absent [OIII] emission lines with $\mathrm{REW_{[OIII]}} < 5$ Å, $\mathrm{REW_{CIV}} < 20$ Å and an extremely large blueshifted CIV emission ($\mathrm{v_{CIV}^{peak}} \approx 2500 - 7500\ \mathrm{km\,s^{-1}}$). Two explanations are proposed for the observed spectral properties in terms of orientation and ionisation cone. Following Risaliti et al. 2011 and Bisogni et al. 2016, higher $\mathrm{REW_{[OIII]}}$ reflects a system closer to be edge-on with respect to the line of sight. Considering a polar direction for the CIV wind, the two sub-populations would correspond to the dichotomy between NLR (*[OIII]* sample) and BLR (*Weak [OIII]* sample) winds.

From [OIII] and CIV luminosities, the mass outflow rate is derived, resulting in $\dot{\mathrm{M}}_{\mathrm{[OIII]}} \approx (1.7 - 7) \times 10^3\ \mathrm{M_\odot\,yr^{-1}}$ and $\dot{\mathrm{M}}_{\mathrm{CIV}} \approx 10 - 100\ \mathrm{M_\odot\,yr^{-1}}$ for NLR and

BLR winds, respectively. Then, the kinetic power ($\dot{E}_{kin}$) associated with them is obtained. Comparing $\dot{E}_{kin}$ to bolometric luminosities, Bischetti et al. 2017 and Vietri et al. 2018 estimate $\dot{E}_{kin}/L_{bol} \approx 1-3\,\%$ for [OIII] outflows and $\sim 20\,\%$ of CIV winds, which is very close to the predicted value $\dot{E}_{kin}/L_{bol} \approx 0.5-5\,\%$ (e.g. Matteo et al. 2005) needed to account for the $M_{BH}-\sigma$ relation. The remaining $\sim 80\,\%$ has kinetic powers similar to those traced by the [OIII] emission lines in less luminous objects; see Figure 2.1 from Vietri et al. 2018.

v_{max} and $\dot{M}$ are studied as a function of bolometric luminosity and compared with lower-luminous samples. Bischetti et al. 2017 suggest a correlation between v_{max} and L_{Bol} consistent with the relation expected for an energy conserving wind ($L_{bol} \propto v_{max}^5$ - Costa et al. 2014) - Figure 2.2a from Bischetti et al. 2017. The increase of $\dot{M}$ as a function of L_{bol} (Figure 2.2b from Bischetti et al. 2017) is consistent with the theoretical idea that a larger amount of gas is invested by radiatively-driven winds in more luminous quasars, and may suggest that at such luminosities, the ionised component traces a larger fraction of the outflowing gas (e.g Fiore et al. 2017).

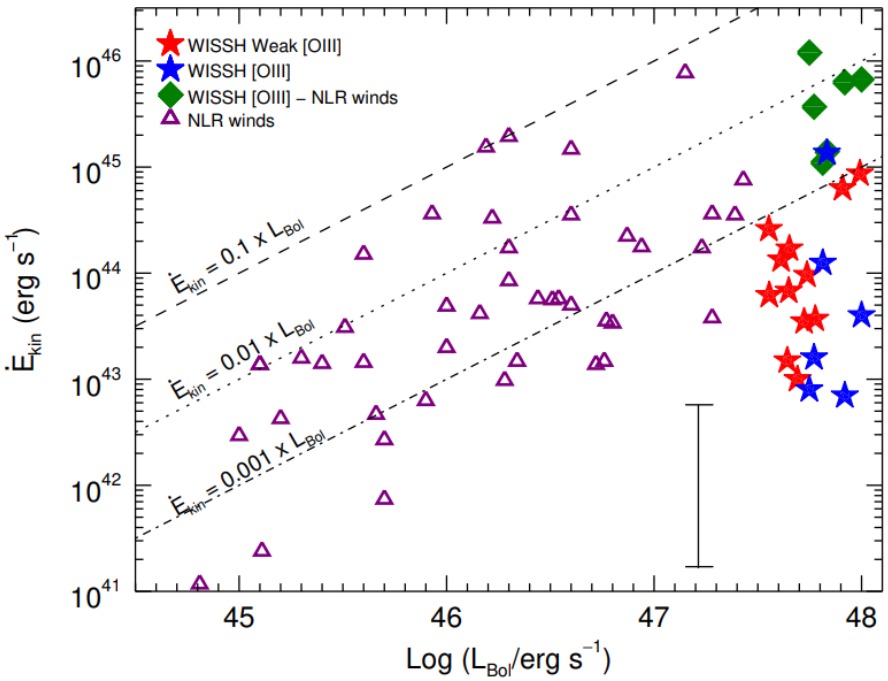

Figure 2.1: From Vietri et al. 2018 - Kinetic power of the CIV outflow component as a function of L_{bol} for the WISSH QSOs (red and blue stars) compared with WISSH NLR ionized outflows from Bischetti et al. 2017 (green diamonds) and other samples from literature (purple triangles). The error bar (bottom right corner) shows the maximum and minimum values obtained for $\dot{E}_{kin}$.

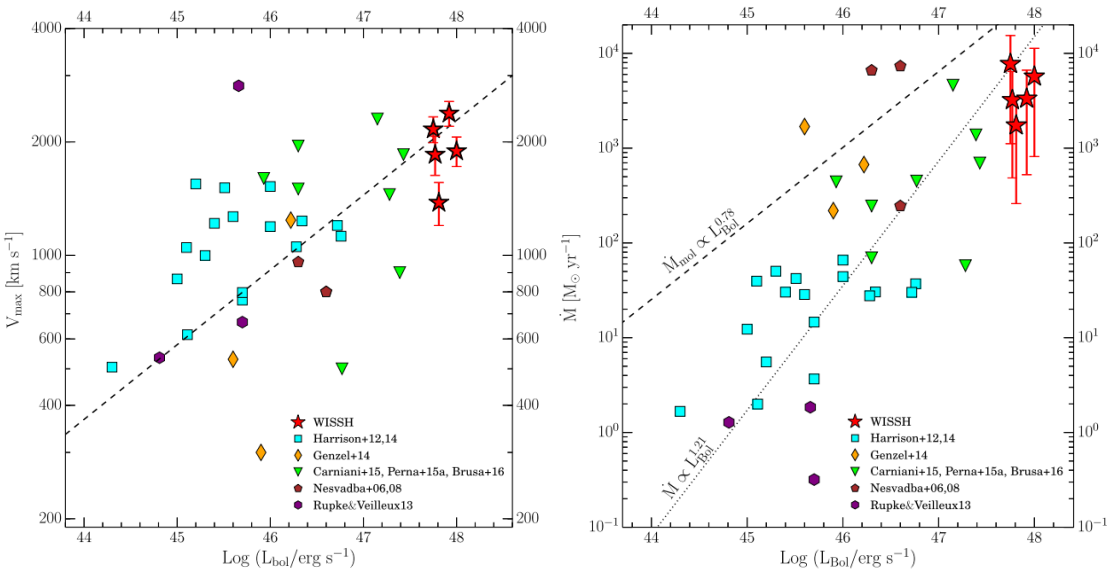

(a) (b)

Figure 2.2: From Bischetti et al. 2017 - *(Left)* Maximum velocity of the outflow versus the AGN L_{bol} of the WISSH quasars compared with other samples from literature. The dashed line represents the relation $L_{bol} \propto v_{max}^5$ (with arbitrary normalization) expected for energy conserving winds (see Costa et al. 2014). *(Right)* Mass rate of the ionised outflows as a function of L_{bol}. Values obtained for the WISSH quasars (red stars) are compared with other samples from literature. The dotted line corresponds to the best-fit relation $\dot{M} \propto L_{bol}^{1.21}$ derived for ionised outflows and the dashed line to the $\dot{M} \propto L_{bol}^{0.78}$ best-fit relation to molecular outflows.

2.2 BAL population in WISSH sample

Nuclear winds are manifested as UV Broad Absorption Lines (BAL) in $\sim 15\,\%$ of quasars.

Inspecting SDSS spectra of the whole WISSH sample and calculating the Balnicity Index $\left(\mathrm{BI} = -\int_{30\,000}^{60\,000} \left[1 - \frac{f(\nu)}{0.9}\right] C \, dv$ - where $f(\nu)$ is the continuum-normalised flux and the C factor can assume two values: 1 when the square bracket value is continuously positive and 0 otherwise$\right)$, Bruni et al. 2019 defined 21 BAL QSOs with $\mathrm{BI} > 0$. 21 out of 85 total quasars corresponds to $24 \pm 5\,\%$ of the sample, which is almost twice the average fraction in previous works (e.g. Gibson et al. 2009, who published results based on the SDSS DR5, Schneider et al. 2007 - Figure 2.3). Dai et al. 2008 find similar values in a 2MASS-selected sample, composed of more luminous objects due to the shallower nature of the survey. It could be a hint that the higher L_{bol} favours the acceleration of BAL outflows. Moreover, the WISSH sample exhibits a higher fraction of sources with higher velocities than Gibson et al. 2009, pointing toward a more efficient acceleration mechanism in

hyper-luminous quasars.

The kinetic power of BAL winds is also studied, deriving $\dot{E}_{kin} \geq 0.1\,\% L_{bol}$. Thus, some of these winds are able to transport kinetic power sufficient for generating a significant feedback contribution to the host galaxy.

Finally, Bruni et al. 2019 make a pilot study of the radio properties of the WISSH sample, cross-correlating it with the FIRST catalogue. 8/38 BAL sources and 20/85 total objects have radio counterpart. Moreover, radio properties of the WISSH sample suggest a similar jet-wind coupling with respect to lower-luminous sources (e.g. Shankar et al. 2008): the higher probability for the WISSH quasars to launch winds does not imply different jet formation rates or strength.

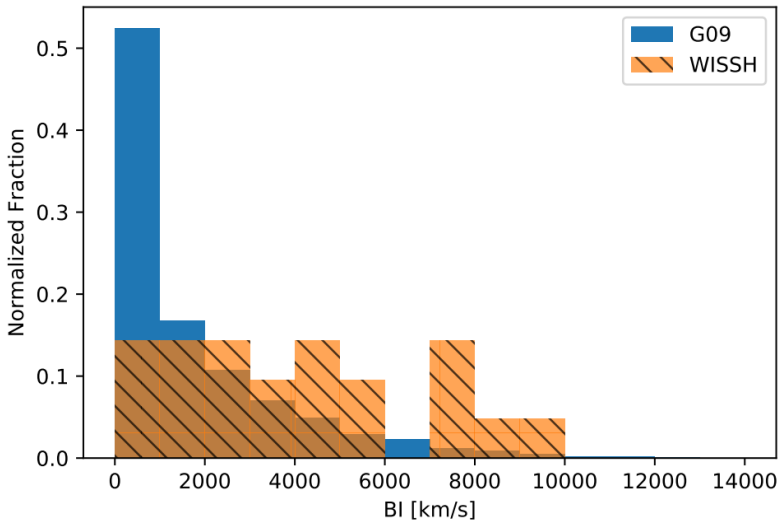

Figure 2.3: From Bruni et al. 2019 - CIV Balnicity Index distribution for the WISSH sample (orange) and the BAL QSOs catalogue from Gibson et al. 2009 (blue).

Among BAL sources, J1538+0855 ($z \approx 3.567$) exhibits widespread presence of outflows, as a BAL feature with maximum velocity $\sim 0.16c$ (Bruni et al. 2019). Variability of such multi-components BAL troughs is revealed by Vietri et al. 2022 through a detailed spectral analysis of SDSS, VLT, LBT and Subaru observations. They suggest that a combination of gas motion and changes in the ionisation state could explain the observed changeability. Inferring a characteristic flowing time, the kinetic power of the outflow $\dot{E}_{kin}$ is also calculated, resulting in $\dot{E}_{kin} \approx 0.1 - 10\,\% L_{bol}$. Moreover, the CGM regions around J1538+0855 are presented by Travascio et al. 2020 through the study of rest-frame UV emission lines, based on VLT/MUSE observations. The mass outflow rate derived from Lyα velocity shift is comparable with that obtained by Vietri et al. 2018 for the galactic-scale [OIII] wind, pointing towards an energy conserving scenario.

2.3 Red quasars

Fabian et al. 2008 identify a "forbidden region" in the $\lambda_{\rm Edd} - {\rm N_H}$ plane, defined by the Eddington limit ($\rm L_{Edd}$). Theoretically, it is explained to arise when the outgoing radiation pressure, due to electron scattering, balances the gravitational attraction due to the source mass. The forbidden region is expected to correspond to a "blowout region", where objects should be experiencing outflows. In the simplest case, assuming a gas of ionised hydrogen, the coupling with radiation is obtained via Thomson scattering. Thus, the corresponding Eddington limit includes the electron cross section $\sigma_{\rm T} \approx 6.65 \times 10^{-25}$ cm^2:

$$\rm L_{Edd} = \frac{4\pi GMm_p c}{\sigma_T} \tag{2.1}$$

where M is the mass acting through its gravitational force and $\rm m_p$ is proton mass.

In a more realistic scenario, partial ionisation and the presence of dust must be taken into account. As the frequency-weighted cross-section of dusty gas for interaction between radiation and matter ($\sigma_{\rm d}$) is larger than for electron scattering, radiation pressure is boosted by a factor $A = \sigma_{\rm d}/\sigma_{\rm T}$. Then, the relevant limit, defined as the *effective* Eddington limit $\rm L'_{Edd}$, is proportionally reduced. Assuming trapping of radiation to be negligible, for a column density $\rm N_H$ and a gas optically thin to Thomson scattering (Fabian et al. 2006)

$$\rm L'_{Edd} \approx \frac{L_{Edd}\tau_T}{\min[\tau_d, 1]} \tag{2.2}$$

where $\tau_{\rm T}$ and $\tau_{\rm d}$ are the optical depths for the corresponding cross sections: $\tau \equiv \sigma\, \rm N_H$. This means that a luminosity which is sub-Eddington for completely ionised gas, can exceed the modified Eddington limit.

Ishibashi et al. 2018 explicitly take into consideration the trapping of reprocessed radiation by dusty gas. In this case, the radiative force is

$$\rm F_{rad} = \frac{L}{c}\,(1 + \tau_{IR} - e^{-\tau_{UV}}) \tag{2.3}$$

where L is the accretion luminosity and $\tau_{\rm IR}$ and $\tau_{\rm UV}$ are the IR and UV optical depths. Depending on $\tau_{\rm IR}$ and $\tau_{\rm UV}$ values, three regimes can be identified: *(i)* $\tau_{\rm IR}$, $\tau_{\rm UV} \gg 1$ when photon trapping is present; *(ii)* $\tau_{\rm IR} \ll 1$ and $\tau_{\rm UV} \gg 1$ which is the single scattering limit; *(iii)* $\tau_{\rm IR}$, $\tau_{\rm UV} \ll 1$ (Ishibashi and Fabian 2015, Ishibashi and Fabian 2016). In Figure 2.4, maximal- and no-photon trapping regimes are represented as a black solid and dashed line, respectively, while the black horizon-

tal dotted line highlights $N_H = 10^{22}$ cm^{-2}. It can be seen that in the IR-optically thick regime, the forbidden area extends towards lower λ_{Edd}, especially for highly-obscured sources. Thus, a given column density can be removed by a lower Eddington ratio, and even Compton thick ($N_H \gtrsim 10^{24}$ cm^{-2}) columns can be potentially disrupted for $\lambda_{Edd} < 1$.

During their duty cycle, AGN move across the $\lambda_{Edd} - N_H$ plane. The sequence is reported in Figure 2.4: *(1)* galaxy wet merger starts the duty cycle; *(2)* dust and gas slide toward the central region, providing obscuration and efficiently accreting on the BH (feeding phase); *(3)* in the high-accretion/high-obscuration regime (forbidden region), intense feedback processes are expected, which end cleaning up the BH neighbourhood, allowing nuclear emission to emerge (blowout phase); *(4)* the fading phase is characterised by sporadic BH-feeding and ceasing star formation, as cold gas is exhausted; *(5)* the system finally evolves in a red passive elliptical galaxy. Ishibashi et al. 2018 estimate the typical blowout timescale to be of the order of 10^6 yr, suggesting a rather short phase. This is supported by the limited number of sources observed to occupy the forbidden area: in a sample of 392 local AGN from the *Swift*/BAT survey, assuming a no-photon trapping model, Ricci et al. 2017 found only $\sim 1\,\%$ of the objects; the fraction rises up to $\sim 8\,\%$ when including trapping of radiation, but considering the total enclosed mass (i.e. stellar, gas and black hole mass, instead of the BH one only), it would still imply $\sim 3\,\%$ of the sources to be in the forbidden region (Ishibashi et al. 2018).

Objects experiencing the theoretical transitional phase, during which BH surroundings and the whole galaxy are cleaned of obscuring gas, are dust-reddened sources. Thus, they are selected for having a color excess $E(B-V) > 0.15$. They exhibit reddened broad-line spectra, which have been missed for long by optical quasars surveys and recovered mostly through near-infrared observations (e.g. Glikman et al. 2012, Banerji et al. 2012, Brusa et al. 2014).

They constitute a unique population ($20-30\,\%$ - Glikman et al. 2018) of Type 1 objects, for which many studies have found distinctive properties indicating that they are intrinsically different from their bluer counterparts. Red quasars exhibit significantly enhanced compact radio emission (e.g. Klindt et al. 2019, Rosario et al. 2020, Fawcett et al. 2020) which may be linked to shocks from winds (e.g. Hwang et al. 2018, Rosario et al. 2021); they are associated with higher-velocity outflows of ionised gas (e.g. Urrutia et al. 2009, Perrotta et al. 2019, Temple et al. 2019, Vayner et al. 2021, Rivera et al. 2021, Monadi et al. 2022) and may have a different luminosity function (e.g. Banerji et al. 2015). Other properties identify red quasars as good candidates for the missing transitional phase: they are found to be predominantly driven by major mergers (e.g. Urrutia et al. 2008, Glikman

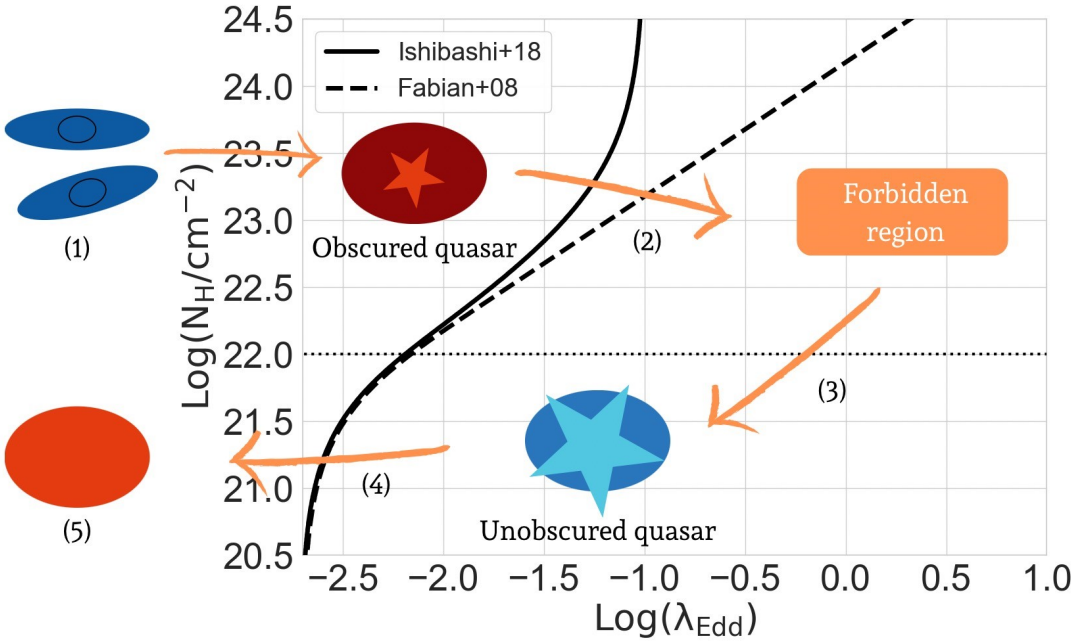

Figure 2.4: AGN duty cycle, from major merger to a red elliptical galaxy, on the $\lambda_{\rm Edd} - {\rm N_H}$ plane. Black solid and dashed lines are Ishibashi et al. 2018 and Fabian et al. 2008 relation, derived from a maximal- and no-photon trapping model, respectively. The black horizontal dotted line highlights ${\rm N_H} = 10^{22}$ cm^{-2}.

et al. 2015, Zakamska et al. 2019), are accreting at very high rates (e.g. Kim et al. 2015) and sometimes exhibit BAL features typically associated with outflows (e.g. Urrutia et al. 2009). However, in a large systematic study of broad-band SED, Rivera et al. 2021 find consistent column densities between red and blue quasars in SDSS. All of these evidences point towards a different physical mechanism for the reddening with respect to the orientation-based extinction typical of Type 2 quasars.

7/85 WISSH QSOs exhibit $\rm E(B-V) > 0.15$ and are classified as red sources. Their ID, SDSS ID and color excess (from Saccheo et al. 2023) are reported in Table 2.3.

ID	SDSS ID	E(B − V)
WISSH25	J1025+2454	0.17
WISSH34	J1110+1930	0.38
WISSH40	J1157+2724	0.15
WISSH49	J1220+1126	0.25
WISSH58	J1326−0005	0.23
WISSH66	J1447+1038	0.17
WISSH74	J1554+1109	0.34

Table 2.3: WISSH red QSOs: ID; SDSS ID; color excess (Saccheo et al. 2023).

2.4 FIR and sub-mm emission

The far IR coverage is provided by Herschel for 16 QSOs, while ALMA, NOEMA and JVLA observed the $\sim 30 - 350$ GHz frequency range for nine WISSH sources (five of which are among those with available Herschel data). Bischetti et al. 2021 presented a systematic study of the rest-frame FIR continuum and CO and [CII] emission lines, tracing cold gas content in eight WISSH quasars.

Bischetti et al. 2021 estimate the gas mass content from CO luminosity, finding $M_{gas} = 4.4 \times 10^9 - 3.5 \times 10^{10}$ $M_\odot$. That confirms the variety of properties in gas reservoir that has been found in previous studies (e.g. Perna et al. 2018). Given the gas mass content and the SFR, Bischetti et al. 2021 derive the depletion time as $\tau_{dep} = \frac{M_{gas}}{SFR}$ finding $\tau_{dep} < 100$ Myr and down to ~ 20 Myr. These values are ~ 30 times shorter compared to the typical depletion timescales in main sequence galaxies of similar stellar mass and redshift. Thus, it may be due to AGN feedback reducing gas reservoir or starburst activity in the host galaxy of the targets (e.g. Aravena et al. 2016, Yang et al. 2017).

For the eight WISSH QSOs studied by Bischetti et al. 2021, a black hole mass estimate is available from single epoch methods based on the Hβ or MgII emission lines. They derive $M_{dyn}/M_{BH} \approx 3 - 10$ (where M_{dyn} is the dynamical mass), which are among the smallest values measured so far. Small values are expected in the early growth phases ($z > 3$) of very massive BH, in the scenario in which black hole accretion is triggered by galaxy interactions (e.g. Lamastra et al. 2010, Menci et al. 2014). Following the local relation (e.g. Jiang et al. 2011), M_{BH} found in WISSH sources would correspond to a dynamical mass $\sim 10^{12}$ $M_\odot$. For $\sim 80\,\%$ of the targets, at least one line emitter is found within $\sim 6 - 40$ kpc, with a CO luminosity (L_{CO}) $\sim 3 - 5$ times lower or at most equal to the QSO one. Bischetti et al. 2021 notice that summing the host galaxy and companion dynamical mass, M_{dyn}/M_{BH} approaches the local relation, suggesting that giant galaxies at $z \approx 0$ assembled through mergers in the location of hyper-luminous QSOs (Figure 2.5a). A particularly significant example is provided by J1015+0020 ($z = 4.407$), around which an extreme overdensity of star-forming galaxies is found (Bischetti et al. 2018): five continuum and line emitters are present at an angular distance < 3.5 arcsec.

Finally, Bischetti et al. 2021 study the gas fraction of the sample defined as $f_{gas} = \frac{M_{gas}}{M_*}$, where M_* is the stellar mass. Assuming the dark matter to be a negligible contribution, they find $f_{gas} = 0.04 - 1.6$. The wide range in terms of gas fraction properties confirms previous high-redshift results (e.g. Banerji et al. 2018, Venemans et al. 2017). Moreover, these values are are $10 - 100$ times smaller than

in star-forming galaxies with the same stellar mass (Figure 2.5b). Thus, Bischetti et al. 2021 suggest that AGN feedback is responsible for depleting the host galaxy of the molecular gas content via outflows (e.g. Brusa et al. 2015, Perna et al. 2018). The widespread observations of different phases outflows in the WISSH sample supports this scenario.

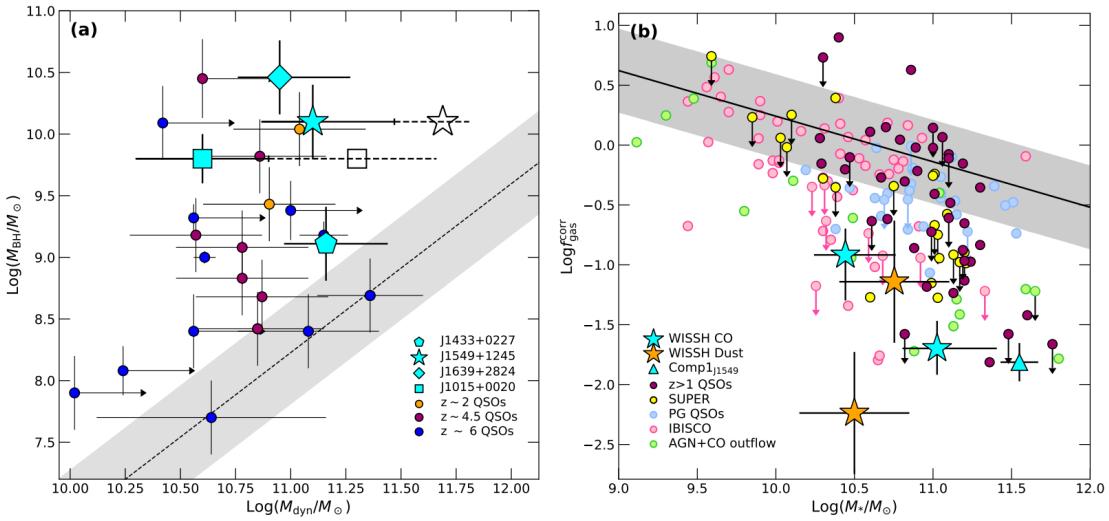

Figure 2.5: From Bischetti et al. 2021 - *(Left)* Black hole mass as a function of the dynamical mass of WISSH QSOs (cyan symbols), compared with $z \sim 2-6$, luminous QSOs from literature. The total dynamical mass associated with the QSO + companion galaxies with measured M_{dyn} are also shown by the empty symbols. The $M_{BH} - M_{dyn}$ relation found for local galaxies by Jiang et al. 2011 is also indicated by the dashed line, with the associated 0.4 dex intrinsic scatter (shaded region). *(Right)* Molecular gas fraction as a function of the host-galaxy stellar mass for WISSH QSOs and a compilation of high-z QSOs and local AGN. WISSH QSOs with dust-based M_{gas} are indicated by orange stars. The average $f_{gas} - M_*$ relation found for $z < 4$ star-forming galaxies from the PHIBSS survey (Tacconi et al. 2018) is shown as the solid line.

2.5 X-ray emission

X-ray Chandra (34 observations) and XMM-Newton (7 observations) data for 41/85 ($\sim 48\,\%$) WISSH sources were presented by M17. They use 33 archival and 8 proprietary observations. 6/41 objects result to be undetected. For the remaining ones, spectroscopic analysis is performed for the 21 quasars with ≥ 40 counts, in addition to Hardness Ratio (HR) analysis for all of the sources. The HR is defined as

$$HR = \frac{H - S}{H + S} \tag{2.4}$$

where S and H are the number of spectral counts in the soft ($0.5-2$ keV) and hard ($2-8$ keV) X-ray band, respectively. It is a proxy of the X-ray spectral shape.

Most of the sources ($\sim 90\,\%$) exhibits negative HR values, pointing towards limited absorption in the WISSH sample. M17 confirm this result deriving column density estimates from spectra obtained using WebPIMMS[1]: $\sim 70\,\%$ of WISSH QSOs show $N_H \leq 5 \times 10^{22}$ cm^{-2}.

Performing spectral fitting, a simple power-law model with Galactic absorption is applied to 13/21 ($\sim 60\,\%$) sources, while the remaining ones need an additional absorbing component. The majority of the objects shows $\Gamma \approx 1.8$, as expected for AGN emission (e.g. Piconcelli et al. 2005). From spectral analysis, 14/21 quasars exhibit little or no intrinsic absorption $N_H <$ few 10^{22} cm^{-2}. Considering the whole X-ray WISSH sample and either spectral or HR analysis, $\sim 60\,\%$ of the sources are unobscured, while $\sim 23\,\%$ are moderately obscured (i.e. 10^{22} cm$^{-2} \leq N_H \leq 10^{23}$ cm^{-2}).

The 2−10 keV flux ranges between 7×10^{-15} erg s^{-1} cm^{-2} and few 10^{-13} erg s^{-1} cm^{-2}, and more than $80\,\%$ of the sources exhibits $F_{2-10} \approx 10^{-14} - 10^{-13}$ erg s^{-1} cm^{-2}. The majority of the sources exhibits intrinsic (i.e. corrected for obscuration) X-ray luminosity in the range 10^{45} erg s^{-1} $< L_{2-10} < 10^{46}$ erg s^{-1}.

Given the X-ray and bolometric luminosities, they calculate X-ray bolometric correction as

$$k_{bol,X} = \frac{L_{bol}}{L_{2-10}} \tag{2.5}$$

and represent it in the $k_{bol,X} - L_{bol}$ plane - Figure 2.6. WISSH sources are well described by the Lusso et al. 2012 relation, although with a large scatter. The Spearman's rank test gives a rank coefficient of $p = 0.7$, and the probability of deviation from a random distribution is $d_s < 10^{-20}$, confirming that a strong correlation is present. A decrease in the relative contribution of X-ray emission to bolometric luminosity is observed at increasing L_{bol}. In case of Type 1 sources, as WISSH QSOs, for which $L_{UV} \sim L_{bol}$, it means that the relative importance of coronal emission decreases compared to the accretion disk one. Thus, this trend highlights the AGN X-ray weakening for high-luminosity sources.

Optical/UV and X-ray emissions can be directly compared through monochromatic luminosities. M17 calculate the X-ray - to - optical index

$$\alpha_{OX} = \frac{\mathrm{Log}(L_{2\,keV}/L_{2500})}{\mathrm{Log}(\nu_{2\,keV}/\nu_{2500})} \tag{2.6}$$

where $L_{2\,keV}$ and L_{2500} are the monochromatic luminosities at 2 keV and 2500 Å, respectively, while $\nu_{2\,keV}$ and ν_{2500} are the corresponding frequencies. α_{OX} is a virtual slope connecting the blue-bump due to disk emission and the soft X-ray at

[1] `https://cxc.harvard.edu/toolkit/pimms.jsp`

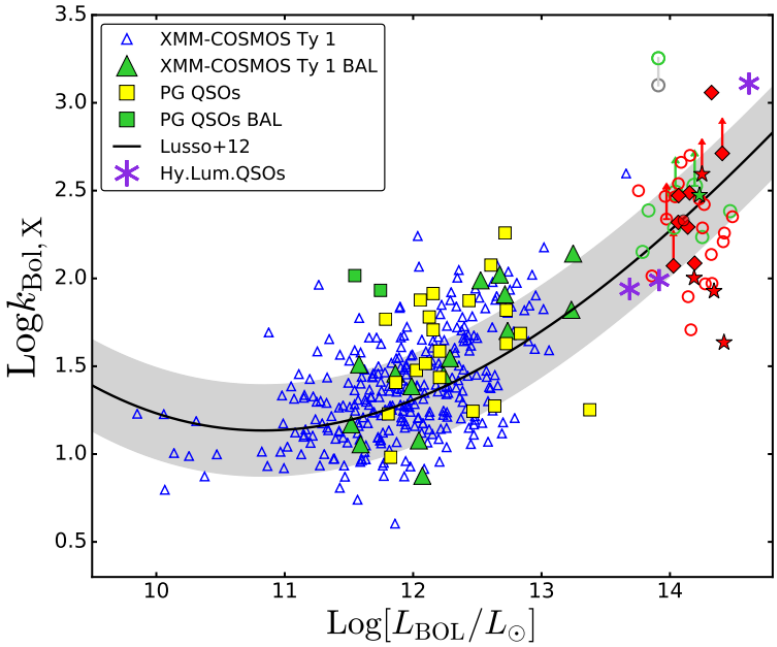

Figure 2.6: From M17 - Bolometric correction in the $2-10$ keV band as a function of the bolometric luminosity. BAL WISSH quasars are represented with green symbols while non-BAL WISSH are represented with red symbols. Filled symbols indicate objects which have LBT/LUCI optical spectrum. Star and diamond symbols indicate the presence of broad [OIII] emission lines and CIV shifts > 2000 km s^{-1}, respectively. Blue triangles indicate the Broad-line AGN sample from the XMM-COSMOS survey by Lusso et al. 2012. The yellow squares indicate PG quasars while green symbols represent BAL AGN. Violet asterisks indicate the hyper luminous quasars ULASJ 1539+0557, ULASJ 2315+0143 and 2QZ0028-2830. The black solid curve represents the relation found by Lusso et al. 2012 for type 1 AGN, while the gray shaded area indicates the 1σ dispersion on the relation. Two values for the hard X-ray luminosity of J0045+1438 (i.e. the object with the lowest X-ray luminosity in M17 WISSH sample) are reported, connected by a gray line. L_{2-10} are calculated by using their best fit value of N_H (i.e. 4×10^{22} cm^{-2}, green open circle) and their upper error (i.e. $N_H = 1.5 \times 10^{23}$ cm^{-2}, gray open circle), respectively.

representative wavelengths. It is clearly marked in red in Figure 2.7 from Lusso et al. 2023, where a complete AGN SED is modelled.

More negative α_{OX} values trace steeper slopes, thus more prominent optical-UV emission compared to the X-ray one, or, equivalently, weaker X-ray sources. M17 also extend the $L_{2500} - \alpha_{OX}$ relation towards the highest luminosity end - Figure 2.8. The decreasing trend of α_{OX} at increasing L_{2500} is confirmed by the Spearman's rank test (p = -0.75, $d_s \sim 10^{-20}$) and a new best-fit is found to the data with the inclusion of WISSH sources:

$$\alpha_{OX} = (-0.172 \pm 0.006)\,\mathrm{Log}(L_{2500}/\mathrm{erg\,s^{-1}\,Hz^{-1}}) + (3.72 \pm 0.17) \qquad (2.7)$$

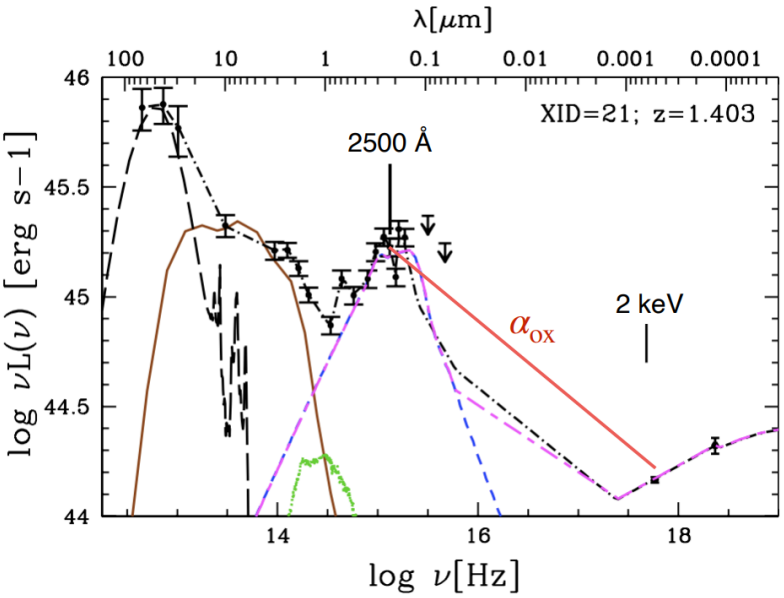

Figure 2.7: From Lusso et al. 2023 - Example of full AGN SED from far-IR to X-rays at redshift 1.4 from the XMM-COSMOS survey. The rest-frame data, used to construct the total SED (shown with a black dot-dashed line), are represented with black points. Various lines represent the different models adopted to describe the data. Specifically, the black long-dashed, brown solid, green dotted, and blue dashed lines correspond to the best-fit starburst, hot-dust from reprocessed AGN emission, host-galaxy, and the empirical disk templates, respectively. The magenta short-long dashed line is the best-fit empirical disk template with the inclusion of X-rays. The rest-frame 2500 Å and 2 keV are marked, as well as a representation of the α_{OX} index for this object (red solid line).

where the errors indicate 1σ significance. Such anti-correlation between the two parameters is a further indication of AGN X-ray weakening for higher-luminosity sources.

WISSH QSOs are selected to be among the most luminous sources in the WISE 22 μm band, therefore extending towards the higher-luminosity regime all the relations involving MIR luminosity. X-ray emission can be represented as a function of mid-IR one. Indeed, the two emissions are strictly correlated as the former is the portion of nuclear emission which is Compton scattered by the hot corona, while the latter is the fraction reprocessed and re-emitted by dust in the torus. M17 refer to $\lambda L_{6\,\mu m}$ (the spectral band where the heated dust emission peaks) as a proxy for MIR radiation. From the SED fitting, Duras et al. 2017 derive 6×10^{46} erg s^{-1} $\lesssim L_{6\,\mu m} \lesssim 3 \times 10^{47}$ erg s^{-1}. A strong correlation is found in the $L_{2-10} - L_{6\,\mu m}$ plane (Figure 2.9), although in MIR-luminous sources X-ray contribution to bolometric luminosity decreases with respect to the MIR one. They hypothesise the low $\frac{L_{2-10}}{L_{6\,\mu m}}$ to be caused by strong AGN-heated, hot dust emission typically observed in the mean SED of hyper-luminous quasars (Krawczyk et al. 2013). Moreover, a large dispersion in the X-ray luminosity at a given MIR lu-

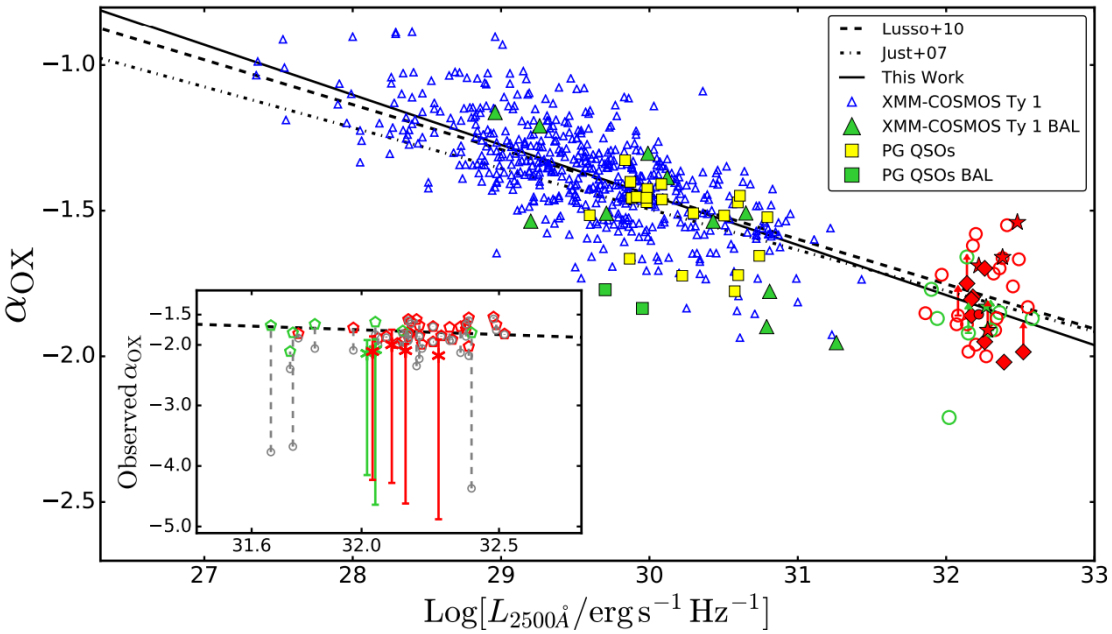

Figure 2.8: From M17 - α_{OX} values as a function of extinction-corrected 2500 Å monochromatic luminosities. BAL WISSH quasars are represented with green symbols while non-BAL WISSH are represented with red symbols. Filled symbols indicate objects which have LBT/LUCI optical spectrum. Star and diamond symbols indicate the presence of broad [OIII] emission lines and CIV shifts > 2000 km s^{-1}, respectively. Blue triangles indicate the Broad-line AGN sample from the XMM-COSMOS survey by Lusso et al. 2010, while the yellow squares indicate PG quasars. Green symbols represent BAL AGN. The dashed line represents the relation found by Lusso et al. 2010, the dash-dot one represents the Just et al. 2007 relation while the black solid line indicates M17 linear fit. In the inset on the lower left corner of the figure, open pentagons indicate absorption-corrected α_{OX} values, while gray open circles indicate α_{OX} values when X-ray absorption is not taken into account. Asterisks with error bars indicate α_{OX} values for the undetected WISSH sources, calculated with M17 N_H median value of the sample. The error bars were calculated using $N_H = 0$ and $N_H = 4 \times 10^{23}$ cm^{-2}, i.e. their maximum value of the sample.

minosity is observed around previously found relations (e.g. Lanzuisi et al. 2009, Stern 2015, Chen et al. 2017). It results in an over-/under-estimation of one parameter when using a universal relation to describe the whole luminosity range.

For 14/41 ($\sim 35\,\%$) sources, a black hole mass estimate derived from the Hβ line is available (Bischetti et al. 2017, Vietri et al. 2018). For the remaining ones M_{BH} is obtained from CIV (Weedman et al. 2012), but M17 stress that using the CIV line may lead to an overestimate of the black hole mass up to a factor of ~ 5 (Coatman et al. 2017). WISSH QSOs extend the studied black hole mass range towards the poorly investigated more massive end. M17 inspect the relation between Γ and λ_{Edd} (Figure 2.10), for which Shemmer et al. 2008 and Brightman et al. 2013 report the existence of a positive correlation. WISSH data are broadly

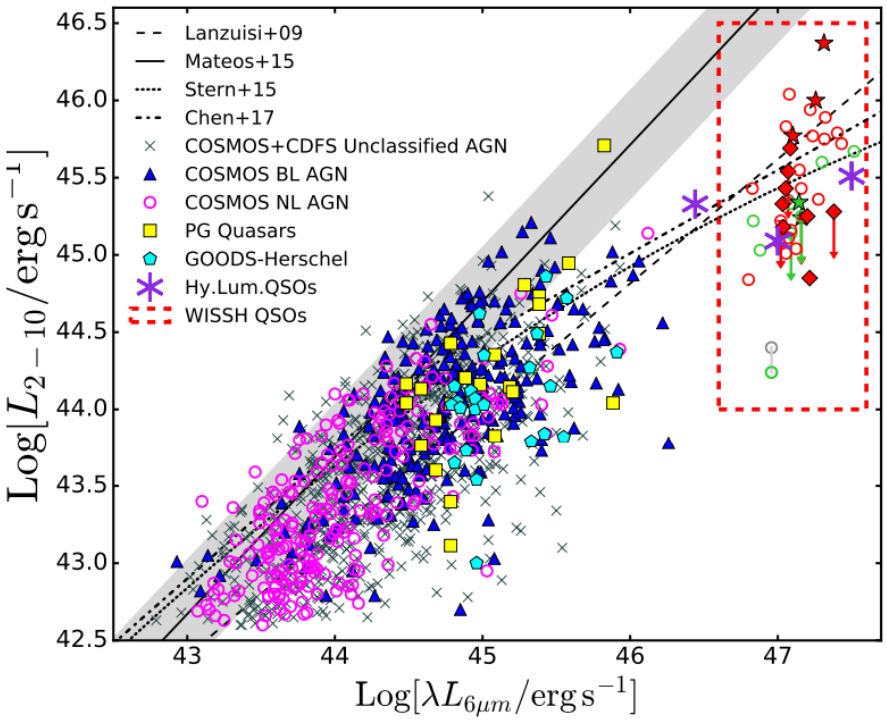

Figure 2.9: From M17 - Absorption-corrected $2-10$ keV luminosity as a function of MIR luminosity at 6 μm. WISSH QSOs are reported along with lower-luminous comparison samples. BAL WISSH quasars are represented with green symbols while non-BAL WISSH are represented with red symbols. Filled symbols indicate objects which have LBT/LUCI optical spectrum. Star and diamond symbols indicate the presence of broad [OIII] emission lines and CIV shifts > 2000 km s^{-1}, respectively. The black solid, dashed, dotted and dash-dotted lines represent the Mateos et al. 2015, Lanzuisi et al. 2009, Stern 2015 and Chen et al. 2017 relations, respectively. The grey shaded area indicates the intrinsic scatter about the Mateos relation. The red dashed line box indicates the locus of the WISSH quasars.

consistent with the other samples, but there is a large dispersion around the best fits, especially in $-1 \leq \log \lambda_{\rm Edd} \leq 0$.

2.5.1 Accretion disk - corona interplay

The fastest and most energetic winds have been reported in hyper-luminous quasars (e.g. Vietri et al. 2018, Fiore et al. 2017, Wu et al. 2011, Meyer et al. 2019, Perrotta et al. 2019). On this basis, Zappacosta et al. 2020 explore the relation between the extreme radiative field of the hyper-luminous WISSH sources and their X-ray coronal properties, interpreting the results in the context of the accretion disk wind scenario.

They find a strong correlation between hard X-ray luminosity (L_{2-10}) and the blueshifted velocity of the CIV emission line (indicative of accretion disk winds): the sources with the largest negative $v_{\rm CIV}$ (i.e. larger blueshifts) are X-ray weaker.

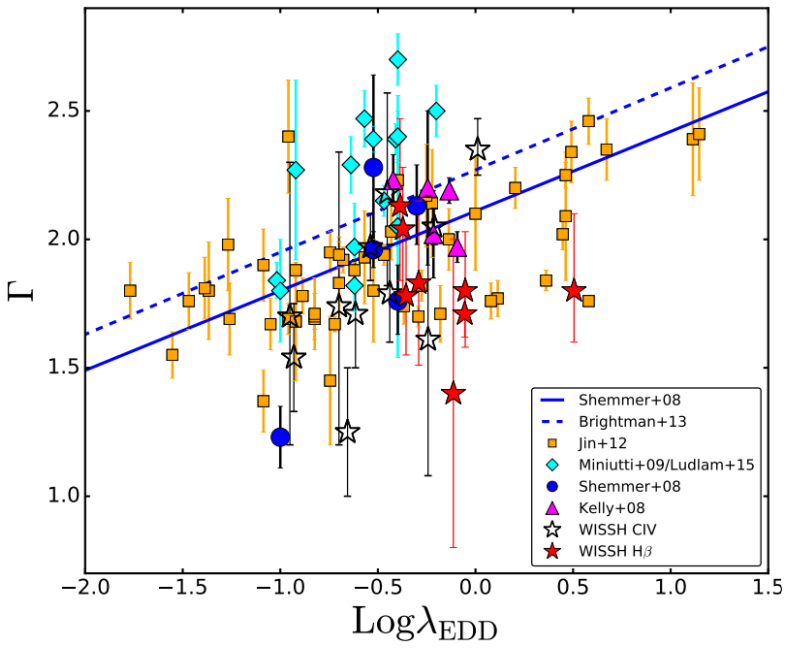

Figure 2.10: From M17 - X-ray photon index as a function of λ_{Edd} for the WISSH quasars with X-ray spectroscopy (filled stars indicate objects with a Hβ-based SMBH mass - Bischetti et al. 2017, Vietri et al. 2018), while open stars indicate sources with a CIV-based SMBH mass (Weedman et al. 2012). Comparison samples are also reported. The blue solid line represents the relation found by Shemmer et al. 2008, while the blue dashed line represents the relation by Brightman et al. 2013. Orange squares mark the AGN from Jin et al. 2012; magenta triangles and blue circles represent high-z quasars from Kelly et al. 2008 and Shemmer et al. 2008, respectively. Errors on Γ are consistently reported at 90 % confidence level for all the sources.

It is reported in Figure 2.11.

Zappacosta et al. 2020 interpret their results in the context of a magnetohydrodynamical (MHD) or radiative scenario. *MHD scenario:* the X-ray flux is an ionising source, able to determine the distance from the SMBH at which CIV atoms can exist. The higher L_{2-10}, the farther CIV can be accelerated: thus, more luminous sources exhibit slower disk winds than X-ray weaker ones. Moreover, to avoid over-ionisation, inner shield of partially ionised gas is needed in the UV winds to absorb X-ray flux. *Radiative scenario:* radiation pressure on spectral lines drives the UV winds. Failed winds act as a shield for the gas to avoid over-ionisation and the drop of gas opacity to UV transitions. Higher L_{2-10} corresponds to vaster failed wind shielding region, thus disk winds can be accelerated only at large radii. On the other hand, weaker X-ray fluxes produce smaller failed wind zones and the CIV outflows can be accelerated closer to the SMBH, reaching faster velocity. Moreover, dense failed winds repositories may contribute to the coronal cooling via Bremsstrahlung, resulting in a weakening/quenching of its X-ray emission. Zappacosta et al. 2020 notice that the radiative scenario would produce a

correlation between the obscuring column density and the UV blueshifted velocity, but no significant dependence is observed between the quantities. Furthermore, semi-relativistc BAL winds have been revealed in weakly/moderately absorbed sources.

Orientation may play a role in producing the scatter in the $L_{2-10} - v_{CIV}$ relation: it may reflect the projection of the wind velocity field depending on the line of sight inclination of the accretion disk - corona system. X-ray variability could also account for the observed scatter: Matzeu et al. 2017 report on a positively correlated variability between UFO velocity and X-ray luminosity exhibited by PDS 456, a luminous ($L_{bol} \approx 10^{47}$ erg s^{-1}, similarly to WISSH sources) low-redshift ($z = 0.184$) quasar. Based on photoionisation and radiative transfer calculations, Dannen et al. 2019 point out, though, that the line-driving mechanisms may not be relevant in plasma with high ionisation parameters typical of UFOs. In this case, MHD-driven winds may be a viable mechanism (e.g. Fukumura et al. 2018).

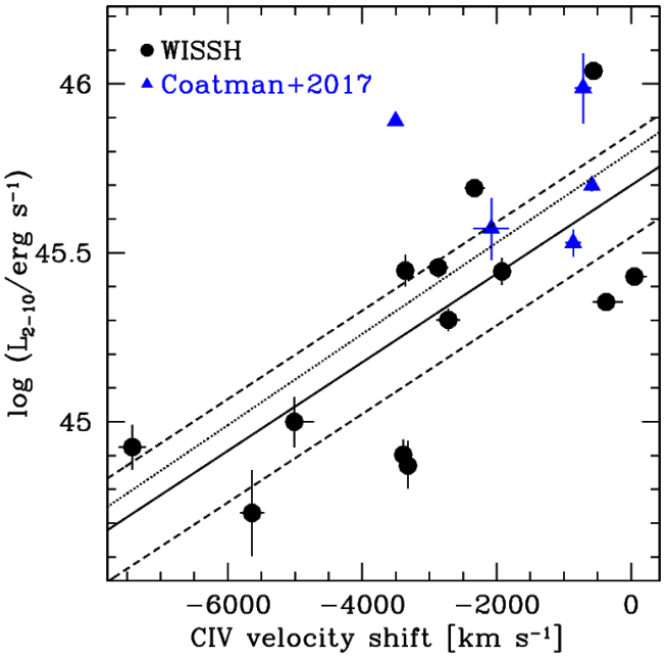

Figure 2.11: From Zappacosta et al. 2020 - L_{2-10} as a function of v_{CIV} for the WISSH quasars (black circles) and hyper-luminous QSOs at $z = 2 - 3$ (blue triangles).

2.6 WISSH Spectral Energy Distribution

Combining SDSS, 2MASS, WISE and Herschel/SPIRE observations, Duras et al. 2017 perform the SED fitting for 16 WISSH sources. The fitting procedure of the collected 15 spectral bands (from UV to FIR) is based on the standard reduced χ^2 minimisation.

To most of the sources a two-components modelling is applied, comprising the accretion disk emission (both direct and reprocessed by the dusty torus - f_{AD+T}) and the cold dust emitting in the FIR bands (f_{CD}). $\sim 31\,\%$ of the sample exhibits a NIR excess and an additional component is included (f_{NE}), representing hot dust heated by the central source, although the physical origin of NIR excess is not yet clear. The complete model applied is the following:

$$f_{model} = Af_{AD+T} + Bf_{CD} + Cf_{NE} \tag{2.8}$$

where A, B and C are normalisation factors.

A lot of parameters concerning nuclear emission and/or the host galaxy can be derived once SED fitting is available:

Bolometric luminosity is calculated integrating the accretion disk emission in the range 60 Å $-$ 1 μm, as follows

$$L_{bol} = 4\pi d_L^2 \int_{60\ \text{Å}}^{1\ \mu\text{m}} Af_{AD}\ [\text{erg}\,\text{s}^{-1}] \tag{2.9}$$

where d_L is the luminosity distance;

Star Formation Rate is estimated from IR luminosity of the host galaxy, due to reprocessed UV luminosity by dust. Integrating the modified black body model in the range $8 - 1000$ μm, they calculate the IR luminosity:

$$L^{host}_{IR\,(8-1000)\,\mu m} = 4\pi d_L^2 \int_{8\ \mu\text{m}}^{1000\ \mu\text{m}} Bf_{CD}\ [\text{erg}\,\text{s}^{-1}] \tag{2.10}$$

Then, assuming a Chabrier Initial Mass Function (IMF) and using the relation by Kennicutt 1998, they obtain

$$SFR = 10^{-10} \frac{L^{host}_{IR\,(8-1000)\,\mu m}}{L_\odot} = 400 - 4500\ M_\odot\,yr^{-1} \tag{2.11}$$

Duras et al. 2017 notice that these values are upper limits, as they are calculated assuming all FIR emission to be produced by young stars.

Duras et al. 2017 debate whether FIR emission is mainly powered by starburst, or a quasar is also required. Following Schneider et al. 2015, they use TRADING radiative transfer simulations, choosing as the central source the nuclear and torus emission best fit. The dust in the host galaxy is modelled as a spheroidal inhomogeneous distribution extending from just outside the dusty torus up to few kpc.

Considering the least and most luminous sources, they estimate the QSOs contribution to FIR flux to be $\sim 43\,\%$ and $\sim 60\,\%$ respectively. Thus, an average quasar contribution of $\sim 50\,\%$ is assumed and the SFR can be derived from Equation 2.11 simply dividing by a factor of 2.

Saccheo et al. 2023 extend the SED fitting to the whole WISSH sample: the resulting mean SED for the WISSH sample is shown in Figure 2.12. The aim of the SED fitting procedure is to uncover eventual peculiar properties of hyper-luminous QSOs compared to the bulk of quasar population.

Referring to Bruni et al. 2019 for the classification of WISSH sources as BAL or non-BAL QSOs, Saccheo et al. 2023 separately study the mean SED of the two categories focusing on the objects with available X-ray data. They observe the main differences between BAL and non-BAL quasars to be in the X-ray and optical/UV regions. In particular, BAL sources are X-ray weaker. This variation seems to be intrinsic, as it is present even after absorption correction, as shown by previous works (e.g. Brandt et al. 2000, Gallagher et al. 2002, Gallagher et al. 2007, Fan et al. 2008, Luo et al. 2014).

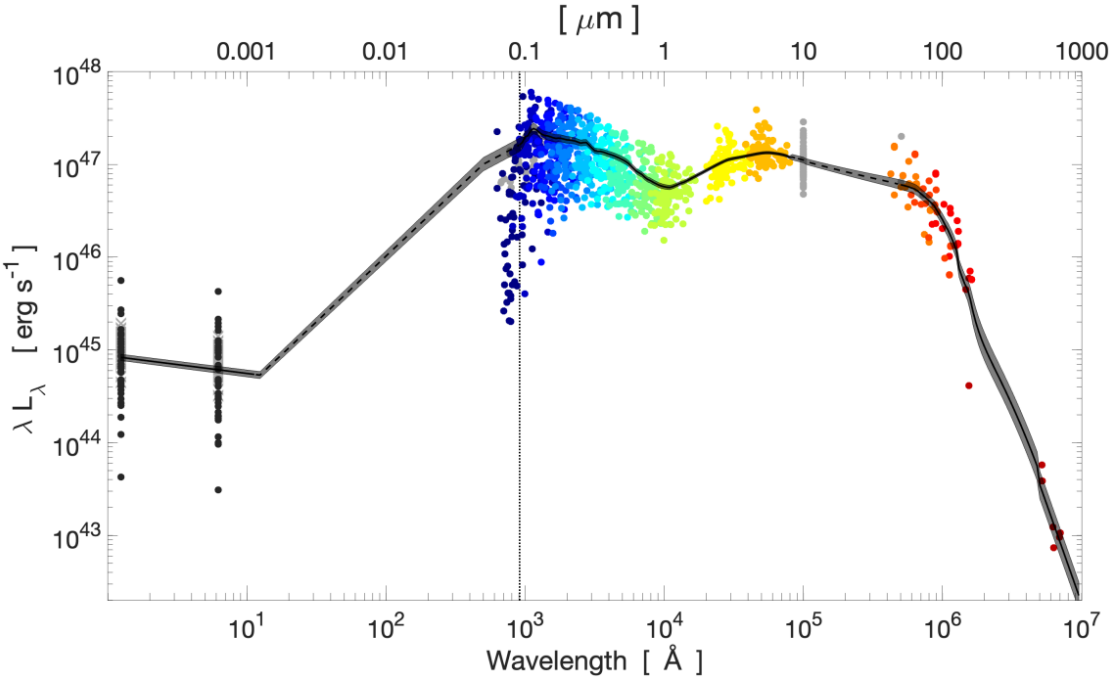

Figure 2.12: From Saccheo et al. 2023 - Mean SED derived from the WISSH sample. The shaded area gives the 68 % confidence interval. The colored circles represent available data points, color-coded according to the filter in which they were observed. Photometry obtained by Gap Repair (i.e. substituting photometric points likely affected by BAL absorption with non-absorbed data, using the mean SED by Krawczyk et al. 2013 normalised to the nearest available filter) is represented as grey circles. The grey crosses indicate X-ray luminosities reconstructed from the α_{OX} relationship. The dotted black line indicates the Lyman limit $\lambda L = 912$ Å: for shorter wavelengths the mean SED was truncated and extended as explained in the text.

3

X-ray satellites and data analysis

The current Chapter introduces XMM-Newton and Chandra X-ray telescopes and their data analysis threads. In Section 3.1, the two satellites are presented, along with their strengths and limitations. Section 3.2 summarises X-ray data reduction for the two telescopes.

3.1 An introduction to X-ray telescopes

Since the birth of X-ray astronomy, specific techniques were developed to perform observations, as conventional refracting or reflective optical-like telescopes are impractical. X-ray photon energies are higher than the binding energies of the typical atomic electrons, leading to a refractive index for X-rays being less than unity. Thus, single-surface reflectivity for near-normal incidence is negligible. However, by Snell's laws, total external reflection occurs and X-rays can be reflected from a surface up to a critical angle defined as

$$\theta_{\mathrm{cri}} \propto \frac{\sqrt{\rho}}{\mathrm{E}} \tag{3.1}$$

where ρ is the density of the mirror's material and E is the energy of the incident photon. It is evident that more energetic photons need smaller incidence angles to be effectively reflected. This requirement determines the way in which X-ray telescopes are designed: nesting coaxial and co-focal mirror shells causing an almost tangential impact direction for the radiation - Figure 3.1. In particular, Wolter I grazing-incidence mirrors are typically used, i.e. couples of a parabolic and an hyperbolic reflecting surface. The higher number of shells increases the collecting area ($\mathrm{A_{geom}}$) of the telescope. For grazing incidence X-ray telescopes, $\mathrm{A_{geom}}$ is only the sum of the areas of the annuli presented to the sky (i.e. the aperture of the

telescope), which is much lower than the mirrors' surface area.

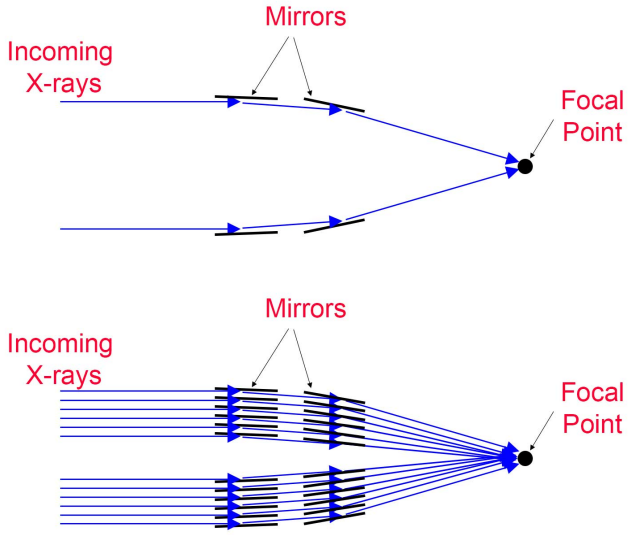

Figure 3.1: Diagram of a cut-away of an X-ray telescope with one and several sets of mirrors (*top* and *bottom panel*, respectively). The incoming X-rays bounce off the two mirrors with a grazing incidence to be focused at the focal point (Credits: NASA's Imagine the Universe).

Different effects cause the geometric area (A_{geom}) of a telescope to be reduced to a smaller effective area (E_a). E_a is defined as follows:

$$E_a\big(E, q, (x, y)\big) = A_{geom} \times R(E) \times V\big(E, (x, y)\big) \times QE\big(E, (x, y)\big) \tag{3.2}$$

where R(E) is the reflectivity of the mirrors, which depends on the photon energy as in Equation 3.1; $V\big(E, (x, y)\big)$ is the vignetting, which represents the reduced ability to collect photons at large distances from the aimpoint (large off-axis angles) and becomes stronger in the hard X-ray band; $QE\big(E, (x, y)\big)$ is the quantum efficiency, which is related to detector's response. XMM-Newton *(left panel)* and Chandra *(right panel)* on-axis effective areas are shown in Figure 3.2. During data reduction, information on the effective area is taken into account creating the Ancillary Response File (ARF) matrix - *left panel* in Figure 3.3.

The instrument response as a function of energy is contained in the Redistribution Matrix File (RMF) - *right panel* in Figure 3.3.

A fundamental property of a (X-ray) telescope is the sensitivity, which is the measure of the minimum signal that a telescope can distinguish above the random background noise. It is defined as

$$\text{sensitivity} = \frac{S}{\sqrt{S+N}} = \frac{S}{\sqrt{S + \left(N^2_{sky} + N^2_{dark\,curent} + N^2_{read\,out}\right)^{1/2}}} \tag{3.3}$$

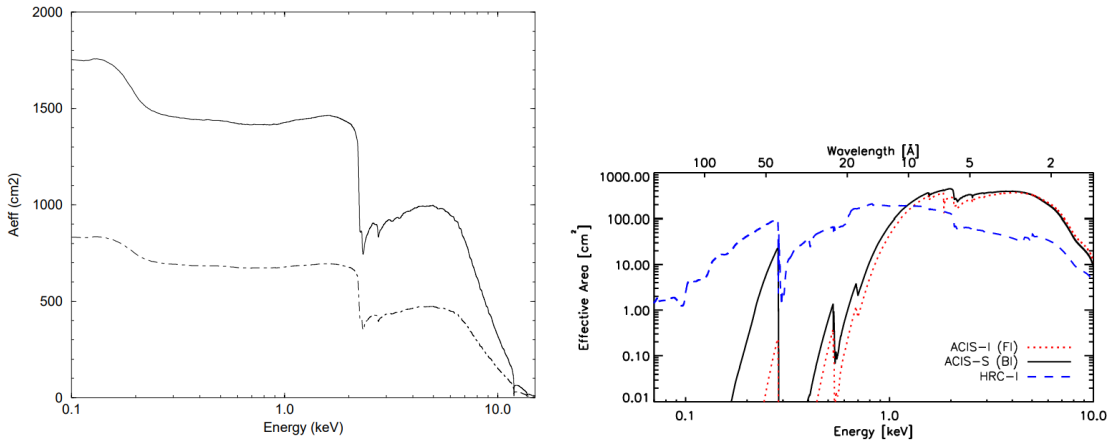

Figure 3.2: *(Left)* From Jansen et al. 2001 - On-axis effective area of the XMM-Newton telescopes without (solid line) and with (dash-dotted line) Reflection Grating Spectrometer (see Section 3.1.1). *(Right)* From `https://cxc.harvard.edu/proposer/POG/html/index.html` - Comparison of the on-axis effective areas for observing a point source (integrated over the PSF) of the HRMA/HRC-I, the HRMA/ACIS(FI), and the HRMA/ACIS(BI) combinations (see Section 3.1.2). The ACIS curves show the predicted values for the middle of Cycle 25.

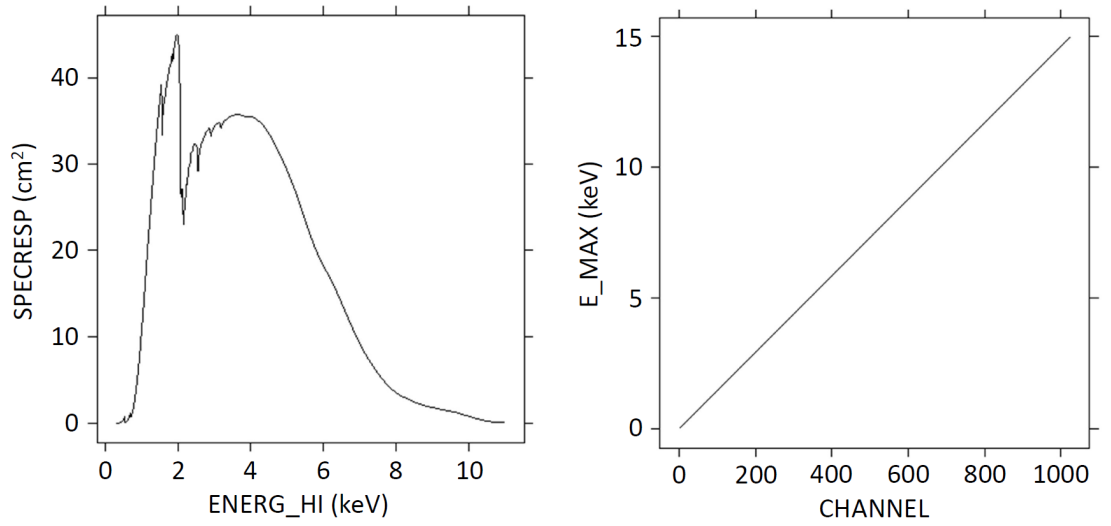

Figure 3.3: Ancillary Response File (ARF) matrix *(left)* and Response Matrix File (RMF, *right*) for J0950+4329 (z = 1.7696).

where S and N are the number of source and background counts, respectively. N derives from the addition in quadrature of sky (N_{sky}) and electronic noise, the latter being due to dark currents ($N_{dark\,current}$) and read out noise ($N_{read\,out}$). Dark current is the result of thermal generation of electrons accumulating on the CCD, which are read by the sensor as photoelectrons; while read out noise is related to the reading elements of the sensor. Sensitivity can be improved through *i)* increasing S or *ii)* diminishing N. *i)* A higher number of source counts can be collected increasing the

effective area, thus the geometric area. This approach brought to the design of XMM-Newton; *ii)* A better angular resolution, consequently a sharper PSF, leads to a reduced background noise. The very high-quality mirrors on board of Chandra allow this result.

XMM (X-ray Multi-Mirror Mission)-Newton *(right panel)* and Chandra *(left panel)* telescopes are shown in Figure 3.4. They were both launched in 1999 by ESA and NASA, respectively. In the following paragraphs, the design and properties of the two satellites are described.

The WISSH project makes use of archival and proprietary data obtained with XMM-Newton and Chandra telescopes over many Cycles of observations.

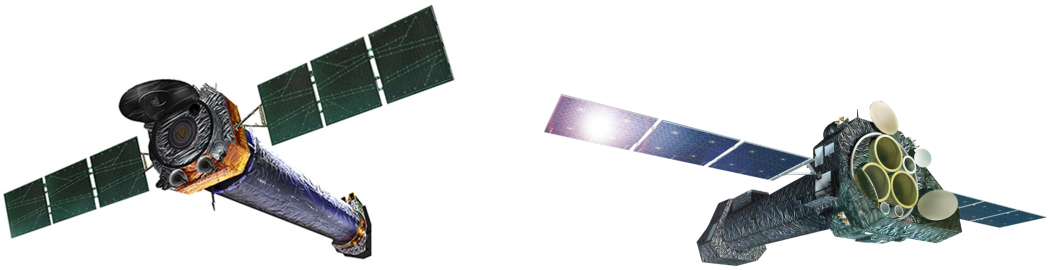

Figure 3.4: Chandra *(left)* and XMM-Newton *(right)* spacecraft (Credits: NASA/CXC/SAO & J.Vaughan, ESA & D. Ducros).

3.1.1 XMM-Newton

The large effective area (up to 1500 cm^{-2} at 2 keV - see *left panel* of Figure 3.2), and the ability to make long uninterrupted exposures make XMM-Newton highly sensitive, with a limiting flux of the order of $\sim 10^{-16}$ $erg\,s^{-1}\,cm^{-2}$. Every observation is carried out by all of the three telescopes on board of the satellite, which work simultaneously. Each telescope is composed by 58 golden-coated Wolter I grazing-incidence mirrors. The three mirror modules are protected by doors during integration, launch and early orbit phase, while baffles suppress (up to a factor of $5-10$) visible and X-ray stray-light, acting as collimators. The platform carrying the mirror assemblies, along with the reflecting surfaces themselves, the Optical Monitor (OM) and the two star-trackers constitute the Mirror Support Platform (MSP).

Each mirror assembly provides a focal length of 7.5 m. The largest shell is 70 cm in diameter and 1.07 *mm* thick; moving towards the focal axis, the surfaces become thinner, down to 0.47 *mm*. Mirror thickness increases with the diameter to guarantee sufficient stiffness.

The OM consists of a 30 cm Ritchey-Chretien telescope with a focal length of ~ 3.8 m. It covers the $170 - 650$ nm wavelength range, looking at the central region (17 arcmin^2) of the X-ray field of view (FoV). Thus, providing optical/UV coverage simultaneously to X-ray observations.

Opposite to the MSP there is the Focal Plane Array (FPA) where all the instruments and respective radiators (which cool the CCD detectors) are located. Two out of three telescopes mount an EPIC MOS (Metal Oxide Semi-conductor) camera at the primary focal plane, while a Reflection Grating Spectrometer (RGS) readout camera is located at the secondary one. When the grating is applied, only $\sim 44\,\%$ of the incident flux reaches the MOS camera, as half of the photons are diverted towards the RGS. An EPIC pn is located on the third telescope. The three EPIC cameras are imaging detectors. All of the instruments are carried by the Focal Plane Platform.

MOS and pn cameras differ under some aspects: geometry of the CCD array (shown in Figure 3.5[1]), instrument design, readout time etc. There are 7 CCDs and 12 pn-CCDs at the focal plane of the MOS and pn camera, respectively. Each CCD and pn-CCD corresponds to 10.9×10.9 arcmin and 13.6×4.4 arcmin at the FoV, respectively. In Figure 3.6[2] are reported the PSFs of the three instruments (MOS1, MOS2 and pn - from left to right), while their size is shown in Table 3.1[3]. It is evident that the pn has a larger PSF with respect to the two MOS; moreover, MOS2 exhibit a more "pronounced" shape. The spikes are caused by the spider-shape support of the mirrors.

Instrument chain	pn		MOS1 + RGS1		MOS2 + RGS2	
	1.5 keV	8 keV	1.5 keV	8 keV	1.5 keV	8 keV
FWHM ["]	6.6	6.6	6.0	5.1	4.5	4.2
HEW ["]	15.1	14.8	13.6	12.5	12.8	12.2

Table 3.1: The on-axis in orbit 1.5 keV PSFs of the different X-ray telescopes.

The three instruments can be used in different operating modes: full frame or partial window mode. In the first case, all pixels of all CCDs are read out and the full field of view (FoV $\approx 30'$ ' is covered. In the second case, for the MOS camera, only the central CCD is operated and 100×100 or 300×300 pixels are read out in small and large window mode, respectively. For the pn camera, in the small window mode, only the CCD containing the focal point is used, while half the area

[1] `https://tinyurl.com/pn-mos`
[2] `https://tinyurl.com/mos-pn-psf`
[3] `https://tinyurl.com/mos-pn-psf`

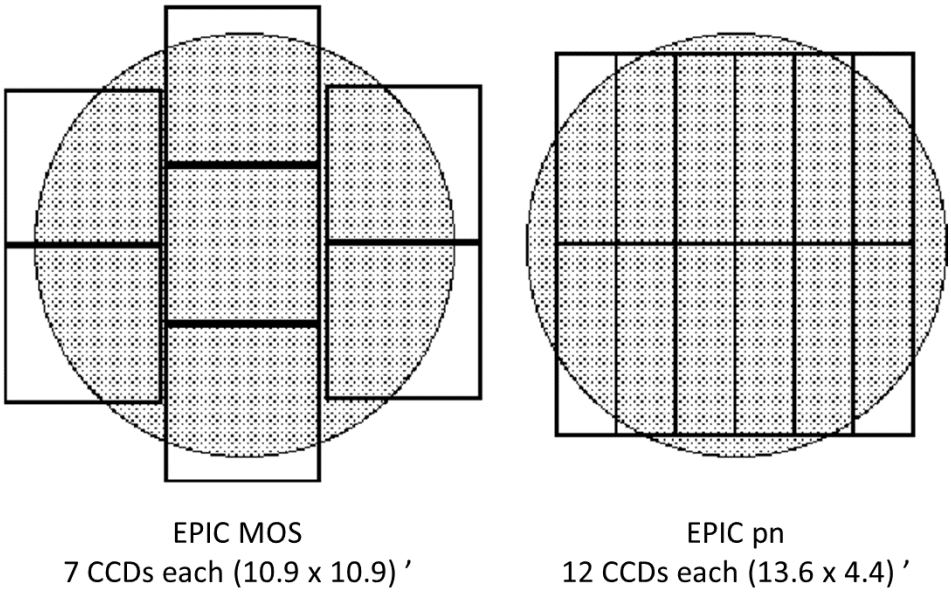

Figure 3.5: A rough sketch of the field of view of the MOS *(left)* and pn *(right)* camera. The shaded circle depicts a 30′ diameter area.

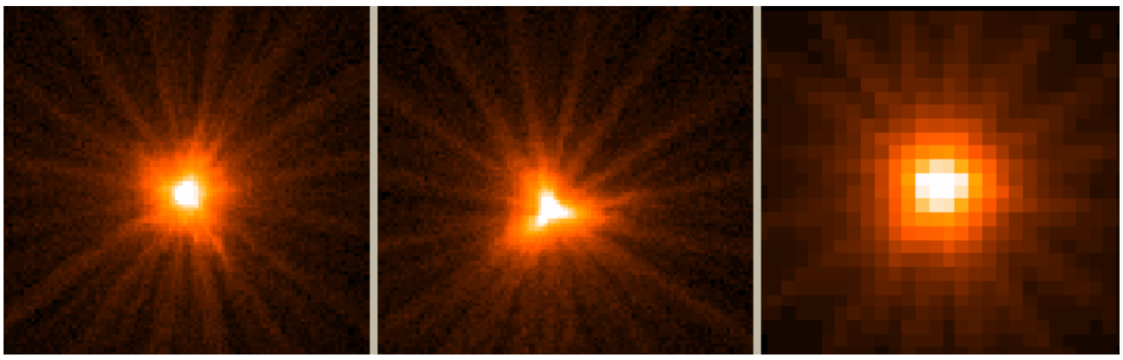

Figure 3.6: On axis Point Spread Function (PSF) of the MOS1, MOS2 and pn X-ray instruments (left to right) registered on the same source with each MOS camera in Small Window mode, and the pn camera in Large Window mode. The pixel size is 1.1 arcsec square for the MOS, and 4.1 arcsec square for the pn. The images are 110 arcsec wide. A square root scale has been used to visualise the wings of the PSF. The core of the PSF is piled-up for this source, with a different factor for the MOS and the pn. The star-like pattern is created by the spider which supports the 58 co-axial Wolter I mirrors of the telescope. The shape of the PSF core is slightly different for all cameras, with MOS2 having a somewhat more “pronounced” shape.

of all 12 CCDs is used in the large window one. All of the cameras produce *event lists* containing, among the others, the position, arrival time and energy of each received photon.

The Service Module (SVM) and the telescope tube connect the MSP to the FPA. The SVM has many different purposes: *i)* thermal control of the whole satellite; *ii)* pointing and slewing, as well as orbit acquisition and maintenance; *iii)*

decoding of ground telecommands and communication with the ground station; *iv)* generation and distribution of regulated power.

XMM-Newton is about 10 m long for 4 tonnes, while the only tube measures 6.8 m. It is made of carbon fibre, which is widely used in the satellite's structure. This material was chosen to guarantee the thermo-elastic stability of the spacecraft, as it is characterised by low thermal-expansion, very high modulus of elasticity and low mass. On the other hand, some components outside the optical path are made of aluminium, due to its thermal conductivity, light-tightness and ease of production properties.

XMM-Newton payload with all the previously mentioned components is represented in Figure 3.7.

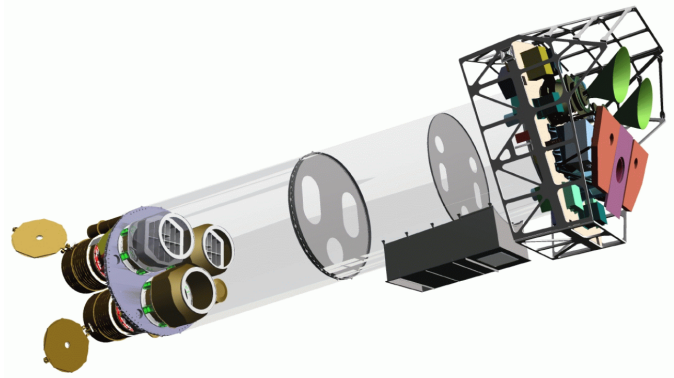

Figure 3.7: If the XMM spacecraft were made of glass, one could gain the above view of its payload. The X-ray telescopes, two with Reflection Grating Arrays, are visible at the lower left. At the right end of the assembly, the focal instruments are shown: the EPIC MOS cameras with their radiators (black/green "horns"), the radiator of the EPIC pn camera (violet) and those of the (light blue) RGS receivers (in orange) (Credits: Dornier Satellitensysteme GmbH).

3.1.2 Chandra

Previously known as Advanced X-ray Astrophysics Facility (AXAF), the telescope was named after the Nobel Prize-winning Indian-American astrophysicist Subrahmanyan Chandrasekhar. With the solar arrays deployed, it is 13.8 m $\times$ 19.5 m in size, resulting in a focal length of 10 m.

X-ray photons collected by the telescope intercept four pairs of nested mirrors (the initial project consisted of six shells), ranging from 0.65 m to 1.23 m in diameter. Their smoothness and alignment accurate to 1.3 μm result in a very sharp PSF. The High Resolution Mirror Assembly (HRMA) is 2.7 m long. The reduced number of mirrors limits Chandra's effective area to ~ 400 cm^2 at 1 keV. A comparison between E_a for different detectors is shown in *right panel* of Figure 3.2,

but the ACIS effective area below 2 keV has continuously declined since launch, due to the build-up of out-gassed material on the ACIS Optical Blocking Filters (OBF) - Figure 3.8[4].

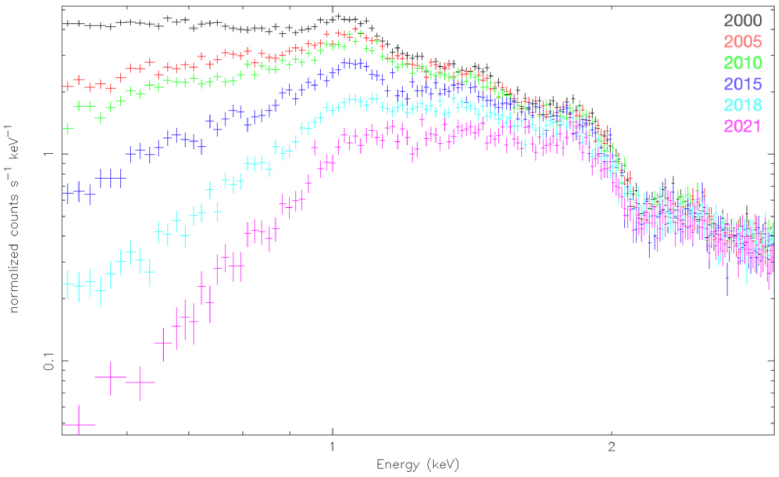

Figure 3.8: ACIS-S spectrum of the galaxy cluster Abell 1795 at six different epochs ranging from 2000 to 2021. The decreasing count rate in the spectrum of a stable calibration source demonstrate the loss of effective area due to the build-up of the contaminant on the ACIS OBF.

Chandra is provided with four science instruments: two imaging and spectroscopy cameras (High Resolution Camera - HRC, Advanced CCD Imaging Spectrometer - ACIS) at the focus, and two high resolution spectrometers (High/Low Energy Transmission Grating Spectrometer - HETG/LETG). HRC comprises two microchannel plates and reaches the highest angular resolution possible with Chandra: < 0.5 arcsec. Moreover, its 31×31 arcmin field of view is the widest available. ACIS is composed by 10 CCD chips forming two arrays (ACIS-I and ACIS-S - Figure 3.9[5]) and has an angular resolution slightly worse than the HRC (~ 0.5 arcsec). There are two types of CCD chips in both the two ACIS arrays: the Front- (FI) and Back-Illuminated (BI) ones. Each CCD corresponds to $\sim 8 \times 8$ arcmin at the FoV. Just over the CCDs are placed Optical Blocking Filters (OBF), which prevent visible-light photons from reaching the chips.

The two cameras work at slightly different energy ranges ($0.06 - 10$ keV and $0.2 - 10$ keV for HRC and ACIS, respectively) but reach the same sensitivity: $\sim 4 \times 10^{-15}$ erg s^{-1} cm^{-2}. HRC and ACIS are mounted on the the Science Instrument Module, along with the mechanisms to move them in and out the focal plane, as only one detector works at a time. The two gold transmission gratings intercept X-ray photons reflected by the mirrors and diffract them, measuring energy to an

[4] https://cxc.harvard.edu/proposer/POG/html/index.html
[5] https://cxc.harvard.edu/proposer/POG/html/index.html

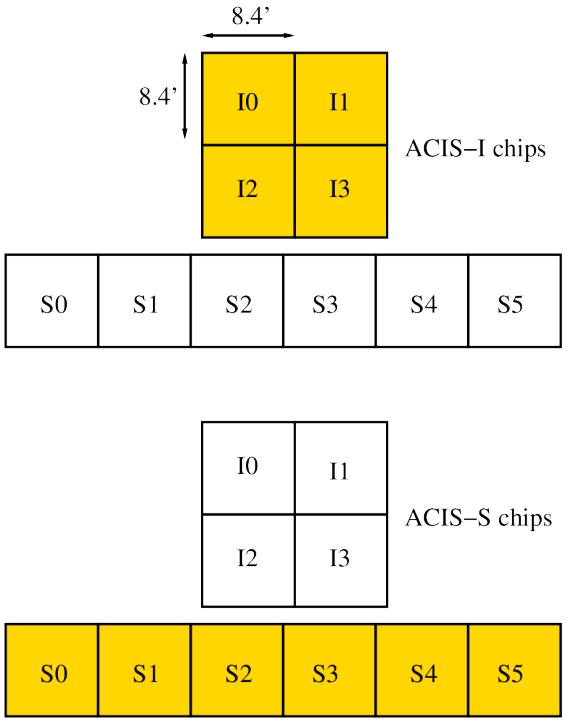

Figure 3.9: A schematic drawing of the ACIS focal plane, not to scale. The ACIS-I array consists of chips I0-I3 (shaded in the *top panel*). The ACIS-S array consists of chips S0-S5 (shaded in the *bottom panel*). The aimpoint falls within I3 and S3 for ACIS-I and ACIS-S, respectively. The view is along the optical axis in each case, from the sky toward the detectors.

accuracy of up to one part in a thousand (LETG).

As for XMM-Newton, ACIS cameras produce *event lists* containing, among the others, the position, arrival time and energy of each received photon. Moreover, both satellites reach a spectral resolution of $\sim$ 150 eV at the iron line energy E $\sim$ 6 keV.

3.2 Data reduction

Once downloaded from the Chandra Data Archive[6] and XMM-Newton Science Archive[7] (XSA), respectively, data are reduced and analysed following the standard science threads of their data analysis software packages. In the following paragraphs, the exact procedure is described.

[6] `https://cda.harvard.edu/chaser/`
[7] `https://www.cosmos.esa.int/web/xmm-newton/xsa`

3.2.1 SAS - XMM-Newton Science Analysis System

Using version 20.0.0 of the XMM-Newton SAS[8], EPIC pn Observation Data Files (ODFs) were reprocessed through the `epproc` task to produce the event files. Possible presence of flaring background, typically attributed to soft protons ($E_p <$ a few 100 keV), was checked extracting the light curve in the $10 - 12$ keV energy range. Accordingly, the event files were filtered with the `espfilt` tool, producing Good Time Interval (GTI) tables, and the light curves were re-extracted. Finally, cleaned event files were created in the energy range $0.3 - 10$ keV. An image was also produced to identify the source and background extraction regions with the visualisation tool `SAOImageDS9`. Circular regions of radii $\sim 10 - 15$" and $\sim 25 - 55$" were used for the source and background, respectively. The former corresponds to $\sim 60 - 70\,\%$ encircled energy fraction (i.e. $60 - 70\,\%$ of the source counts are enclosed in such region, assuming the source to be pointlike). The latter was selected to be free of sources, close enough to the target to be representative of the background in its extraction region and large enough to adequately sample the noise. Net counts derived in the $0.3 - 10$ keV energy range are reported in Table 4.1 with corresponding 1σ uncertainties, while spectral analysis is described in Section 4.2.4.

3.2.2 CIAO - Chandra Interactive Analysis of Observations

The downloaded files were reprocessed through the `chandra_repro` task using CIAO[9] 4.14 package with CALDB 4.9.8. This task automates the recommended data processing steps presented in the CIAO analysis threads. Applying the `dmcopy` tool, the data were filtered and an image in the $0.3 - 7$ keV energy range was produced. As for XMM-Newton observations, the image was inspected with `SAOImageDS9` to define the extraction regions. Circular regions of radii ~ 2" and $\sim 11 - 42$" were selected for the source and background, respectively. Net counts derived in the $0.3-7$ keV energy range are reported in Table 4.1 with corresponding 1σ uncertainties, while spectral analysis is described in Section 4.2.4.

[8] `https://www.cosmos.esa.int/web/xmm-newton/sas`
[9] `https://cxc.cfa.harvard.edu/ciao/`

4

Towards WISSH in X-ray

The current Chapter introduces the X-ray data of WISSH QSOs and their analysis. WISSH X-ray data are described in Section 4.1. Data analysis based on the source counts is reported in Section 4.2.

4.1 Data presentation

All WISSH sources have been observed at least once by Chandra or XMM-Newton. 24/85 quasars have been targeted more than once. Among the remaining 61 objects, four and 57 have only one XMM-Newton and Chandra observation, respectively. Moreover, WISSH sources were the target of the observations (i.e. were at the aimpoint, where the highest capabilities of the optics and detectors are present) in almost all cases. When multiple targeting is available, the data resulting in the higher number of counts are taken into consideration for the subsequent analysis. The complete dataset is presented in Table 4.1, where the (1) ID, (2) SDSS ID, (3) redshift, (4) X-ray observatory, (5) observation ID, (6) observation date, (7) exposure time in kiloseconds (ks), (8) net counts, (9) bolometric luminosity from Saccheo et al. 2023 and (10) BAL nature of the source are reported. BAL identification and classification as Low/High-ionisation refer to Bruni et al. 2019, while "BAL" means that the spectrum coverage did not allow a proper HiBAL/LoBAL classification.

Both archival (Chandra and XMM-Newton) and proprietary (Chandra) data are used. The accepted Chandra proposal (Cycle 23), submitted by Enrico Piconcelli, completes the X-ray sample previously published by M17, consisting of 41 objects. The 44 remaining WISSH QSOs were divided into two redshift ranges - $z < 4$ and $z > 4$ - and 4 and 9 ACIS-S ks were required in the proposal, respectively. The choice was based on previous Chandra observations: all sources with

$z < 4$ had been successfully detected with exposures $t_{exp} \geq 4$ ks. Moreover, > 15 net counts were detected in $\sim 70\,\%$ of the $z < 4$ quasars targeted with exposures $t_{exp} < 4$ ks and it is demonstrated (Vito et al. 2019) that four net counts are enough for deriving sufficiently reliable L_{2-10} and α_{OX} even in more distant and fainter $z > 6$ sources. All of the scheduled observations have been performed, with only $8/85$ ($\sim 9\,\%$) of the sources resulting undetected.

Table 4.1: X-ray WISSH sample and log of the X-ray observations. (1) ID; (2) SDSS ID; (3) redshift; (4) X-ray observatory; (5) observation ID; (6) date of the X-ray observation; (7) net exposure time in ks; (8) net counts in the $0.3-7$ keV and $0.3-10$ keV for Chandra and XMM-Newton, respectively; (9) bolometric luminosity (in units of $\mathrm{Log(L/erg\,s^{-1})}$); (10) BAL classification (Bruni et al. 2019).

ID	SDSS ID	z	X-ray obs.	Obs. ID	Obs. date	Exp (ks)	Net counts	L_{bol}	BAL
(1)	(2)	(3)	(4)	(5)	(6)	(7)	(8)	(9)	(10)
WISSH01	J0045+1438	1.9897	Chandra	6889	2006-07-24	11.4	11.7 ± 3.5	47.53 ± 0.13	LoBAL
WISSH02	J0124+0044	3.822	Chandra	25318	2022-06-04	4.02	9.0 ± 3.0	47.55 ± 0.06	
WISSH03	J0125−1027	3.3588	Chandra	25319	2022-05-22	4.03	10.9 ± 3.3	47.48 ± 0.08	
WISSH04	J0209−0005	2.870	Chandra	17078	2014-11-18	29.69	139.6 ± 11.8	47.67 ± 0.06	
WISSH05	J0216−0921	3.7387	Chandra	25320	2022-07-03	3.89	3.9 ± 2.4	47.53 ± 0.06	HiBAL
WISSH06	J0414+0609	2.6324	Chandra	25321	2022-11-23	4.03	1.92 ± 1.85	47.59 ± 0.07	HiBAL
WISSH07	J0735+2659	1.999	Chandra	17077	2015-10-02	24.76	181.6 ± 12.4	47.66 ± 0.05	
WISSH08	J0745+4734	3.225	Chandra	13308	2012-01-01	1.54	81.0 ± 9.0	47.96 ± 0.15	
WISSH09	J0747+2739	4.126	XMM	0844970601	2020-03-29	47.2	198.2 ± 28.5	47.50 ± 0.06	BAL
WISSH10	J0801+5210	3.257	Chandra	17081	2014-12-11	43.5	166.3 ± 13.1	47.81 ± 0.05	
WISSH11	J0818+0958	3.6943	Chandra	25322	2022-01-27	4.04	3.9 ± 2.4	47.48 ± 0.06	
WISSH12	J0846+2411	4.7218	Chandra	25323	2022-01-02	8.97	< 2.3	47.27 ± 0.09	
WISSH13	J0900+4215	3.294	XMM	0803950601	2017-11-17	10.4	1072.6 ± 33.4	47.89 ± 0.08	
WISSH14	J0904+1309	2.9765	XMM	0745010301	2014-11-24	9.1	502.6 ± 22.8	47.85 ± 0.08	
WISSH15	J0928+5340	4.466	Chandra	25324	2022-12-18	8.94	< 5.2	47.47 ± 0.12	BAL
WISSH16	J0941+3257	3.454	Chandra	25325	2022-01-29	3.91	5.9 ± 2.5	47.61 ± 0.07	

Continues in next page

ID	SDSS ID	z	X-ray obs.	Obs. ID	Obs. date	Exp (ks)	Net counts	L_{bol}	BAL
(1)	(2)	(3)	(4)	(5)	(6)	(7)	(8)	(9)	(10)
WISSH17	J0947+1421	3.031	XMM	0803950801	2017-04-28	21.4	555.7 ± 25.7	47.67 ± 0.05	HiBAL
WISSH18	J0950+4329	1.7696	Chandra	25326	2022-05-22	4.03	292.0 ± 16.9	47.66 ± 0.07	
WISSH19	J0958+2827	3.434	Chandra	20444	2018-09-30	29.68	18.3 ± 4.4	47.59 ± 0.10	
WISSH20	J0959+1312	4.0781	Chandra	25327	2023-01-03	9.26	29.9 ± 5.6	47.81 ± 0.10	BAL
WISSH21	J1013+5615	3.6507	Chandra	25328	2022-12-18	4.03	6.0 ± 2.5	47.61 ± 0.07	HiBAL
WISSH22	J1014+4300	3.1224	XMM	0803950201	2017-04-16	21.6	430.1 ± 21.6	47.81 ± 0.13	
WISSH23	J1015+0020	4.407	Chandra	25329	2022-01-19	9.53	18.9 ± 4.4	47.29 ± 0.07	
WISSH24	J1020+0922	3.6584	Chandra	25330	2022-01-29	4.04	2.9 ± 2.1	47.26 ± 0.08	
WISSH25	J1025+2454	2.3917	Chandra	23755	2021-03-02	9.92	< 2.3	47.29 ± 0.51	LoBAL
WISSH26	J1026+0329	3.8808	Chandra	25331	2023-03-08	4.03	< 2.3	47.38 ± 0.14	
WISSH27	J1027+3543	3.1182	XMM	0803950401	2017-10-28	16.2	705.4 ± 27.5	47.99 ± 0.07	
WISSH28	J1048+4407	4.408	Chandra	25332	2022-09-29	8.82	4.8 ± 2.6	47.74 ± 0.11	BAL
WISSH29	J1051+3107	4.2742	Chandra	25333	2022-02-28	8.96	5.8 ± 2.5	47.53 ± 0.08	BAL
WISSH30	J1057+4555	4.1306	Chandra	878	2000-06-14	2.81	32.9 ± 5.6	47.89 ± 0.08	
WISSH31	J1103+1004	3.6004	Chandra	25334	2023-03-08	4.13	< 2.3	47.51 ± 0.06	HiBAL
WISSH32	J1106−1731	2.572	Chandra	25335	2022-01-23	4.04	4.9 ± 2.6	47.42 ± 0.15	
WISSH33	J1106+6400	2.221	Chandra	6811	2006-07-16	3.65	137.9 ± 11.7	47.71 ± 0.13	
WISSH34	J1110+1930	2.502	Chandra	25336	2023-03-08	3.89	12.9 ± 3.6	47.75 ± 0.40	HiBAL
WISSH35	J1110+4831	2.9741	XMM	0104861001	2002-06-01	24.7	472.5 ± 22.2	47.84 ± 0.06	HiBAL
WISSH36	J1110+4305	3.8492	Chandra	25337	2022-10-11	4.03	71.9 ± 8.4	47.96 ± 0.16	

Continues in next page

ID	SDSS ID	z	X-ray obs.	Obs. ID	Obs. date	Exp (ks)	Net counts	L_{bol}	BAL
(1)	(2)	(3)	(4)	(5)	(6)	(7)	(8)	(9)	(10)
WISSH37	J1111+1336	3.490	Chandra	17082	2015-01-26	43.06	182.5 ± 13.0	47.72 ± 0.05	
WISSH38	J1122+1645	3.0398	Chandra	25338	2022-12-17	4.03	4.9 ± 2.6	47.61 ± 0.13	LoBAL
WISSH39	J1130+0732	2.659	Chandra	25339	2022-12-28	4.03	76.9 ± 8.9	47.70 ± 0.15	HiBAL
WISSH40	J1157+2724	2.217	XMM	0865210601	2020-11-24	10.9	89.7 ± 15.3	47.58 ± 0.07	HiBAL
WISSH41	J1159+1337	4.0084	Chandra	13323	2012-06-29	1.56	3.0 ± 2.1	47.75 ± 0.06	
WISSH42	J1200+3126	2.9947	Chandra	13309	2012-03-18	1.47	18.0 ± 4.2	47.79 ± 0.15	
WISSH43	J1201+0116	3.248	XMM	0803952201	2017-06-06	33.6	96.0 ± 10.3	47.64 ± 0.07	
WISSH44	J1201+1206	3.512	Chandra	13324	2012-06-11	1.56	16.0 ± 4.0	47.75 ± 0.09	
WISSH45	J1204+3309	3.638	Chandra	25340	2023-06-04	4.03	< 2.3	47.76 ± 0.10	LoBAL
WISSH46	J1210+1741	3.831	Chandra	25341	2023-04-03	4.03	< 2.3	47.82 ± 0.15	HiBAL
WISSH47	J1215−0034	2.6987	Chandra	4201	2003-11-14	44.52	132.6 ± 13.3	47.64 ± 0.06	HiBAL
WISSH48	J1219+4940	2.6928	Chandra	25342	2022-12-14	4.03	20.0 ± 4.4	47.62 ± 0.07	
WISSH49	J1220+1126	1.8962	Chandra	25343	2023-03-06	3.85	44.0 ± 6.6	47.81 ± 0.07	
WISSH50	J1236+6554	3.424	Chandra	20443	2018-07-29	44.91	139.2 ± 13.5	47.68 ± 0.06	
WISSH51	J1237+0647	2.7891	Chandra	25344	2023-07-29	4.03	11.9 ± 3.5	47.40 ± 0.08	
WISSH52	J1245+0105	2.8068	Chandra	2974	2002-05-03	6.67	9.9 ± 3.2	47.42 ± 0.16	HiBAL
WISSH53	J1249−0159	3.6286	Chandra	13335	2011-12-03	1.54	3.0 ± 2.1	47.59 ± 0.07	
WISSH54	J1250+2631	2.0476	XMM	0143150201	2003-06-18	13.2	2432.4 ± 50.0	47.86 ± 0.20	
WISSH55	J1250+2046	3.543	Chandra	25345	2022-05-11	3.71	1.90 ± 1.85	47.45 ± 0.12	HiBAL
WISSH56	J1305+0521	4.101	Chandra	25346	2022-06-08	8.96	15.0 ± 3.9	47.53 ± 0.15	HiBAL

Continues in next page

ID	SDSS ID	z	X-ray obs.	Obs. ID	Obs. date	Exp (ks)	Net counts	L_{bol}	BAL
(1)	(2)	(3)	(4)	(5)	(6)	(7)	(8)	(9)	(10)
WISSH57	J1310+4601	2.1423	Chandra	25347	2022-07-03	4.02	48.0 ± 6.9	47.59 ± 0.09	
WISSH58	J1326−0005	3.303	XMM	0804480101	2017-12-30	33.4	324.9 ± 20.1	47.67 ± 0.20	HiBAL
WISSH59	J1328+5818	3.140	XMM	0405690501	2006-11-25	18.1	21.3 ± 5.4	47.37 ± 0.20	HiBAL
WISSH60	J1333+1649	2.099	Chandra	867	2000-04-03	3.01	167.0 ± 12.9	47.68 ± 0.12	
WISSH61	J1421+4633	3.454	Chandra	12859	2011-06-20	23.64	48.6 ± 6.9	47.68 ± 0.05	
WISSH62	J1422+4417	3.648	XMM	0865210401	2021-01-07	23.8	83.1 ± 9.5	47.96 ± 0.09	-HiBAL
- WISSH63	J1426+6025	3.1972	XMM	0402070101	2006-11-12	2.2	65.4 ± 8.2	48.04 ± 0.06	
WISSH64	J1433+0227	4.728	Chandra	25348	2022-05-16	8.96	4.8 ± 2.64	47.57 ± 0.07	
WISSH65	J1441+0454	2.080	Chandra	12860	2012-02-28	21.46	76.5 ± 8.5	47.37 ± 0.10	
WISSH66	J1447+1038	3.7042	Chandra	25349	2022-01-08	4.03	3.9 ± 2.4	47.55 ± 0.08	HiBAL
WISSH67	J1451+1441	3.0940	Chandra	25350	2022-09-05	4.02	4.9 ± 2.6	47.66 ± 0.12	HiBAL
WISSH68	J1506+5220	4.0995	Chandra	25351	2022-08-16	8.96	2.9 ± 2.1	47.66 ± 0.11	HiBAL
WISSH69	J1513+0855	2.8883	Chandra	17079	2016-04-06	29.68	280.4 ± 17.9	47.86 ± 0.09	HiBAL
WISSH70	J1521+5202	2.218	Chandra	15334	2013-10-22	37.39	83.5 ± 7.6	47.85 ± 0.09	
WISSH71	J1538+0855	3.567	Chandra	25352	2022-07-01	4.03	2.9 ± 2.1	47.83 ± 0.07	HiBAL
WISSH72	J1544+4120	3.5513	Chandra	25353	2023-07-05	4.03	2.95 ± 2.14	47.57 ± 0.09	HiBAL
WISSH73	J1549+1245	2.365	XMM	0763160201	2016-02-04	23.8	352.1 ± 21.4	47.74 ± 0.13	HiBAL
WISSH74	J1554+1109	2.930	Chandra	25354	2023-07-18	4.00	< 2.3	47.80 ± 0.26	
WISSH75	J1555+1003	3.529	Chandra	25355	2022-06-30	4.03	1.90 ± 1.85	47.41 ± 0.14	LoBAL
WISSH76	J1559+4828	3.419	Chandra	25356	2023-03-06	3.85	2.94 ± 2.14	47.50 ± 0.05	

Continues in next page

ID	SDSS ID	z	X-ray obs.	Obs. ID	Obs. date	Exp (ks)	Net counts	L_{bol}	BAL
(1)	(2)	(3)	(4)	(5)	(6)	(7)	(8)	(9)	(10)
WISSH77	J1559+1923	3.9532	Chandra	25357	2022-10-10	4.03	1.89 ± 1.85	47.64 ± 0.09	
WISSH78	J1621−0042	3.7285	Chandra	2184	2001-09-05	1.57	26.0 ± 5.2	47.78 ± 0.09	
WISSH79	J1633+3629	3.5747	Chandra	25358	2023-07-21	4.03	6.9 ± 2.7	47.80 ± 0.08	
WISSH80	J1639+2824	3.846	Chandra	13315	2011-11-24	1.54	6.0 ± 2.5	48.07 ± 0.07	HiBAL
WISSH81	J1650+2507	3.337	Chandra	25359	2022-07-22	4.03	2.9 ± 2.1	47.62 ± 0.14	HiBAL
WISSH82	J1701+6412	2.753	XMM	0723700301	2013-08-04	30.5	2337.9 ± 48.8	47.96 ± 0.13	
WISSH83	J2123−0050	2.282	Chandra	17080	2015-12-22	39.55	745.3 ± 27.8	47.69 ± 0.06	HiBAL
WISSH84	J2238−0808	3.1422	Chandra	25360	2022-09-19	4.03	2.9 ± 2.1	47.47 ± 0.06	HiBAL
WISSH85	J2346−0016	3.511	Chandra	25361	2022-05-07	4.03	4.9 ± 2.6	47.53 ± 0.05	

4.2 Data analysis

X-ray observations result in a number of net counts ranging from 0 to $\sim$ 2340 (see Table 4.1). Once source detection is carried out, depending on the number of available photons, sources are divided into four groups and a different approach is used for each of them. For all of the WISSH quasars, the hard (i.e. $2 - 10$ keV) X-ray intrinsic luminosity (L_{2-10}) and observed $0.5 - 10$ keV flux ($F_{0.5-10}$) are derived. Moreover, intrinsic column density is measured for objects with ≥ 6 counts, through HR (Equation 2.4) or spectral analysis. From the latter procedure, the X-ray spectral index Γ is also derived for sources with ≥ 20 counts.

Non-detections For objects with virtually zero counts in an extraction aperture of 2" centered on the optical source position, upper limits are computed on L_{2-10} and $F_{0.5-10}$ at the 90 % confidence level (Section 4.2.1);

$1 - 5$ counts Source detection is derived through the binomial method (Section 4.2.2);

$6 - 19$ counts Hardness Ratio is derived computing separately soft and hard X-ray photons (Section 4.2.3);

≥ 20 counts Spectral extraction and analysis allow the derivation of basic X-ray spectral parameters (Section 4.2.4).

In the following paragraphs the different approaches are extensively explained.

4.2.1 X-ray non-detections

7/85 WISSH observations - all of which performed with Chandra - result in 0 counts. Previous observations at shorter wavelengths (at least from the SDSS, in which data for all WISSH sources are available, by construction) confirmed the presence of an AGN at the quasars position. Thus, the X-ray exposure is not deep enough to detect these objects.

Working in a Poissonian regime, the upper limits are computed by deriving the probability distribution function of net counts using the binomial method of Weisskopf et al. 2007 (see their Appendix A3). The nominal value of the net counts coincides to the peak of the probability distribution. In Table 4.1, upper limits corresponding to the 90 % confidence interval are reported.

The X-ray flux upper limits are derived considering the value at 90 % confidence level as the detected net counts. Assuming a standard X-ray spectral index ($\Gamma = 1.8$ - e.g. Lawson et al. 1997, Reeves et al. 2000), a proper Galactic absorption ($N_{H,gal}$)

and a possible intrinsic absorption (here considered to be negligible), Chandra WebPIMMS allows to derive observed fluxes. Moreover, the decreasing quality of the ACIS detector, caused by piled-up dust over time (see Figure 3.8) is taken into account through the specification of the Chandra Cycle.

Hard X-ray intrinsic luminosities can be derived from fluxes as follows:

$$L_{2-10} = 4\pi d_L^2 \, F_{2-10} \, (1+z)^{\Gamma-2} \ \mathrm{erg\,s^{-1}} \tag{4.1}$$

where d_L is the luminosity distance[1], F_{2-10} is the unabsorbed flux in the $2-10$ keV energy range, z is the source redshift and $\Gamma = 1.8$. F_{2-10} is derived through WebPIMMS.

Results for the seven undetected sources are summarised in Table 4.2.

ID (1)	SDSS ID (2)	z (3)	$N_{H,gal}$ (4)	$\mathrm{Log}(L_{2-10})$ (5)	$\mathrm{Log}(F_{0.5-10})$ (6)	obsCycle (7)
WISSH12	J0846+2411	4.7218	3.05	< 44.77	< -14.30	23
WISSH25	J1025+2454	2.3917	1.16	< 43.82	< -14.52	22
WISSH26	J1026+0329	3.8808	3.25	< 44.87	< -13.99	23
WISSH31	J1103+1004	3.6004	2.33	< 44.79	< -13.99	23
WISSH45	J1204+3309	3.638	1.42	< 44.80	< -13.99	23
WISSH46	J1210+1741	3.831	3.35	< 44.85	< -13.99	23
WISSH74	J1554+1109	2.930	3.46	< 44.57	< -13.99	23

Table 4.2: Undetected WISSH sources. (1) ID; (2) SDSS ID; (3) redshift; (4) Galactic absorption (in units of 10^{20} $\mathrm{cm^{-2}}$); (5) intrinsic $2-10$ keV luminosity (in units of $\mathrm{Log(L/erg\,s^{-1})}$); (6) observed $0.5-10$ keV flux (in units of $\mathrm{Log(F/erg\,s^{-1}\,cm^{-2})}$); (7) Chandra observation Cycle. Upper limits are reported at 90 % confidence level.

4.2.2 Sources with $1-5$ counts

All of the observations where sources have $1 \leq$ counts ≤ 5 counts in an extraction aperture of 2 " were carried out by Chandra. The procedure followed for these 23/85 objects is similar to that described in Section 4.2.1 for non-detections. The robustness of the detections was tested with the aforementioned binomial method: for all but one source (J0928+5340, z = 4.466), a detection significance > 99 % was obtained. Indeed, thanks to the sharp Chandra PSF, resulting in an extremely low background level, even very few counts can constitute a detection. J0928+5340 was

[1]Calculated from `https://astro.ucla.edu/~wright/CosmoCalc.html` assuming $H_0 = 70$, $\Omega_m = 0.27$ and $\Omega_\Lambda = 0.73$ (Bennett et al. 2013).

treated as an undetected object (Section 4.2.1), while quasars net counts and corresponding 1σ uncertainties were derived for the other sources using the binomial method.

Under the same assumptions as in Section 4.2.1 (i.e. $\Gamma = 1.8$ and negligible intrinsic absorption), observed $0.5-10$ keV fluxes were derived through WebPIMMS. Than, intrinsic $2-10$ keV luminosities were obtained from Equation 4.1.

Results for the 23 sources with a number of counts in the range $\sim 1-5$ are summarised in Table 4.3.

ID (1)	SDSS ID (2)	z (3)	$N_{H,gal}$ (4)	$Log(L_{2-10})$ (5)	$Log(F_{0.5-10})$ (6)	obsCycle (7)
WISSH05	J0216−0921	3.7387	2.91	45.05 ± 0.20	-13.77 ± 0.20	23
WISSH06	J0414+0609	2.6324	10.2	44.40 ± 0.30	-14.08 ± 0.30	23
WISSH11	J0818+0958	3.6943	2.79	45.04 ± 0.20	-13.77 ± 0.20	23
WISSH15	J0928+5340	4.466	1.66	< 45.01	< -13.99	23
WISSH24	J1020+0922	3.6584	2.89	44.87 ± 0.23	-13.93 ± 0.23	23
WISSH28	J1048+4407	4.408	1.16	44.91 ± 0.20	-14.07 ± 0.20	23
WISSH32	J1106−1731	2.572	4.27	44.74 ± 0.18	-13.69 ± 0.18	23
WISSH38	J1122+1645	3.0398	1.47	44.91 ± 0.20	-13.69 ± 0.20	23
WISSH41	J1159+1337	4.0084	2.07	45.05 ± 0.24	-13.84 ± 0.24	13
WISSH53	J1249−0159	3.6286	1.66	44.94 ± 0.24	-13.84 ± 0.24	13
WISSH55	J1250+2046	3.543	2.08	44.69 ± 0.30	-14.07 ± 0.30	23
WISSH64	J1433+0227	4.728	2.58	44.99 ± 0.20	-14.07 ± 0.20	23
WISSH66	J1447+1038	3.7042	1.56	45.04 ± 0.20	-13.77 ± 0.20	23
WISSH67	J1451+1441	3.0940	1.52	44.93 ± 0.20	-13.69 ± 0.20	23
WISSH68	J1506+5220	4.0995	1.84	44.62 ± 0.22	-14.29 ± 0.22	23
WISSH71	J1538+0855	3.567	3.09	44.85 ± 0.23	-13.93 ± 0.23	23
WISSH72	J1544+4120	3.5513	1.86	44.84 ± 0.23	-13.93 ± 0.23	23
WISSH75	J1555+1003	3.529	3.90	44.69 ± 0.30	-14.07 ± 0.30	23
WISSH76	J1559+4828	3.419	1.69	44.86 ± 0.24	-13.87 ± 0.24	23
WISSH77	J1559+1923	3.9532	2.72	44.81 ± 0.30	-14.07 ± 0.30	23
WISSH81	J1650+2507	3.337	4.63	44.78 ± 0.23	-13.93 ± 0.23	23
WISSH84	J2238−0808	3.1422	3.56	44.71 ± 0.23	-13.93 ± 0.23	23
WISSH85	J2346−0016	3.511	3.71	45.07 ± 0.20	-13.69 ± 0.20	23

Table 4.3: WISSH sources with $1 \leq$ counts ≤ 5. (1) ID; (2) SDSS ID; (3) redshift; (4) Galactic absorption (in units of 10^{20} cm^{-2}); (5) intrinsic $2-10$ keV luminosity (in units of $\mathrm{Log(L/erg\,s^{-1})}$); (6) observed $0.5-10$ keV flux (in units of $\mathrm{Log(F/erg\,s^{-1}\,cm^{-2})}$); (7) Chandra observation Cycle. Errors and upper limits are reported at 1σ and 90 % confidence level, respectively.

4.2.3 Sources with 6 − 19 counts

The 16/85 WISSH QSOs with a number of net counts between ~ 6 and ~ 19 have all been observed with Chandra. Images of the soft $0.3-2$ keV and hard $2-7$ keV emission are separately produced as in Section 3.2.2. Thus, the number of soft and hard X-ray source and background photons is derived from `SAOImageDS9`.

The number of soft and hard X-ray photons, together with the source and background extraction areas, are required to derive the Hardness Ratio through the Bayesian Estimator of Hardness Ratio (BEHR) program (Park et al. 2006). BEHR is especially useful in Poissonian regimes, where background subtraction is not a good solution, as correctly deals with the non-Gaussian nature of the error propagation regardless of whether the source is detected in both passbands or not. HR values and corresponding 1σ uncertainties are reported in Table 4.4.

HR is representative of the source spectrum, thus, it is strictly linked to the intrinsic absorption (N_H), which shapes the spectral profile. Accordingly, comparing HR values with simulated absorbed power-law models (fixed Γ) at a given redshift, intrinsic N_H values are constrained. The relation among HR and z for Chandra Cycle 23, considering various N_H, is represented in Figure 4.1. Moreover, the corresponding uncertainties are derived converting the maximum and minimum HR values. Intrinsic obscuration is considered to be significant when its lower boundary is not consistent with zero; otherwise, if the highest end of the N_H range is not consistent with zero, upper limits are obtained. As evident in Table 4.4, 4/16 (25 %) sources exhibit a significant N_H.

Broad-band observed flux is calculated through WebPIMMS as in Section 4.2.1 and 4.2.2. Spectral index is fixed to be 1.8 and a proper $N_{H,gal}$ is used, as before; the previously estimated significant intrinsic column densities are also included. Using the same parameters, L_{2-10} is derived from Equation 4.1.

Results for the 16 sources with $6 \leq$ counts ≤ 19 are summarised in Table 4.4.

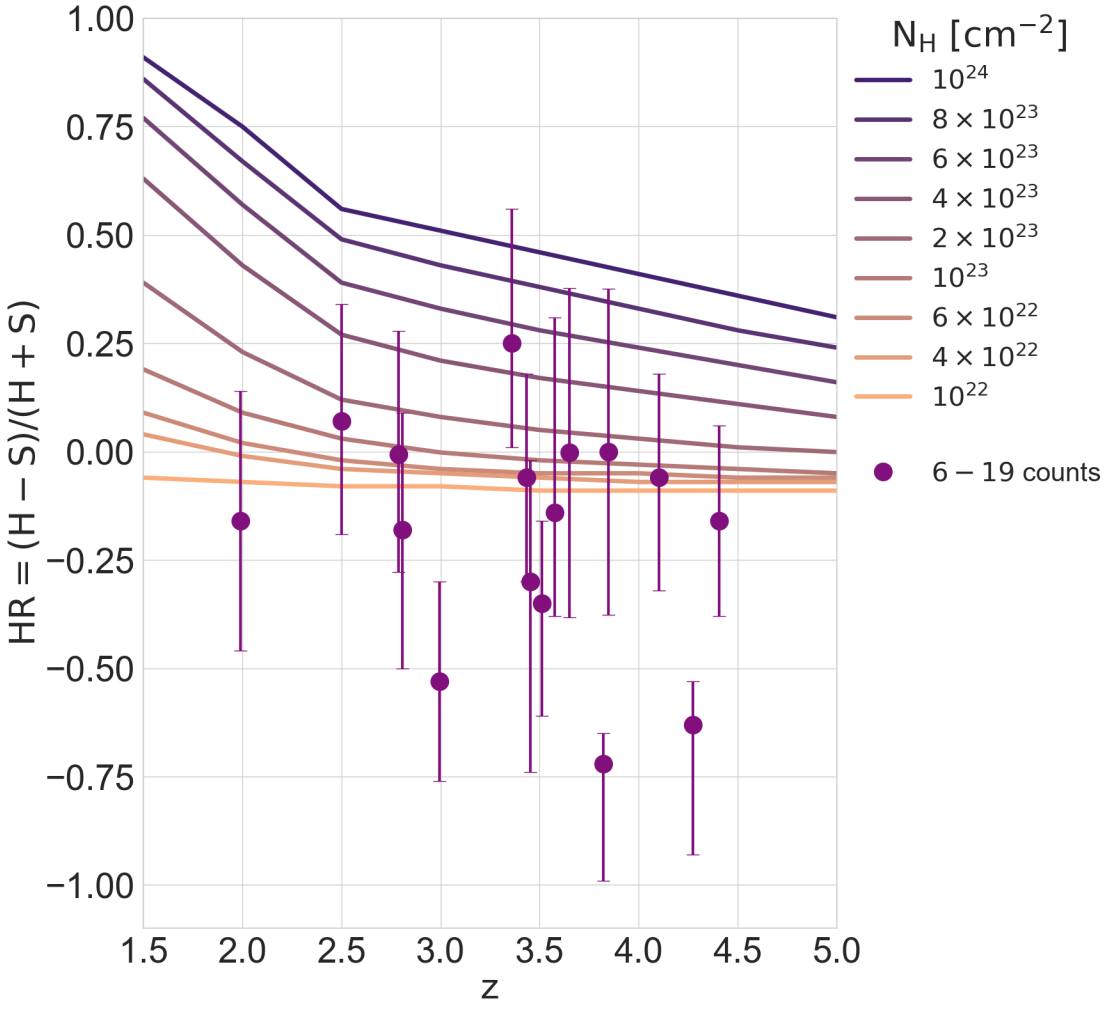

Figure 4.1: Hardness Ratio (HR) as a function of redshift for WISSH sources with $6-19$ counts. Color-coded curves represent HR variation with z for a given intrinsic absorption and fixed X-ray spectral index ($\Gamma = 1.8$) for Chandra Cycle 23. Errors are reported at 1σ confidence level.

Table 4.4: WISSH sources with $6 \leq$ counts ≤ 19. (1) ID; (2) SDSS ID; (3) redshift; (4) Galactic absorption (in units of 10^{20} cm^{-2}); (5) Hardness Ratio; (6) intrinsic column density (in units of 10^{22} cm^{-2}); (7) intrinsic $2-10$ keV luminosity (in units of Log(L/erg s^{-1})); (8) observed $0.5-10$ keV flux (in units of Log(F/erg s^{-1} cm^{-2})); (9) Chandra observation Cycle. Errors and upper limits are reported at 1σ confidence level.

ID	SDSS ID	z	$N_{H,gal}$	HR	N_H	$Log(L_{2-10})$	$Log(F_{0.5-10})$	obsCycle
(1)	(2)	(3)	(4)	(5)	(6)	(7)	(8)	(9)
WISSH01	J0045+1438	1.9897	5.50	-0.16 ± 0.30	15^{+15}_{-13}	44.39 ± 0.11	-13.91 ± 0.11	07
WISSH02	J0124+0044	3.822	3.13	$-0.72^{+0.07}_{-0.27}$	< 0.04	45.42 ± 0.12	-13.43 ± 0.12	23
WISSH03	J0125-1027	3.3588	3.20	$0.25^{+0.31}_{-0.24}$	50^{+50}_{-35}	45.58 ± 0.11	-13.30 ± 0.11	23
WISSH16	J0941+3257	3.454	1.44	$-0.30^{+0.28}_{-0.44}$	< 10	45.14 ± 0.15	-13.59 ± 0.15	23
WISSH19	J0958+2827	3.434	1.46	-0.06 ± 0.24	< 60	44.63 ± 0.07	-14.10 ± 0.07	19
WISSH21	J1013+5615	3.6507	0.91	-0.002 ± 0.380	< 80	45.20 ± 0.15	-13.59 ± 0.15	23
WISSH23	J1015+0020	4.407	2.90	$-0.16^{+0.10}_{-0.22}$	< 30	45.52 ± 0.10	-13.47 ± 0.10	23
WISSH29	J1051+3107	4.2742	2.12	$-0.63^{+0.10}_{-0.30}$	< 0.04	44.96 ± 0.18	-13.99 ± 0.18	23
WISSH34	J1110+1930	2.502	1.73	$0.07^{+0.27}_{-0.26}$	< 50	45.14 ± 0.10	-13.25 ± 0.10	23

Continues in next page

ID	SDSS ID	z	$N_{H,gal}$	HR	N_H	$Log(L_{2-10})$	$Log(F_{0.5-10})$	obsCycle
(1)	(2)	(3)	(4)	(5)	(6)	(7)	(8)	(9)
WISSH42	J1200+3126	2.9947	1.49	-0.53 ± 0.23	< 15	45.55 ± 0.09	-13.04 ± 0.09	13
WISSH44	J1201+1206	3.512	1.89	$-0.35^{+0.19}_{-0.26}$	< 40	45.65 ± 0.10	-13.11 ± 0.10	13
WISSH51	J1237+0647	2.7891	1.53	-0.01 ± 0.28	< 50	45.22 ± 0.11	-13.29 ± 0.11	23
WISSH52	J1245+0105	2.8068	1.42	$-0.18^{+0.27}_{-0.32}$	30^{+30}_{-23}	44.92 ± 0.12	-13.75 ± 0.12	03
WISSH56	J1305+0521	4.101	1.88	$-0.06^{+0.24}_{-0.26}$	< 50	45.37 ± 0.09	-13.54 ± 0.09	23
WISSH79	J1633+3629	3.5747	1.14	$-0.14^{+0.31}_{-0.38}$	< 40	45.23 ± 0.15	-13.54 ± 0.15	23
WISSH80	J1639+2824	3.846	2.93	$-0.001^{+0.377}_{-0.375}$	70^{+80}_{-55}	45.76 ± 0.15	-13.28 ± 0.15	13

4.2.4 Sources with ≥ 20 counts

The remaining 39/85 observations, corresponding to ≥ 20 counts sources, are deep enough to perform basic spectral analysis. Thus, not only $F_{0.5-10}$ and L_{2-10}, but also the N_H and X-ray spectral index (Γ) are estimated through the X-ray spectral fitting package `Xspec`[2]. Sources have either XMM-Newton (16/39 objects) or Chandra (23/39 objects) data; accordingly, spectral extraction is performed with the appropriate software.

XMM-Newton sources Following the procedure described in Section 3.2.1, spectra are extracted through the XMM-Newton SAS meta-task `especget`, which runs also the `arfgen`, `rmfgen` and `backscale` tasks. Thus, ARF and RMF matrix are calculated, and the source and background extraction region are re-scaled to obtain the spectra;

Chandra sources Once the source and background regions are identified as in Section 3.2.2, spectral extraction is performed with CIAO task `specextract`.

Spectral points are grouped to one count/bin due to low statistic regime (~ 20 to ~ 2340 counts), and C-statistic is used. A simple power-law model with proper Galactic absorption is initially applied, which translates into an `Xspec` model of the form `pha*po`. The presence of an absorbing component at the source redshift is also tested adding a `zpha` multiplicative component. To verify its significance, an F-test is performed fixing the threshold for a relevant improvement of the model at 95 %. 11/39 (~ 28 %) sources exhibit a non-negligible N_H, which is not expected, given the Type 1 nature of WISSH QSOs. However, ~ 24 % (Bruni et al. 2019) of WISSH sources exhibits BAL spectral features, witnessing the presence of outflows; in this context, obscuring gas is commonly found (e.g. Brandt et al. 2000) and thought to prevent over-ionisation, thus allowing wind launching. Two re-binned spectra are visible in Figure 4.2, for which ~ 292 *(top panel)* and ~ 20 *(bottom panel)* counts are detected. They are both fitted through a simple power-law model + Galactic absorption.

Most of the spectral indices are close to the expected range $\sim 1.8 - 2$ within 1σ errors. However, there are some exceptions: the most noticeable is J1328+5818 (z = 3.140), which exhibits $\Gamma = 0.60 \pm 0.33$. This result may be due to the low number of counts, which is very close to the limit value for spectral analysis and could prevent the identification of an absorbing component. Fixing $\Gamma = 1.8$ to derive the intrinsic column density, it results in the presence of a thick obscuring component ($N_H = 2.4^{+1.4}_{-1.0} \times 10^{23}$ cm^{-2}).

[2] `https://heasarc.gsfc.nasa.gov/xanadu/xspec/`

Table 4.5 shows the results for the ≥ 20 counts sources.

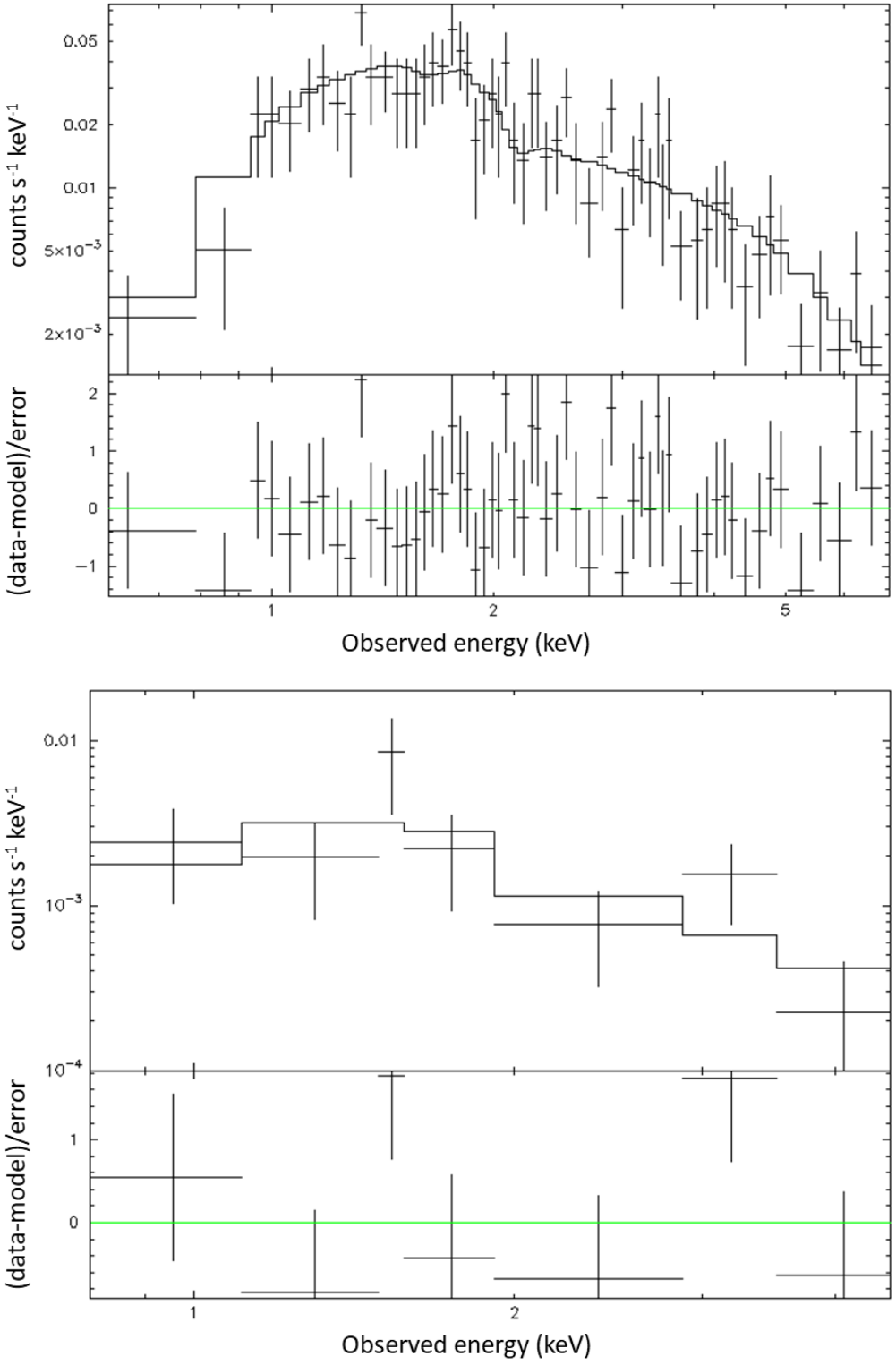

Figure 4.2: Two re-binned spectra of J0950+4329 (*top*, z = 1.7696) and J1219+4940 (*bottom*, z = 2.6928), observed with Chandra. About 292 and 20 counts are detected for these sources, respectively. Both spectra are fitted with a simple power-law model with Galactic absorption. The residuals are defined as `(data − model)` in units of σ.

Table 4.5: WISSH sources with ≥ 20 counts. (1) ID; (2) SDSS ID; (3) redshift; (4) Galactic absorption (in units of 10^{20} cm^{-2}); (5) X-ray spectral index; (6) intrinsic column density (in units of 10^{22} cm^{-2}); (7) intrinsic $2-10$ keV luminosity (in units of Log(L/erg s^{-1})); (8) observed $0.5-10$ keV flux (in units of Log(F/erg s^{-1} cm^{-2})); (9) Chandra observation Cycle. f: frozen value. Errors and upper limits are reported at 1σ confidence level.

ID	SDSS ID	z	$N_{H,gal}$	Γ	N_H	$Log(L_{2-10})$	$Log(F_{0.5-10})$	obsCycle
(1)	(2)	(3)	(4)	(5)	(6)	(7)	(8)	(9)
WISSH04	J0209−0005	2.870	2.29	1.36 ± 0.14	< 1.04	45.20 ± 0.04	-13.17 ± 0.06	16
WISSH07	J0735+2659	1.999	5.39	1.57 ± 0.13	< 1.77	45.13 ± 0.03	-12.99 ± 0.05	16
WISSH08	J0745+4734	3.225	5.78	$1.83^{+0.20}_{-0.19}$	< 1.97	46.38 ± 0.05	-12.28 ± 0.07	13
WISSH09	J0747+2739	4.126	3.82	1.65 ± 0.13	< 3.18	45.09 ± 0.04	-13.73 ± 0.06	-
WISSH10	J0801+5210	3.257	4.61	1.74 ± 0.14	< 0.35	45.31 ± 0.04	-13.33 ± 0.05	15
WISSH13	J0900+4215	3.294	2.37	$1.89^{+0.05}_{-0.04}$	< 0.52	46.24 ± 0.01	-12.46 ± 0.02	-
WISSH14	J0904+1309	2.9765	2.58	2.04 ± 0.07	< 0.89	45.88 ± 0.02	-12.77 ± 0.03	-
WISSH17	J0947+1421	3.031	2.95	1.98 ± 0.11	$0.90^{+0.44}_{-0.42}$	45.59 ± 0.02	-13.03 ± 0.03	-
WISSH18	J0950+4329	1.7696	0.94	1.55 ± 0.12	< 4.29	46.16 ± 0.03	-11.84 ± 0.03	23

Continues in next page

ID	SDSS ID	z	$N_{H,gal}$	Γ	N_H	$Log(L_{2-10})$	$Log(F_{0.5-10})$	obsCycle
(1)	(2)	(3)	(4)	(5)	(6)	(7)	(8)	(9)
WISSH20	J0959+1312	4.0781	2.62	$2.56^{+0.49}_{-0.46}$	< 76.72	46.00 ± 0.20	-13.16 ± 0.10	23
WISSH22	J1014+4300	3.1224	1.61	2.15 ± 0.08	< 0.96	45.47 ± 0.02	-13.26 ± 0.04	-
WISSH27	J1027+3543	3.1182	0.81	1.99 ± 0.06	< 0.57	45.79 ± 0.02	-12.89 ± 0.03	-
WISSH30	J1057+4555	4.1306	0.87	2.08 ± 0.31	< 0.48	45.75 ± 0.08	-13.25 ± 0.14	-
WISSH33	J1106+6400	2.221	0.92	2.09 ± 0.15	< 0.23	45.73 ± 0.04	-12.61 ± 0.05	07
WISSH35	J1110+4831	2.9741	1.62	1.92 ± 0.07	< 0.15	45.41 ± 0.02	-13.20 ± 0.03	-
WISSH36	J1110+4305	3.8492	1.39	1.76 ± 0.26	< 12.21	46.36 ± 0.10	-12.45 ± 0.06	23
WISSH37	J1111+1336	3.490	1.54	1.76 ± 0.13	< 4.84	45.39 ± 0.04	-13.32 ± 0.05	16
WISSH39	J1130+0732	2.659	4.86	1.56 ± 0.23	< 26.63	45.98 ± 0.07	-12.40 ± 0.06	23
WISSH40	J1157+2724	2.217	1.78	$1.61^{+0.25}_{-0.22}$	< 0.51	44.89 ± 0.08	-13.33 ± 0.23	-
WISSH43	J1201+0116	3.248	1.63	$2.11^{+0.37}_{-0.31}$	$4.39^{+3.40}_{-2.34}$	44.80 ± 0.05	-13.88 ± 0.08	-
WISSH47	J1215−0034	2.6987	1.69	$1.53^{+0.31}_{-0.29}$	$18.18^{+7.74}_{-6.49}$	45.30 ± 0.15	-13.21 ± 0.07	04

Continues in next page

ID	SDSS ID	z	$N_{H,gal}$	Γ	N_H	$Log(L_{2-10})$	$Log(F_{0.5-10})$	obsCycle
(1)	(2)	(3)	(4)	(5)	(6)	(7)	(8)	(9)
WISSH48	J1219+4940	2.6928	2.09	$2.02^{+0.55}_{-0.54}$	< 10.60	45.52 ± 0.14	-13.01 ± 0.11	23
WISSH49	J1220+1126	1.8962	2.20	$2.21^{+0.37}_{-0.36}$	< 18.10	45.55 ± 0.08	-12.64 ± 0.07	23
WISSH50	J1236+6554	3.424	2.31	2.45 ± 0.17	< 4.35	45.51 ± 0.05	-13.40 ± 0.04	19
WISSH54	J1250+2631	2.0476	0.94	2.12 ± 0.03	-	45.97 ± 0.01	-12.28 ± 0.01	-
WISSH57	J1310+4601	2.1423	1.17	2.80 ± 0.32	< 5.34	45.71 ± 0.08	-12.66 ± 0.07	23
WISSH58	J1326−0005	3.303	1.69	$1.79^{+0.14}_{-0.13}$	$3.64^{+1.10}_{-0.98}$	45.34 ± 0.03	-13.25 ± 0.04	-
WISSH59	J1328+5818	3.140	1.94	1.8^{f}	$23.91^{+14.49}_{-10.00}$	44.80 ± 0.11	-13.54 ± 0.13	-
WISSH60	J1333+1649	2.099	1.60	$1.38^{+0.12}_{-0.11}$	< 0.62	45.84 ± 0.04	-12.27 ± 0.06	01
WISSH61	J1421+4633	3.454	1.10	$1.23^{+0.27}_{-0.26}$	< 8.81	44.95 ± 0.08	-13.51 ± 0.11	12
WISSH62	J1422+4417	3.648	0.81	$1.99^{+0.51}_{-0.39}$	$13.05^{+12.67}_{-6.96}$	44.96 ± 0.06	-13.68 ± 0.08	-
WISSH63	J1426+6025	3.1972	2.08	$1.63^{+0.19}_{-0.18}$	< 2.58	45.69 ± 0.06	-12.89 ± 0.09	-
WISSH65	J1441+0454	2.080	2.81	$1.83^{+0.40}_{-0.39}$	$5.42^{+3.43}_{-3.10}$	44.78 ± 0.05	-13.38 ± 0.08	12

Continues in next page

ID	SDSS ID	z	$N_{H,gal}$	Γ	N_H	$Log(L_{2-10})$	$Log(F_{0.5-10})$	obsCycle
(1)	(2)	(3)	(4)	(5)	(6)	(7)	(8)	(9)
WISSH69	J1513+0855	2.8883	2.19	$2.01^{+0.18}_{-0.17}$	$5.26^{+2.11}_{-1.86}$	45.74 ± 0.07	-12.96 ± 0.04	16
WISSH70	J1521+5202	2.218	1.53	$1.58^{+0.38}_{-0.37}$	$11.37^{+5.17}_{-4.44}$	44.91 ± 0.06	-13.43 ± 0.08	14
WISSH73	J1549+1245	2.365	3.18	$2.25^{+0.18}_{-0.17}$	$4.66^{+1.13}_{-0.94}$	45.13 ± 0.02	-13.09 ± 0.04	-
WISSH78	J1621−0042	3.7285	6.49	$1.81^{+0.38}_{-0.37}$	< 4.26	45.98 ± 0.11	-12.81 ± 0.13	02
WISSH82	J1701+6412	2.753	2.11	$2.20^{+0.06}_{-0.05}$	0.76 ± 0.16	45.95 ± 0.01	-12.64 ± 0.01	-
WISSH83	J2123−0050	2.282	3.65	1.97 ± 0.07	< 0.38	45.69 ± 0.02	-12.66 ± 0.02	16

To summarise, among WISSH sources

- 8 are undetected;
- 22 have 1 to 5 counts;
- 16 have 6 to 19 counts;
- 39 have ≥ 20 counts.

A schematic data presentation is visible in Figure 4.3, while net counts distribution is displayed in Figure 4.4.

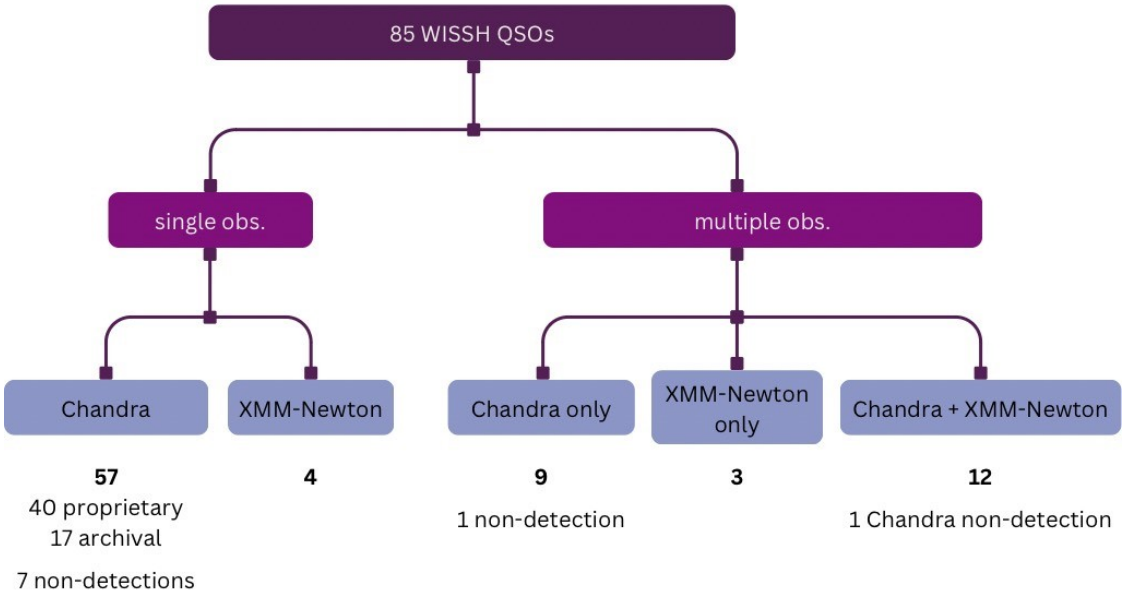

Figure 4.3: WISSH observatories and detections.

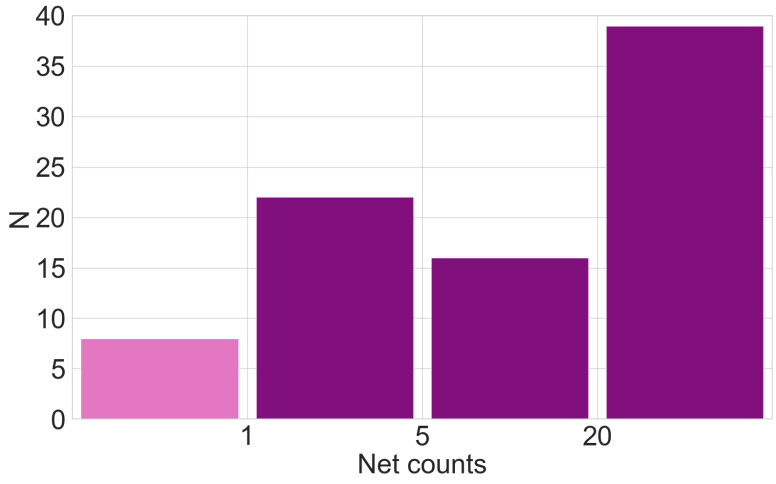

Figure 4.4: WISSH net counts distribution. Pink bar represents upper limits.

5

The WISSH sample in X-rays

The analysis reported in the previous Chapter leads to the derivation of observed $0.5-10$ keV fluxes and intrinsic $2-10$ keV luminosities for the whole WISSH sample. $F_{0.5-10}$ ranges from 3.0×10^{-15} erg s^{-1} cm^{-2} up to 1.4×10^{-12} erg s^{-1} cm^{-2}. Observed fluxes distribution is visible in Figure 5.1, where the yellow dashed line displays the median value. Further considerations are needed to present intrinsic $2-10$ keV luminosity distribution.

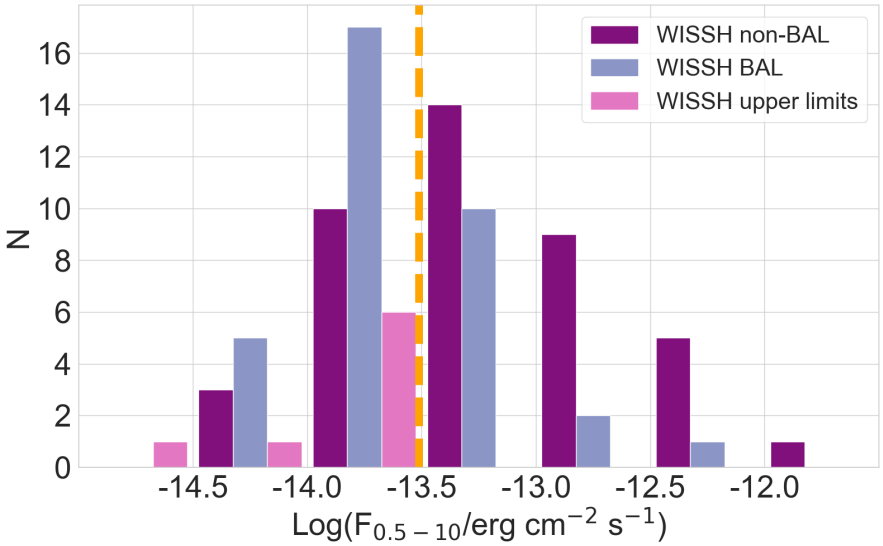

Figure 5.1: Observed $0.5-10$ keV flux distribution for the WISSH sample. BAL quasars are indigo bars, while non-BAL QSOs are represented as purple bars. Pink bars are for undetected sources at 90 % confidence level. The yellow vertical dashed line corresponds to the median value.

5.1 Intrinsic absorption in WISSH QSOs

In Section 4.2.3 and 4.2.4 the intrinsic column densities were derived for the 55/85 quasars with ≥ 6 counts. Only 15/55 ($\sim 27\,\%$) sources exhibit relevant ($> 5 \times 10^{21}$ cm^{-2}) obscuration, while for 40/55 objects upper limits were obtained, thus, broadly confirming Type 1 nature of WISSH source, although some obscuration is present.

Neglecting the huge errors associated with N_H, especially for HR-derived values, Figure 5.2 shows the complete N_H distribution for the WISSH QSOs with ≥ 6 counts. Sources for which the power-law model represents the best fit are included in the bin $N_H < 5 \times 10^{21}$ cm^{-2}. It is evident that the vast majority ($\sim 73\,\%$) of the quasars for which an intrinsic column density estimate is possible result to be unobscured ($N_H < 5 \times 10^{21}$ cm^{-2}). Moreover, the bulk of the subsample with ≥ 6 counts (42/55, i.e. $\sim 76\,\%$) exhibits $N_H < 5 \times 10^{22}$ cm^{-2}. Accordingly, just $\sim 9\,\%$ and $\sim 15\,\%$ of the quasars are moderately (10^{22} cm$^{-2} \leq N_H \leq 10^{23}$ cm^{-2}) or strongly ($N_H > 10^{23}$ cm^{-2}) obscured, respectively. All of the previous results are coherent with those found by M17, and better constrained, as the number of sources in the sample has almost been doubled.

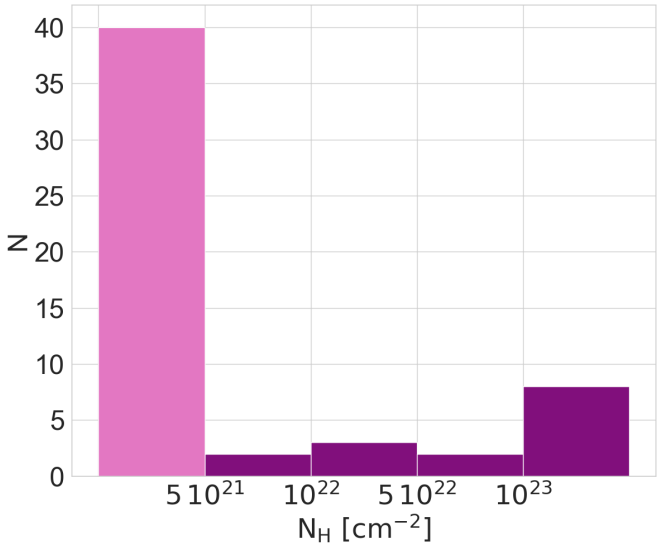

Figure 5.2: Absorbing column density distribution for the 55/85 WISSH sources with ≥ 6 counts, derived from either HR or spectral analysis. Sources for which the power-law model represents the best fit (i.e. with no obscuration required) are included in the bin $N_H < 5 \times 10^{21}$ cm^{-2}.

Since a fraction of WISSH QSOs with ≥ 6 counts exhibits a moderate/strong obscuration up to $N_H > 10^{23}$ cm^{-2}, the assumption of negligible column density in the objects with $1 \leq$ counts ≤ 5 may not be reliable. Considering the subsam-

ple for which a significant N_H has been derived, the median value is calculated: $N_H \sim 8 \times 10^{22}$ cm^{-2}. This absorbing component is introduced in the WebPIMMS modelling, and L_{2-10} are re-obtained for all $1-5$ counts sources but the undetected one. An average variation of 0.05 dex is registered in the intrinsic luminosities. Column (5) in Table 5.1 shows new L_{2-10} values, which will be used in subsequent Sections unless specified otherwise.

In conclusion, intrinsic luminosity ranges 6.6×10^{43} erg s$^{-1} \lesssim L_{2-10} \lesssim 2.4 \times 10^{46}$ erg s^{-1}. Its distribution is presented in Figure 5.3, where the yellow dashed line displays the median value. The extreme strength of the emission clearly emerges. Moreover, it is evident that BAL QSOs (indigo bars) are typically less luminous, as expected (e.g. Brandt et al. 2000, Gibson et al. 2009, Luo et al. 2013, Luo et al. 2014, Liu et al. 2018). There is an overall consistency with the results presented by M17.

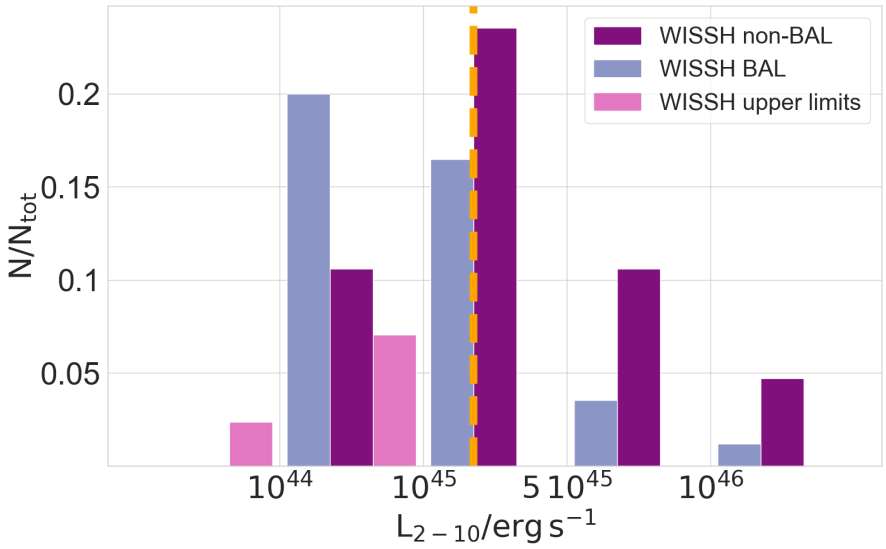

Figure 5.3: Intrinsic $2-10$ keV luminosity distribution for the WISSH sample. BAL quasars are indigo bars, while non-BAL QSOs are represented as purple bars. Pink bars are for undetected sources at 90 % confidence level. The yellow vertical dashed line corresponds to the median value.

5.2 Bolometric correction

The bolometric and intrinsic hard X-ray luminosities are fundamental to calculate bolometric corrections, as defined in Equation 2.5. By definition, bolometric correction describes the relative importance of the hard X-ray emission compared to the total one due to accretion, mostly ascribed to the disk emission in the optical/UV. For WISSH QSOs, k_{bol} distribution has a huge spread, ranging from ~ 30

ID (1)	SDSS ID (2)	z (3)	$N_{H,gal}$ (4)	$Log(L_{2-10})$ (5)	obsCycle (6)
WISSH05	J0216−0921	3.7387	2.91	45.09 ± 0.20	23
WISSH06	J0414+0609	2.6324	10.2	44.46 ± 0.30	23
WISSH11	J0818+0958	3.6943	2.79	45.07 ± 0.20	23
WISSH24	J1020+0922	3.6584	2.89	44.91 ± 0.23	23
WISSH28	J1048+4407	4.408	1.16	44.91 ± 0.20	23
WISSH32	J1106−1731	2.572	4.27	44.94 ± 0.18	23
WISSH38	J1122+1645	3.0398	1.47	44.96 ± 0.20	23
WISSH41	J1159+1337	4.0084	2.07	45.14 ± 0.24	13
WISSH53	J1249−0159	3.6286	1.66	45.05 ± 0.24	13
WISSH55	J1250+2046	3.543	2.08	44.73 ± 0.30	23
WISSH64	J1433+0227	4.728	2.58	45.02 ± 0.20	23
WISSH66	J1447+1038	3.7042	1.56	45.07 ± 0.20	23
WISSH67	J1451+1441	3.0940	1.52	44.98 ± 0.20	23
WISSH68	J1506+5220	4.0995	1.84	44.65 ± 0.22	23
WISSH71	J1538+0855	3.567	3.09	44.88 ± 0.23	23
WISSH72	J1544+4120	3.5513	1.86	44.88 ± 0.23	23
WISSH75	J1555+1003	3.529	3.90	44.73 ± 0.30	23
WISSH76	J1559+4828	3.419	1.69	44.90 ± 0.24	23
WISSH77	J1559+1923	3.9532	2.72	44.84 ± 0.30	23
WISSH81	J1650+2507	3.337	4.63	44.82 ± 0.23	23
WISSH84	J2238−0808	3.1422	3.56	44.76 ± 0.23	23
WISSH85	J2346−0016	3.511	3.71	45.10 ± 0.20	23

Table 5.1: WISSH sources with $1 \leq$ counts ≤ 5. (1) ID; (2) SDSS ID; (3) redshift; (4) Galactic absorption (in units of 10^{20} cm^{-2}); (5) intrinsic $2-10$ keV luminosity (in units of $\mathrm{Log(L/erg\,s^{-1})}$) assuming an intrinsic column density $N_H = 8 \times 10^{22}$ cm^{-2}; (6) Chandra observation Cycle. Errors are reported at 1σ confidence level.

up to ~ 2950. Individual values are reported in Table A.1.

Following M17, in Figure 5.4 the bolometric correction of WISSH QSOs is represented as a function of bolometric luminosity (from Saccheo et al. 2023), along with three lower-luminous samples. XMM-COSMOS (Cosmological Evolution Survey) sample of 343 Type 1 AGN presented by Lusso et al. 2010 is represented with yellow dots; it covers a wide range of redshifts ($0.04 < z < 4.25$) and X-ray luminosities ($40.6 \leq \mathrm{Log(L_{2-10}/erg\,s^{-1}) \leq 45.3}$). 22 SUBWAYS (SUpermassive Black hole Winds in the x-rAYS) quasars and Type 1 AGN at intermediate redshifts ($0.1 \lesssim z \lesssim 0.4$) from Matzeu et al. 2023 can be seen as red dots; SUBWAYS campaign has been designed to provide high Signal-to-Noise Ratio (SNR) for sources at $L_{bol} > 10^{45}$ erg s^{-1}. Light blue triangles correspond to 14 radio-quiet high-Eddington ratio ($\lambda_{Edd} \gtrsim 1$) sources presented by Laurenti et al. 2022; they are

at $0.4 \leq z \leq 0.75$. Studying k_{bol} as a function of L_{bol} is aimed at understanding the behaviour of WISSH QSOs compared to published relations. One of the most commonly used is from Duras et al. 2020 (D20 hereafter). They study the $L_{bol}-k_{bol}$ relation fitting data for ~ 1000 Type 1 and 2 radio quiet sources, spanning seven luminosity decades. Despite the wide L_{bol} coverage, D20 miss the highest-luminosity end of QSO distribution, which can now be properly recovered through the whole WISSH sample. They make use of quasars from five different samples: Swift/BAT 70-month catalog, WISSH (41 objects available at publication time), XMM-COSMOS, ASCA Medium Sensitivity Survey catalog and a subsample from XXL survey. The black solid line represents the relation D20 find fitting Type 1 sources only:

$$k_{bol} = a\left[1 + \left(\frac{Log(L_{bol}/L_{\odot})}{b}\right)^{c}\right] \tag{5.1}$$

where $a = 12.76 \pm 0.13$, $b = 12.15 \pm 0.01$ and $c = 18.78 \pm 0.14$. Black dashed curves correspond to the 0.26 dex spread of the same relation. D20 relation is almost flat at low luminosities (i.e. in the range $7.5 < Log(L_{bol}/L_{\odot}) < 11$), while it increases at $Log(L_{bol}/L_{\odot}) > 11$.

Although M17 populate the $L_{bol} - k_{bol}$ plane with lower statistics, they still notice the incoherent distribution of WISSH QSOs with respect to literature relations (e.g. Lusso et al. 2012). Doubling the sample, it broadly follows the increasing trend of k_{bol} in more luminous sources, but seems to distribute perpendicularly to that, also due to the narrow range of bolometric luminosities in the WISSH sample. The anomalous distribution of WISSH QSOs and high-λ_{Edd} sources is more evident in Figure 5.5, where the vertical axis displays the ratio between the observed bolometric corrections and the expected ones at the same L_{bol} from D20 relation $\left(\frac{k_{bol,obs}}{k_{bol,D20}}\right)$. As a consequence, one single relation may not be sufficient to fit the whole distribution of AGN. In particular, caution has to be taken when dealing with sources at $L_{bol} \gtrsim 10^{13} - 10^{14}$ $L_{\odot}$.

Remembering that $L_{bol} \sim L_{UV}$ for Type 1 quasars, as the accretion disk emission is the dominant one, the bolometric correction compares (X-ray) coronal and (optical/UV) accretion disk emission. Thus, relative importance of X-ray contribution with respect to the UV one decreases at the highest end of the QSOs luminosity function. Moreover, the large spread in Figures 5.4 and 5.5 points towards a wide variety of coronal - accretion disk coupling occurring in extremely luminous sources, that will be discussed further.

As expected, due to the presence of obscuration depressing their X-ray emission, BAL quasars are mainly ($\sim 55\,\%$) located above the D20 relation. In other words, at a given L_{bol}, they are more often characterised by weaker X-ray emission.

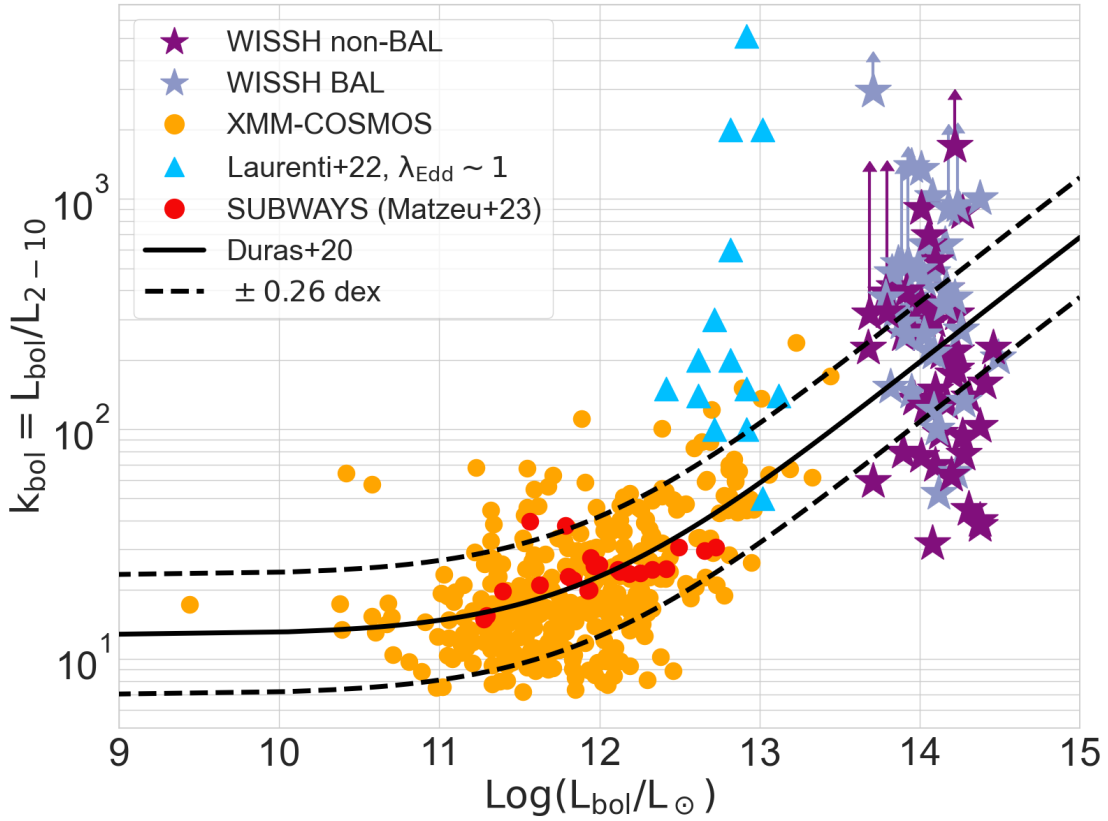

Figure 5.4: Bolometric correction as a function of bolometric luminosity (in units of $\mathrm{Log(L/L_\odot)}$ - from Saccheo et al. 2023). WISSH BAL quasars are indigo stars, while WISSH non-BAL QSOs are purple stars. XMM-COSMOS and SUBWAYS samples are yellow and red dots, respectively. $\lambda_{\mathrm{Edd}} \gtrsim 1$ sources from Laurenti et al. 2022 are light blue triangles. The black solid and dashed lines correspond to D20 best fit to Type 1 sources and its 0.26 dex spread, respectively.

Nonetheless, a non negligible fraction of $\sim 35\,\%$ and $\sim 10\,\%$ of WISSH BAL QSOs fall within and below D20 spread, respectively. On the other hand, non-BAL objects are more equally distributed: $\sim 27\,\%$ above, $\sim 38\,\%$ within and $\sim 36\,\%$ below the best-fit relation. To summarise, only $\sim 36\,\%$ of the whole WISSH sample falls within the adopted relation spread, while $\sim 64\,\%$ is distributed above ($\sim 40\,\%$) and below ($\sim 24\,\%$) it. The complete distribution is visible in Figure 5.6.

X-ray weakness is fundamental to prevent over-ionisation of the gas in the accretion disk atmosphere, favouring radiation driven winds launch. Hence, X-ray observations are consistent with results in the optical/UV band for WISSH QSOs (Vietri et al. 2018, Bischetti et al. 2017, Zappacosta et al. 2020), which highlight the presence of extreme outflows (see Section 2.1).

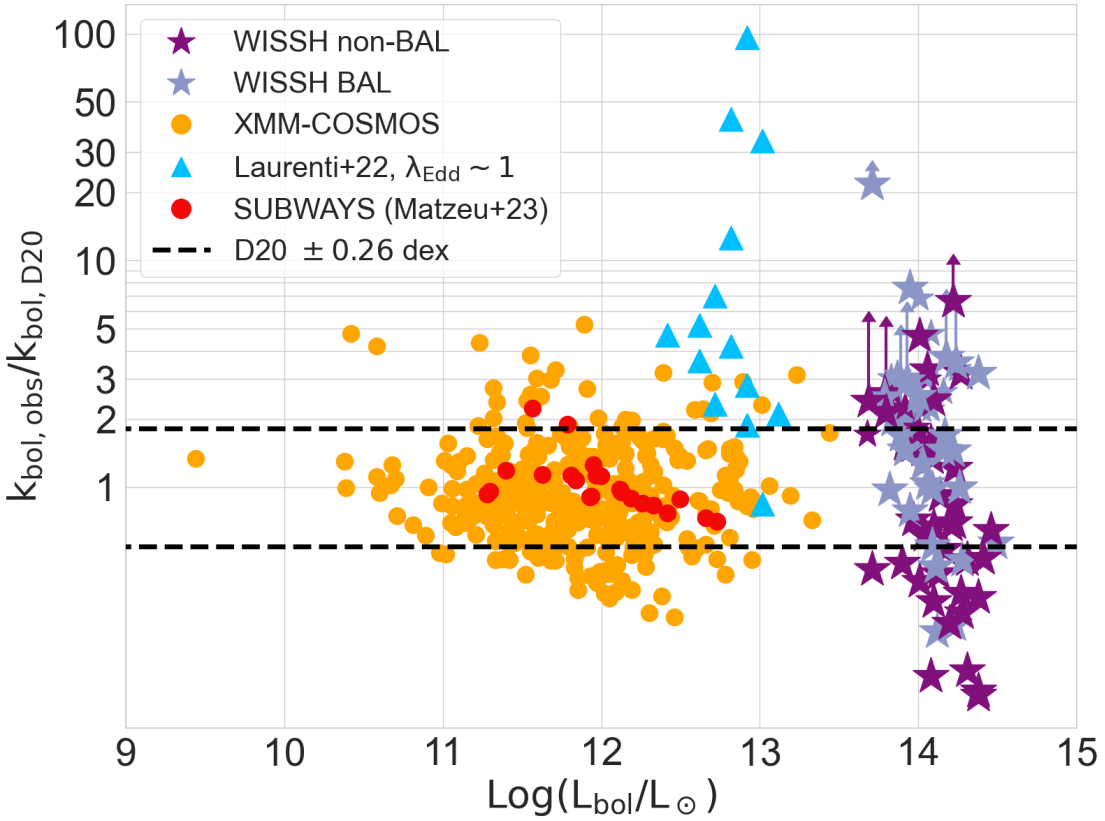

Figure 5.5: Observed - to - expected bolometric correction ratio as a function of bolometric luminosity (in units of $\mathrm{Log(L/L_{\odot})}$). Expected bolometric corrections refer to the value derived from D20 relation at a given bolometric luminosity. Symbols are the same as in Figure 5.4. The two black dashed lines correspond to the 0.26 dex spread of D20 best fit to Type 1 sources.

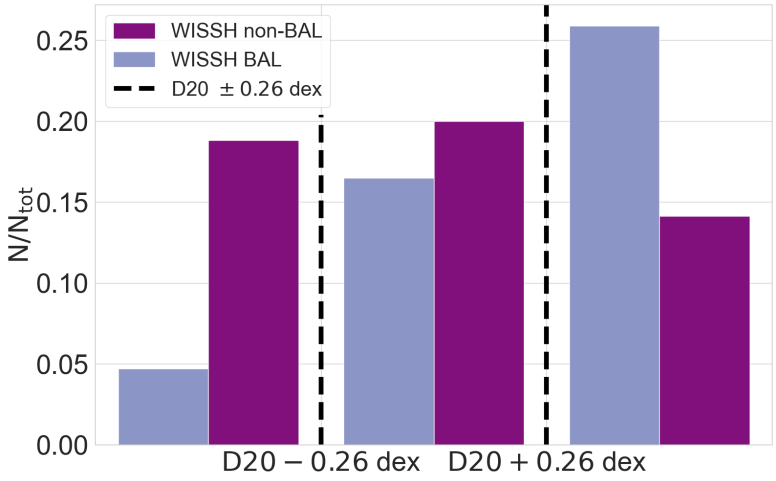

Figure 5.6: WISSH QSOs bolometric corrections grouped in terms of their "location" in the D20 relation, i.e. being below, within or above the relation including its spread (black vertical dashed lines). BAL and non-BAL sources are represented as indigo and purple bars, respectively.

5.3 X-ray - to - optical spectral index

The comparison between X-ray and UV emission corresponds, by definition, to the X-ray - to - optical spectral index (Equation 2.6). α_{OX} values for WISSH QSOs are reported in Table A.1, they are derived using L_{2500} from Saccheo et al. 2023. More negative α_{OX} values indicate steeper slopes, thus more prominent optical/UV emission compared to the X-ray one, or, equivalently, weaker X-ray sources at a given optical luminosity.

The WISSH sample lies in the bottom-right region of the $L_{2500} - \alpha_{OX}$ plane: hyper-luminous quasars are the X-ray weakest sources. In Figure 5.7, WISSH BAL and non-BAL objects are shown as indigo and purple stars, respectively; XMM-COSMOS sample is represented as yellow dots, while $\lambda_{Edd} \gtrsim 1$ sources from Laurenti et al. 2022 are light blue triangles. M17, Lusso et al. 2010 and Just et al. 2007 relations are chosen as representative of the numerous literature works, and are reported as black solid, dashed and dotted lines, respectively. From Section 5.2, this result is expected in Type 1 sources ($L_{bol} \sim L_{UV}$), as k_{bol} and α_{OX} describe relative importance of coronal emission compared to the bolometric and AD ones, respectively. As in the $L_{bol} - k_{bol}$ plane, WISSH QSOs broadly follow the decreasing trend at higher UV luminosities proposed by previous papers (e.g. Lusso et al. 2010, Just et al. 2007) and already observed by M17 with lower statistic. In particular, Lusso et al. 2010 fitted XMM-COSMOS data only; Just et al. 2007 considered 34 quasars of their core sample (32 quasars from the SDSS DR3 quasar catalog and two additional objects in the DR3 area that were missed by the SDSS selection criteria), 332 sources from Steffen et al. 2006 and 14 from Shemmer et al. 2006; M17 relation is based on XMM-COSMOS objects, 23 optically selected quasars from the Palomar-Green (PG) Bright Quasar Survey of the complete sample by Laor et al. 1994 and WISSH data for 41 objects available when the paper was published (Figure 2.8). At the same time, α_{OX} covers a wider range for a fixed L_{2500} than the XMM-COSMOS lower-luminosity sample, again, also due to the narrow L_{2500} range for WISSH QSOs. This evidence points towards an "heterogeneous" nature of the accretion disk - corona system.

Measuring the offset between the observed values $\alpha_{OX,obs}$ and those expected from M17 relation ($\alpha_{OX,M17}$) at a given L_{2500}, $\Delta(\alpha_{OX})$ can be defined as

$$\Delta(\alpha_{OX}) = \alpha_{OX,obs} - \alpha_{OX,M17} \tag{5.2}$$

The resulting values for WISSH QSOs are reported in Table A.1. It can be used to distinguish X-ray weak sources from the rest of the sample; in particular, the

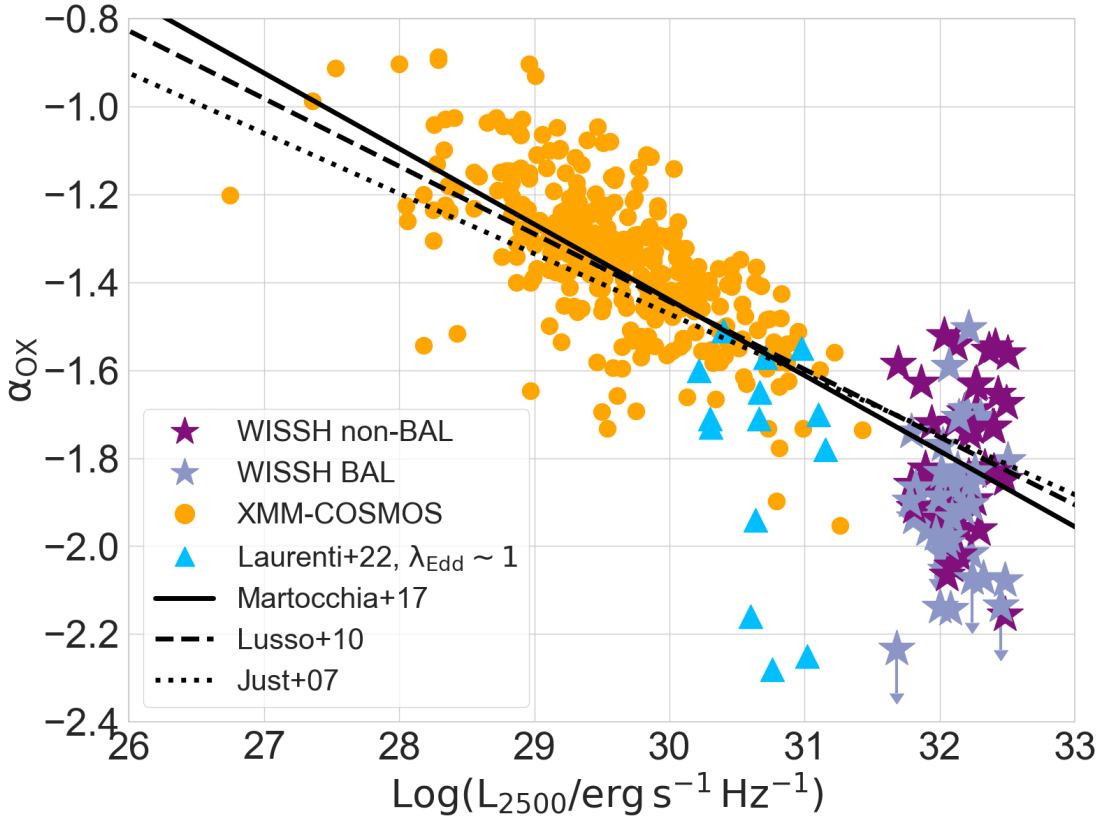

Figure 5.7: X-ray - to - optical index (α_{OX}) as a function of 2500 Å luminosity (from Saccheo et al. 2023). WISSH BAL quasars are indigo stars, while WISSH non-BAL QSOs are purple stars. XMM-COSMOS objects are yellow dots. $\lambda_{Edd} \gtrsim 1$ sources from Laurenti et al. 2022 are light blue triangles. Black solid, dashed and dotted lines are the best fit from M17, Lusso et al. 2010 and Just et al. 2007, respectively.

threshold is fixed to $\Delta(\alpha_{OX}) < -0.2$, as in Luo et al. 2015. Figure 5.8 shows the $\Delta(\alpha_{OX})$ distribution, where BAL and non-BAL QSOs are presented as indigo and purple bars, respectively, while the pink bar corresponds to undetected sources. The X-ray weak region is highlighted with the yellow rectangle; $\sim 22\,\%$ of WISSH quasars results to fall under this category. In particular, $\Delta(\alpha_{OX})$ value is below the adopted threshold for $\sim 30\,\%$ and $\sim 16\,\%$ of BAL and non-BAL objects, respectively (considering the BAL classification also for the undetected sources). In addition to that, it is evident that BAL and non-BAL quasars are differently distributed: the Kolmogorov-Smirnov (KS) test is performed, and p = 0.006 is derived.

For sources with ≥ 20 counts and, thus, Γ derived from spectral analysis, a possible correlation between the spectral index and $\Delta(\alpha_{OX})$ is searched for. Figure 5.9 exhibits the X-ray spectral index as a function of $\Delta(\alpha_{OX})$: in the *top panel*, Γ is derived applying a simple power-law model with Galactic absorption only; the presence of a significant intrinsic column density (see Sections 4.2.3 and 4.2.4) is

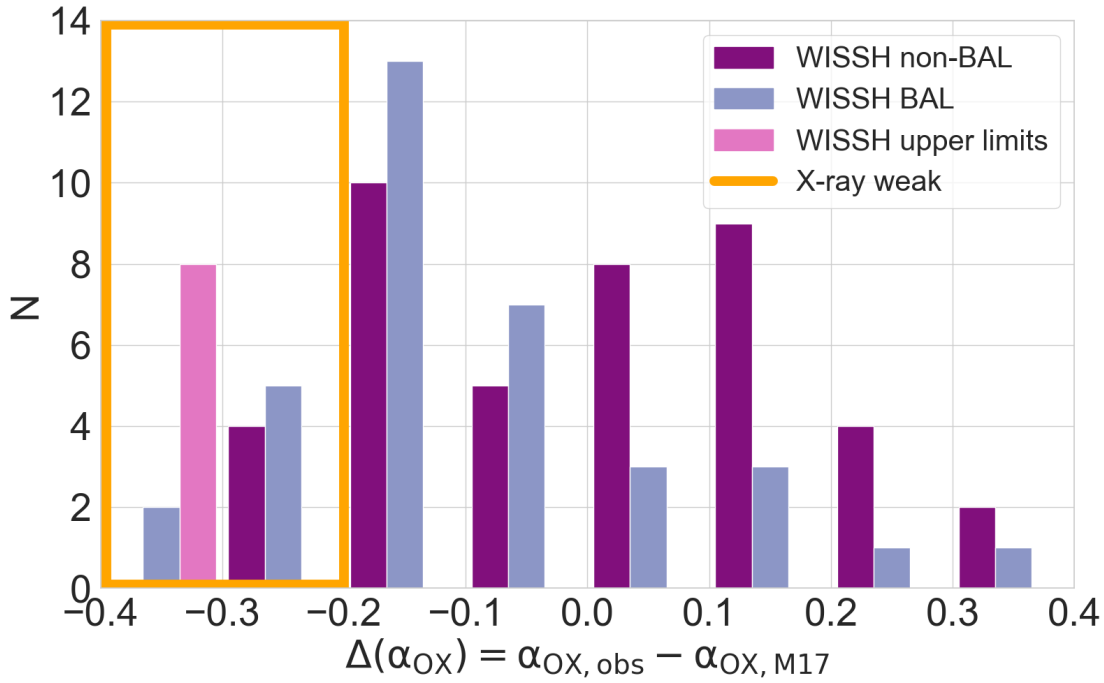

Figure 5.8: $\Delta(\alpha_{OX}) = \alpha_{OX,obs} - \alpha_{OX,M17}$ distribution. Expected X-ray - to - optical indices ($\alpha_{OX,M17}$) refer to the value derived from M17 relation at a given L_{2500}. BAL and non-BAL quasars are represented as indigo and purple bars, respectively. Pink bar is for undetected sources, which have all been included in the bin $\Delta(\alpha_{OX}) < -0.2$. The yellow rectangle highlights X-ray weak sources.

taken into consideration in the *bottom panel*. As expected, the main variations occur at the lowest $\Delta(\alpha_{OX})$: suppression of the soft X-ray component by intrinsic N_H causes both Γ flattening and X-ray weakening with respect to the optical/UV emission. Moreover, once the best fit including intrinsic N_H is applied *(bottom panel)*, Spearman's rank test gives a rank coefficient of $\rho_s = 0.36$ ($p = 0.03$). Thus, no correlation emerges between the two quantities. However, additional non-revealed obscuration may be present in X-ray weaker sources.

5.4 Black hole mass and Eddington ratio

For 36/85 sources ($\sim 42\,\%$), a black hole mass estimate is available (Bischetti et al. 2017, Vietri et al. 2018, Vietri et al. in prep.). They are derived through a single epoch virial method relation (Bongiorno et al. 2014), which depends on the Hβ line FWHM and the continuum luminosity at 5100 Å (λL_λ):

$$\mathrm{Log}(M_{BH}/M_\odot) = 6.7 + 2\,\mathrm{Log}\left(\frac{\mathrm{FWHM}_{H\beta}}{10^3\ \mathrm{km\,s^{-2}}}\right) + 0.5\,\mathrm{Log}\left(\frac{\lambda L_\lambda}{10^{44}\ \mathrm{erg\,s^{-1}}}\right) \qquad (5.3)$$

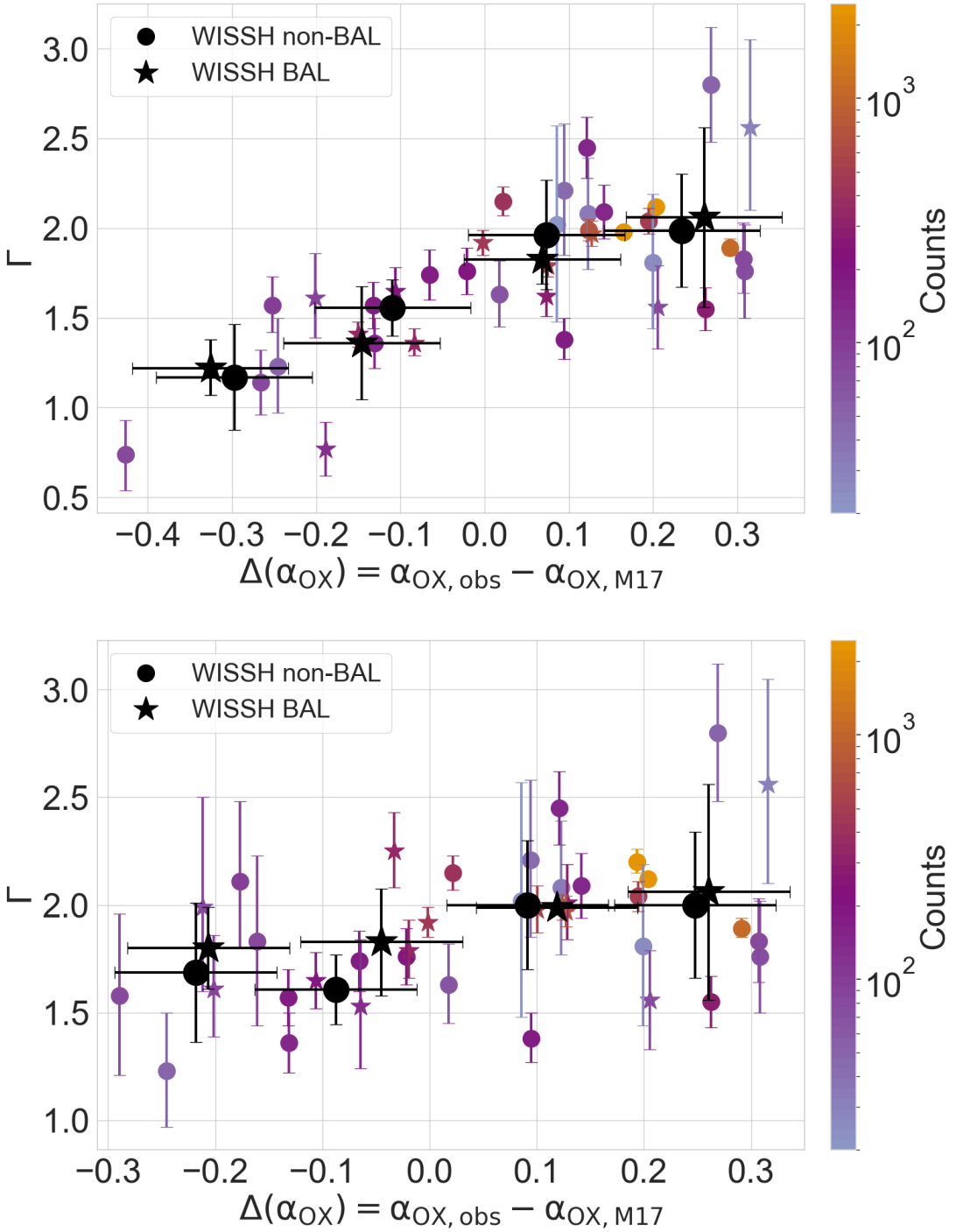

Figure 5.9: X-ray spectral index Γ as a function of $\Delta(\alpha_{OX})$ for the sources with ≥ 20 counts. *(Top)* Γ is derived through spectral analysis using a simple power-law model with Galactic absorption. *(Bottom)* Significant intrinsic column density (see Sections 4.2.3 and 4.2.4) is included in the spectral model used to derive Γ. BAL and non-BAL quasars are represented as stars and dots, respectively. Colours are based on the available X-ray net counts, and errors are reported at 1σ confidence level. Black symbols represent mean values in each $\Delta(\alpha_{OX})$ bin: y-axis error bars correspond to standard deviation of Γ distribution within each bin.

The systematic uncertainty in the Log(M_{BH}) determination is estimated in about 0.3 dex (Bongiorno et al. 2014). Hβ-based SMBH masses are chosen over MgII- and CIV-derivations. Indeed, the former results in systematically smaller M_{BH} compared to Hβ-estimates, maybe due to an improper modelling of the iron emission line, which overlaps with the MgII one; the latter typically exhibits an asymmetric profile, which can not be ascribed to virialised motion, but is likely due to outflowing gas (e.g. Denney 2012, Coatman et al. 2017). Black hole mass values are reported in Table 5.2: all of the BH masses are larger than 10^9 $M_\odot$, with 26/36 quasars hosting supermassive black holes with $M_{BH} > 5 \times 10^9$ $M_\odot$.

ID (1)	SDSS ID (2)	M_{BH} (3)	ID (1)	SDSS ID (2)	M_{BH} (3)
WISSH06	J0414+0609	6.3[a]	WISSH53	J1249−0159	10.0[a]
WISSH08	J0745+4734	15.7[c]	WISSH57	J1310+4601	4.0[a]
WISSH10	J0801+5210	6.2[b]	WISSH58	J1326−0005	2.1[c]
WISSH11	J0818+0958	7.7[a]	WISSH61	J1421+4633	6.2[b]
WISSH13	J0900+4215	2.1[c]	WISSH62	J1422+4417	4.4[b]
WISSH16	J0941+3257	6.3[a]	WISSH63	J1426+6025	24.9[a]
WISSH19	J0958+2827	3.5[b]	WISSH67	J1451+1441	26.4[a]
WISSH21	J1013+5615	8.7[a]	WISSH70	J1521+5202	9.98[b]
WISSH22	J1014+4300	8.4[a]	WISSH71	J1538+0855	5.5[b]
WISSH27	J1027+3543	13.8[a]	WISSH72	J1544+4120	23.4[a]
WISSH33	J1106+6400	10.0[b]	WISSH73	J1549+1245	12.6[c]
WISSH34	J1110+1930	10.4[a]	WISSH76	J1559+4828	7.0[a]
WISSH37	J1111+1336	8.5[b]	WISSH78	J1621−0042	6.8[a]
WISSH40	J1157+2724	2.6[b]	WISSH79	J1633+3629	12.5[a]
WISSH43	J1201+0116	3.2[b]	WISSH80	J1639+2824	8.5[a]
WISSH44	J1201+1206	6.5[c]	WISSH83	J2123−0050	3.9[b]
WISSH45	J1204+3309	5.9[a]	WISSH84	J2238−0808	11.1[a]
WISSH50	J1236+6554	4.3[b]	WISSH85	J2346−0016	4.3[b]

Table 5.2: Hβ-derived black hole masses for the WISSH sample: (1) ID; (2) SDSS ID; (3) black hole mass (in units of 10^9 $M_\odot$) with a typical uncertainty of 0.3 dex. [a] From Vietri et al. (in prep.). [b] From Vietri et al. 2018. [c] From Bischetti et al. 2017.

Subsequently, Eddington luminosities are derived from Equation 1.5, obtaining values between 1.3×10^{47} erg s^{-1} and 3.3×10^{48} erg s^{-1}. In Figure 5.10, WISSH black hole masses and bolometric luminosities are compared with those from XMM-COSMOS sources. WISSH BAL and non-BAL objects are shown as indigo and purple stars, respectively, while yellow dots represent XMM-COSMOS quasars. Black solid, dashed and dotted lines correspond to L_{Edd} equal to 100 %, 50 % and 10 % of L_{bol}. The extreme nature of WISSH QSOs is evident, as they occupy the most massive and luminous end of M_{BH} and L_{bol} distributions. As a consequence,

their Eddington luminosities broadly correspond to higher fractions of their bolometric ones.

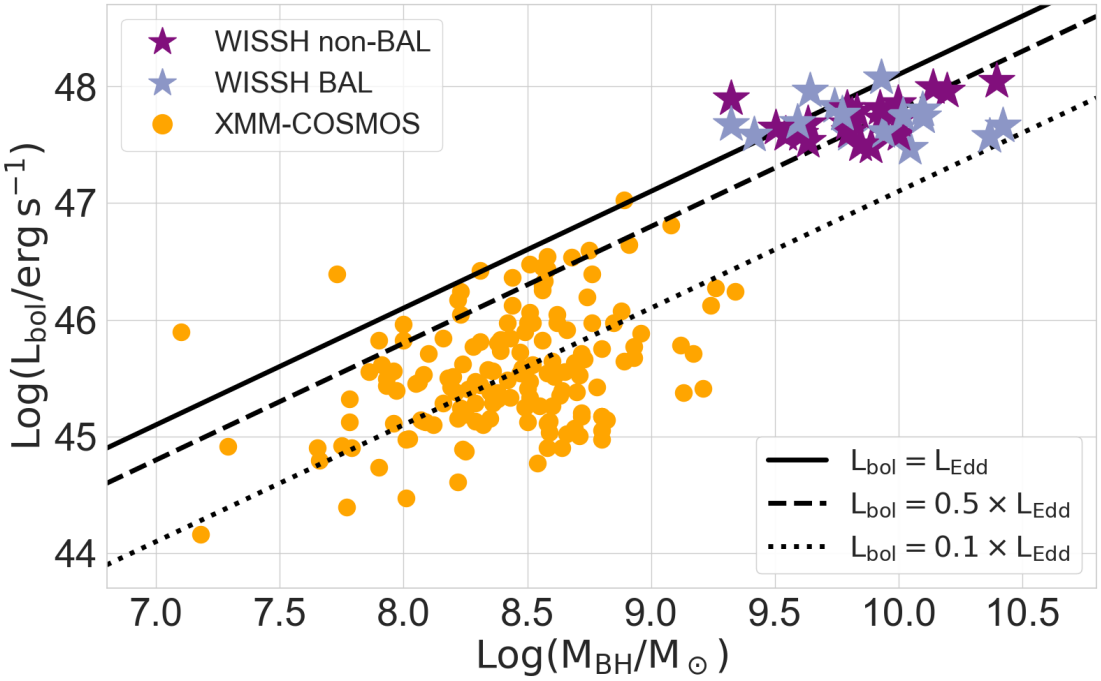

Figure 5.10: Bolometric luminosity as a function of black hole mass of WISSH sources for which an Hβ-estimate of M_{BH} is available. WISSH BAL and non-BAL objects are indigo and purple stars, respectively, while yellow dots represent XMM-COSMOS quasars. Black solid, dashed and dotted lines correspond to L_{Edd} equal to 100 %, 50 % and 10 % of L_{bol}, respectively.

Having both bolometric and Eddington luminosities, Eddington ratios are derived from Equation 1.5, resulting in a range between 0.1 and 2.8, with a median value 0.7. λ_{Edd} values are reported in Table A.1. These values support the extreme-accretion regime that are expected in hyper-luminous quasars at the cosmic noon.

The possibility to derive a fundamental parameter as λ_{Edd} from Γ is very attractive, thus different authors tried to find a correlation. Such a relation is expected as higher λ_{Edd} corresponds to more intense disk emission, thus a more efficient coronal Compton cooling, which leads to a softer (i.e. steeper) spectral index (e.g. Haardt et al. 1991, Haardt et al. 1993, Pounds et al. 1995, Fabian et al. 2015, Cheng et al. 2020). In Figure 5.11, the X-ray spectral index is studied as a function of Eddington ratio. WISSH BAL and non-BAL objects are indigo and purple stars, respectively; $\lambda_{Edd} \gtrsim 1$ sources from Laurenti et al. 2022 are light blue triangles, while SUBWAYS sample is shown as red dots. Black solid, dashed, dotted and dash-dotted lines correspond to Liu et al. 2021, Brightman et al. 2013, and two models (BCES bisector - following Akritas et al. 1996; FITEXY method - following Tremaine et al. 2002) from Trakhtenbrot et al. 2017 relations, respectively. In

particular, Liu et al. 2021 consider 47 AGN with both Super- and Sub-Eddington accretion rates from the sample compiled by the SEAMBH collaboration (Du et al. 2015, Du et al. 2016, Du et al. 2018). Brightman et al. 2013 use 69 broad-line AGN from the extended Chandra Deep Field South (E-CDF-S, Lehmer et al. 2005), inclusive of the ultradeep central area (e.g. Giacconi et al. 2002, Luo et al. 2008, Xue et al. 2011), and COSMOS surveys. Trakhtenbrot et al. 2017 refer to 228 hard X-ray selected AGN at $0.01 < z < 0.5$, drawn from the Swift/BAT AGN Spectroscopic Survey (BASS, Baumgartner et al. 2013). Only 19/85 WISSH sources are represented, which have either an available Hβ-derived BH mass estimate and ≥ 20 counts to perform spectral analysis. A correlation seems to be present in low-accretion regimes, but data show a large spread around $\lambda_{\rm Edd} \approx 1$ and no relation emerges.

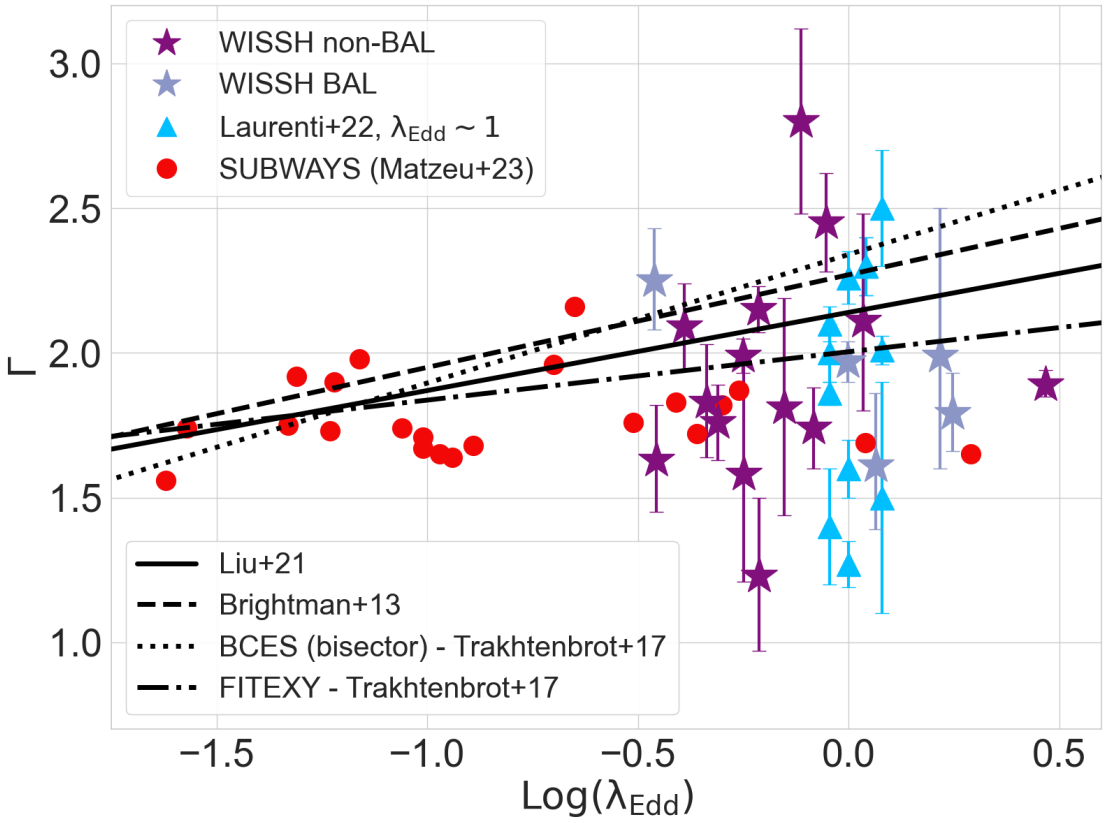

Figure 5.11: X-ray spectral index as a function of Eddington ratio for WISSH sources. Only quasars with ≥ 20 counts (i.e. with spectral analysis), for which an Hβ estimate of $M_{\rm BH}$ is available are considered. WISSH BAL and non-BAL objects are indigo and purple stars, respectively; $\lambda_{\rm Edd} \gtrsim 1$ sources from Laurenti et al. 2022 are light blue triangles, while SUBWAYS sample is shown as red dots. Black solid, dashed, dotted and dash-dotted lines correspond to Liu et al. 2021, Brightman et al. 2013, and two models (BCES bisector - following Akritas et al. 1996; FITEXY method - following Tremaine et al. 2002) from Trakhtenbrot et al. 2017 relations, respectively. Uncertainties are reported at 1σ confidence level.

As introduced in Section 2.3, the relation between the Eddington ratio and intrinsic column density is studied. Combining the available information on Hβ-derived black hole masses and intrinsic column densities (either from spectral analysis or hardness ratio modelling - thus, objects with ≥ 6 counts), the $\lambda_{\rm Edd} - {\rm N_H}$ plane can be populated. Figure 5.12 reports WISSH QSOs only, where BAL and non-BAL objects are triangles and stars, respectively; sources with a significant intrinsic column density (see Sections 4.2.3 and 4.2.4) have been coloured depending on their $\Delta(\alpha_{\rm OX})$ (3/6 are X-ray weak). Moreover, red quasars (Section 2.3) are surrounded with a circle. Despite being expected in the blowout region (e.g. Glikman 2017, Lansbury et al. 2020), as transitioning from dust-obscured to unobscured blue quasar phase, it emerges that only 1/3 of the plotted WISSH red sources robustly occupy the forbidden area, while another one likely does, due to its extremely thick $\rm N_H$ upper limit. On the other hand, all of the five blue objects with a significant intrinsic column density are located in the feedback area, and a higher statistic is expected to locate more properly the current upper limits.

5.5 Mid-infrared luminosity

The X-ray and mid-IR emissions are strictly connected in QSOs, as the former is coronal emission of accretion disk Comptonised photons, while the latter is their re-emission once being absorbed and thermalised by the dusty torus. Thus, a positive correlation is expected in the $\rm L_{6\,\mu m} - L_{2-10}$ plane (see Section 2.5). Furthermore, unless extreme column densities are considered, mid-infrared radiation is largely unaffected by obscuration, differently from X-ray. Several authors therefore adopt AGN mid-IR luminosity as a robust indicator of their intrinsic strength. Then, the presence of intrinsic $\rm N_H$ can be derived comparing expected (from the $\rm L_{6\,\mu m} - L_{2-10}$ relation) and observed X-ray luminosity (e.g. Fiore et al. 2008, Fiore et al. 2009, Georgantopoulos et al. 2011, Luo et al. 2013, Lansbury et al. 2014, Rovilos et al. 2013, Stern et al. 2014).

Many efforts initially focused on low-luminosity samples to determine the aforementioned relation: Lutz et al. 2004 and Gandhi et al. 2009 study local Type 1 and Type 2 Seyfert galaxies, therefore exploring the lowest-luminosity range; Fiore et al. 2009 inspect higher luminosities through unobscured AGN in the COSMOS field, while Lanzuisi et al. 2009 investigate obscured sources within the SWIRE survey area in a similar luminosity regime as Fiore et al. 2009. Good agreement is found in the low-luminosity regime, but extrapolations towards the high-luminosity end of the distribution differ by up to an order of magnitude at $\lambda {\rm L_{6\,\mu m}} \sim 10^{47}$ erg s^{-1}.

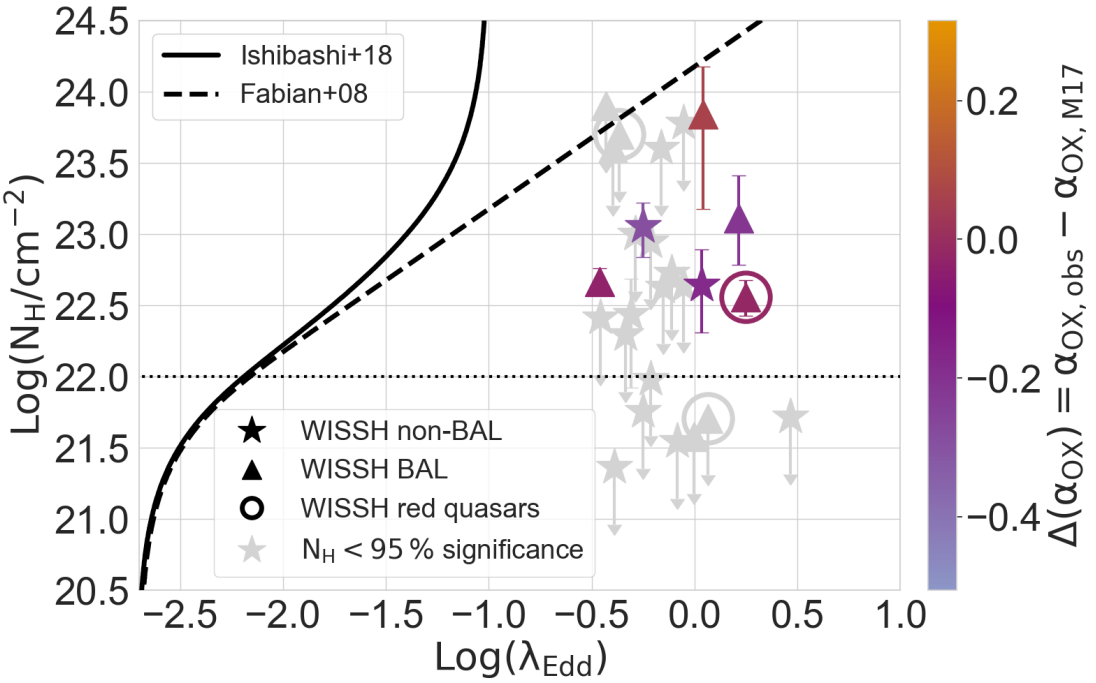

Figure 5.12: Intrinsic column density (in units of $\mathrm{Log}(\mathrm{N_H/cm^{-2}})$) as a function of Eddington ratio. Only WISSH sources for which an Hβ-estimate of $\mathrm{M_{BH}}$ and $\mathrm{N_H}$ (thus, with ≥ 6 counts) are available are reported. WISSH BAL and non-BAL objects are triangles and stars, respectively. Sources with a significant $\mathrm{N_H}$ (see Sections 4.2.3 and 4.2.4) are coloured depending on their $\Delta(\alpha_{\mathrm{OX}})$, from Section 5.3: 3/6 quasars result being X-ray weak. The other sources (i.e. those with rmN_H significance $< 95\,\%$) are represented as grey symbols. Red quasars (Section 2.3) are surrounded with a circle. Black solid and dashed lines are Ishibashi et al. 2018 and Fabian et al. 2008 relations, derived from a maximal- and no-photon trapping model, respectively. The black horizontal dotted line highlights $\mathrm{N_H} = 10^{22}$ cm^{-2}. Errors and upper limits are reported at 1σ confidence level.

More recently, the highest-luminosity end of the distribution was the subject of some publications. In particular, Mateos et al. 2015 derive a linear relation in the logarithmic plane (black solid line in Figure 5.13) making use of 232 Type 1 and Type 2 sources at $0.05 < \mathrm{z} < 2.8$ from the Bright Ultra-hard XMM-Newton survey; luminosities at 6 μm are from WISE. Based on 3247 Type 1 AGN from Boötes, XMM-COSMOS, XMM-XXL-North, and SDSS in the Swift/XRT footprint, Chen et al. 2017 find a bilinear relation in the Log − Log plane (black dash-dotted line in Figure 5.13).

Stern 2015 (S15 hereafter) relies on published works for the lowest-luminosity sample of local Seyfert galaxies (e.g. Lutz et al. 2004, Horst et al. 2007, Gandhi et al. 2009). Intermediate sub-samples are taken from the Serendipitous Extragalactic X-ray Source Identification (SEXIS) program (Eckart et al. 2009) and SDSS DR5 (Young et al. 2009). The most luminous quasars from SDSS DR3 (Just et al. 2007) are also included. Finally, various NuSTAR (Nuclear Spectroscopic Telescope

Array)-detected sources are also reported. Doing a least-square polynomial fit to the data, S15 obtains

$$\mathrm{Log}\Big(\frac{\mathrm{L}_{2-10}}{\mathrm{erg\,s^{-1}}}\Big) = 40.981 + 1.024\,x - 0.047\,x^2 \tag{5.4}$$

where $x = \mathrm{Log}(\lambda \mathrm{L}_{6\,\mu\mathrm{m}}/10^{41}\ \mathrm{erg\,s^{-1}})$. It is represented as a black dotted curve in Figure 5.13.

By construction, all 85 WISSH quasars have been detected in the WISE 3.3 μm band, from which luminosity at 6 μm can be recovered applying a correction derived from the mean SED of the sample (Saccheo et al. 2023). $\mathrm{Log}(\mathrm{L}_{6\,\mu\mathrm{m}})$ values are reported in Table 5.3: they range from 46.75 up to 47.55.

In Figure 5.13 the X-ray intrinsic luminosity is studied as a function of $\mathrm{L}_{6\,\mu\mathrm{m}}$. WISSH BAL and non-BAL objects are indigo and purple stars, respectively, while yellow dots are comparison samples from Lanzuisi et al. 2009, S15 and Mateos et al. 2015. An overall positive correlation emerges, although it seems to flatten at the highest $\mathrm{L}_{6\,\mu\mathrm{m}}$. This represents another evidence of the characteristic X-ray weakness of most of the WISSH QSOs. Despite the limited range in terms of $\mathrm{L}_{6\,\mu\mathrm{m}}$ due to the selection, WISSH sources cover a wide vertical range of L_{2-10}. Thus, something differs between hyper-luminous quasars and lower-luminous ones in the innermost regions inside the torus.

Similarly to the derivation of the $\Delta(\alpha_{\mathrm{OX}})$ parameter, the vertical offset of WISSH QSOs from the relation by S15 has been studied:

$$\Delta_{6\,\mu\mathrm{m,\,X}} = \mathrm{Log}(\mathrm{L}_{2-10,\,\mathrm{obs}}) - \mathrm{Log}(\mathrm{L}_{2-10,\,\mathrm{S15}}) \tag{5.5}$$

It is compared with $\Delta(\alpha_{\mathrm{OX}})$ in Figure 5.14, where WISSH BAL and non-BAL objects are indigo and purple stars, respectively. A strong positive correlation is evident and has been fitted with a first order relation, resulting in the following equation:

$$\Delta(\alpha_{\mathrm{OX}}) = 0.36\,\Delta_{6\,\mu\mathrm{m,\,X}} + 0.04 \tag{5.6}$$

which is represented as a solid black line in Figure 5.14. Such a strict relation makes it possible to "translate" the $\Delta(\alpha_{\mathrm{OX}})$-based definition of X-ray weak source (yellow horizontal dashed line - $\Delta(\alpha_{\mathrm{OX}}) < -0.2$) into the $\Delta_{6\,\mu\mathrm{m,\,X}}$ parameter, resulting in

$$\Delta_{6\,\mu\mathrm{m,\,X}} < -0.65 \tag{5.7}$$

which is highlighted by the yellow vertical dashed line.

To summarise, WISSH QSOs display anomalous properties in the $\mathrm{L_{bol}}-\mathrm{k_{bol}}$ and

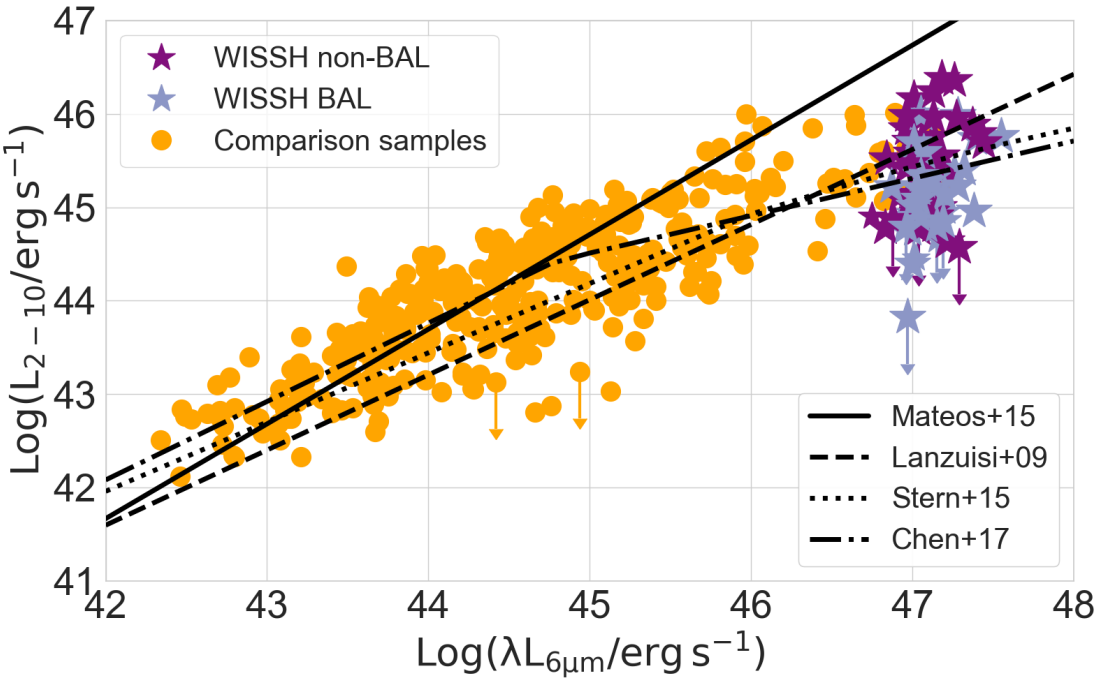

Figure 5.13: Intrinsic $2-10$ keV luminosity as a function of 6 μm luminosity. WISSH BAL and non-BAL objects are indigo and purple stars, respectively, while yellow dots represent various comparison samples from Lanzuisi et al. 2009, S15 and Mateos et al. 2015. Black solid, dashed, dotted and dash-dotted lines correspond to relation by Mateos et al. 2015, Lanzuisi et al. 2009, S15 and Chen et al. 2017, respectively.

$L_{2500} - \alpha_{OX}$ planes; however, caution has to be used due to the limited bolometric and UV luminosity range of the present sample. Moreover, the relevant number of objects located above (below) the expected k_{bol} (α_{OX}) values hints towards an X-ray weak nature of hyper-luminous quasars, which seems to be intrinsic.

$\lambda_{Edd} \gtrsim 1$ values are calculated from Hβ-derived BH masses. Figure 5.11 highlights that caution has to be taken when deriving the X-ray spectral index from the Eddington ratio, due to data dispersion at high λ_{Edd}. The $\lambda_{Edd} - N_H$ plane is also studied, showing that not only red quasars, but also blue ones occupy the forbidden region.

Finally, an offset of WISSH values from literature relations is also present in the $L_{6\,\mu m} - L_{2-10}$ plane. In particular, a strong correlation is find between the distance of WISSH data from expected X-ray luminosity from S15 relation ($\Delta_{6\,\mu m,X}$), and $\Delta(\alpha_{OX})$. Thus, X-ray weak definition - $\Delta(\alpha_{OX}) < -0.2$ - can be "translated" as $\Delta_{6\,\mu m,X} < -0.65$.

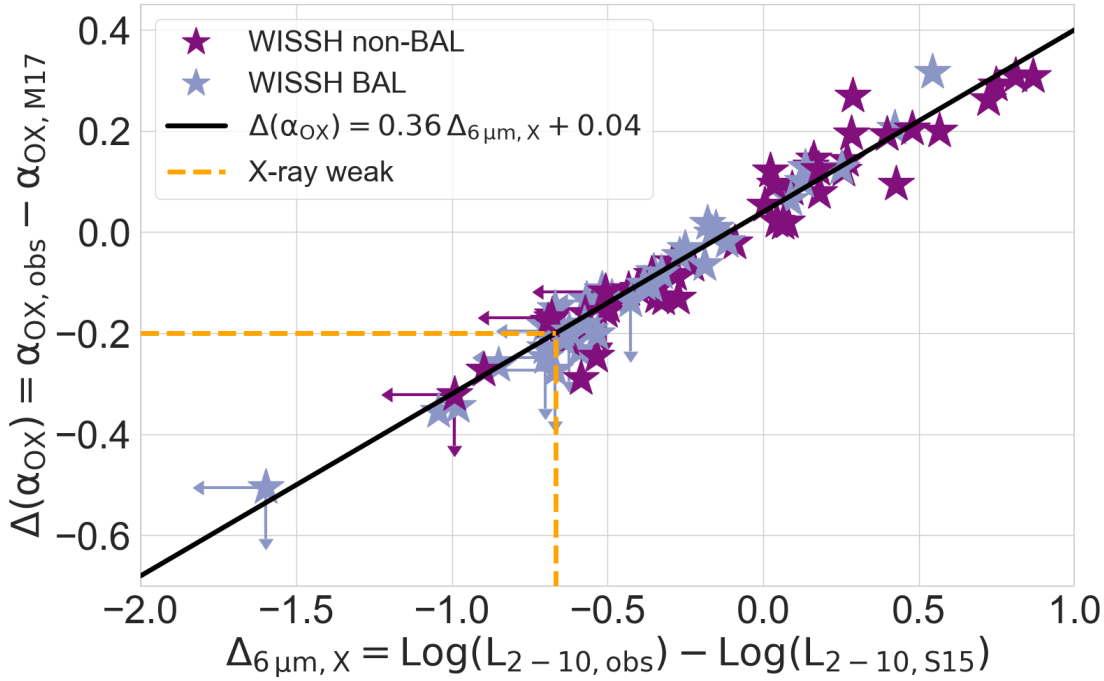

Figure 5.14: $\Delta(\alpha_{\rm OX})$ as a function of the hard X-ray luminosity offset of WISSH QSOs from the relation by S15 ($\Delta_{6\,\mu{\rm m,\,X}}$). Black solid line represents the best fit relation between the two quantities. WISSH BAL and non-BAL objects are indigo and purple stars, respectively. Orange horizontal line highlights the X-ray weak limit $\Delta(\alpha_{\rm OX}) < -0.2$, while the vertical one is its "translation" on the x-axis as $\Delta_{6\,\mu{\rm m,\,X}} < -0.65$.

ID	SDSS ID	$\mathrm{Log}(\mathrm{L}_{6\,\mu\mathrm{m}})$	ID	SDSS ID	$\mathrm{Log}(\mathrm{L}_{6\,\mu\mathrm{m}})$
WISSH01	J0045+1438	47.00 ± 0.01	WISSH44	J1201+1206	47.06 ± 0.03
WISSH02	J0124+0044	46.96 ± 0.05	WISSH45	J1204+3309	47.15 ± 0.03
WISSH03	J0125−1027	46.99 ± 0.03	WISSH46	J1210+1741	47.19 ± 0.03
WISSH04	J0209−0005	47.09 ± 0.01	WISSH47	J1215−0034	47.12 ± 0.02
WISSH05	J0216−0921	47.02 ± 0.03	WISSH48	J1219+4940	46.99 ± 0.01
WISSH06	J0414+0609	47.02 ± 0.01	WISSH49	J1220+1126	47.18 ± 0.01
WISSH07	J0735+2659	47.04 ± 0.01	WISSH50	J1236+6554	47.12 ± 0.02
WISSH08	J0745+4734	47.18 ± 0.02	WISSH51	J1237+0647	46.87 ± 0.02
WISSH09	J0747+2739	47.04 ± 0.06	WISSH52	J1245+0105	47.01 ± 0.02
WISSH10	J0801+5210	47.23 ± 0.02	WISSH53	J1249−0159	47.11 ± 0.03
WISSH11	J0818+0958	46.99 ± 0.05	WISSH54	J1250+2631	47.13 ± 0.01
WISSH12	J0846+2411	47.04 ± 0.12	WISSH55	J1250+2046	47.00 ± 0.03
WISSH13	J0900+4215	47.13 ± 0.02	WISSH56	J1305+0521	47.26 ± 0.03
WISSH14	J0904+1309	47.37 ± 0.01	WISSH57	J1310+4601	46.98 ± 0.01
WISSH15	J0928+5340	47.01 ± 0.07	WISSH58	J1326−0005	47.05 ± 0.02
WISSH16	J0941+3257	46.98 ± 0.04	WISSH59	J1328+5818	47.08 ± 0.02
WISSH17	J0947+1421	47.07 ± 0.02	WISSH60	J1333+1649	46.96 ± 0.01
WISSH18	J0950+4329	47.01 ± 0.01	WISSH61	J1421+4633	47.12 ± 0.02
WISSH19	J0958+2827	47.21 ± 0.02	WISSH62	J1422+4417	47.38 ± 0.02
WISSH20	J0959+1312	47.05 ± 0.06	WISSH63	J1426+6025	47.44 ± 0.01
WISSH21	J1013+5615	47.08 ± 0.03	WISSH64	J1433+0227	47.19 ± 0.06
WISSH22	J1014+4300	46.99 ± 0.02	WISSH65	J1441+0454	46.83 ± 0.01
WISSH23	J1015+0020	46.84 ± 0.21	WISSH66	J1447+1038	47.00 ± 0.03
WISSH24	J1020+0922	46.75 ± 0.08	WISSH67	J1451+1441	47.17 ± 0.02
WISSH25	J1025+2454	46.97 ± 0.01	WISSH68	J1506+5220	47.15 ± 0.03
WISSH26	J1026+0329	46.88 ± 0.09	WISSH69	J1513+0855	47.39 ± 0.01
WISSH27	J1027+3543	47.41 ± 0.01	WISSH70	J1521+5202	47.14 ± 0.01
WISSH28	J1048+4407	47.14 ± 0.06	WISSH71	J1538+0855	47.08 ± 0.03
WISSH29	J1051+3107	47.03 ± 0.08	WISSH72	J1544+4120	47.05 ± 0.02
WISSH30	J1057+4555	47.13 ± 0.05	WISSH73	J1549+1245	47.04 ± 0.01
WISSH31	J1103+1004	46.96 ± 0.04	WISSH74	J1554+1109	47.29 ± 0.01
WISSH32	J1106−1731	47.10 ± 0.01	WISSH75	J1555+1003	47.00 ± 0.03
WISSH33	J1106+6400	47.06 ± 0.01	WISSH76	J1559+4828	46.94 ± 0.02
WISSH34	J1110+1930	47.20 ± 0.01	WISSH77	J1559+1923	47.08 ± 0.05
WISSH35	J1110+4831	47.32 ± 0.01	WISSH78	J1621−0042	46.96 ± 0.05
WISSH36	J1110+4305	47.26 ± 0.03	WISSH79	J1633+3629	47.28 ± 0.02
WISSH37	J1111+1336	47.11 ± 0.03	WISSH80	J1639+2824	47.55 ± 0.02
WISSH38	J1122+1645	47.21 ± 0.01	WISSH81	J1650+2507	47.17 ± 0.02
WISSH39	J1130+0732	47.28 ± 0.01	WISSH82	J1701+6412	47.27 ± 0.01
WISSH40	J1157+2724	46.98 ± 0.01	WISSH83	J2123−0050	47.01 ± 0.01
WISSH41	J1159+1337	47.11 ± 0.05	WISSH84	J2238−0808	46.94 ± 0.03
WISSH42	J1200+3126	47.09 ± 0.02	WISSH85	J2346−0016	46.91 ± 0.04
WISSH43	J1201+0116	47.13 ± 0.03			

Table 5.3: The WISSH sample: ID, SDSS ID and luminosity at 6 μm (in units of $\mathrm{Log}(\lambda \mathrm{L}/\mathrm{erg\,s^{-1}})$). Errors are reported at 1σ confidence level.

6

Conclusion

AGN feedback is a fundamental piece in the puzzle of the AGN - galaxy co-evolution framework. Under this perspective, the WISSH project aims at investigating the phenomenon in its extreme manifestations, observing the most luminous quasars in the Universe in their most active epoch, the cosmic noon ($z \approx 2-4$). To properly study feedback in all of its aspects, a multi-wavelength study is performed, making use of archival and proprietary data from radio to X-ray band. Figure 6.1 displays the spectral coverage of several telescopes used to acquire data of an ideal WISSH quasar at $z = 3.5$.

X-ray analysis can be summarised in three main results:

- X-ray weakness;
- Spectral index (Γ) relation with $\Delta(\alpha_{OX})$ and λ_{Edd};
- WISSH blue sources found in the forbidden region of $\lambda_{Edd} - N_H$ plane.

X-ray weakness

WISSH QSOs exhibit anomalous distribution in the $L_{bol} - k_{bol}$ and $L_{2500} - \alpha_{OX}$ planes. Despite broadly following expected trends (i.e. D20 and M17, respectively), their vertical dispersion is large: a small L_{bol} or L_{2500} range corresponds to a wide bolometric correction and X-ray - to - optical index distribution (Figures 5.4 and 5.7). The two parameters represent the X-ray luminosity relative strength compared to total and UV ones. Thus, the increase (decrease) of k_{bol} (α_{OX}) means that L_{2-10} becomes weaker in hyper-luminous quasars, in accordance with the slopes found for lower-luminosity samples. Accretion disk - corona coupling in WISSH AGN is therefore consistent with that in standard QSOs. However, the vertical spread hints towards additional phenomena occurring in the AD - corona system.

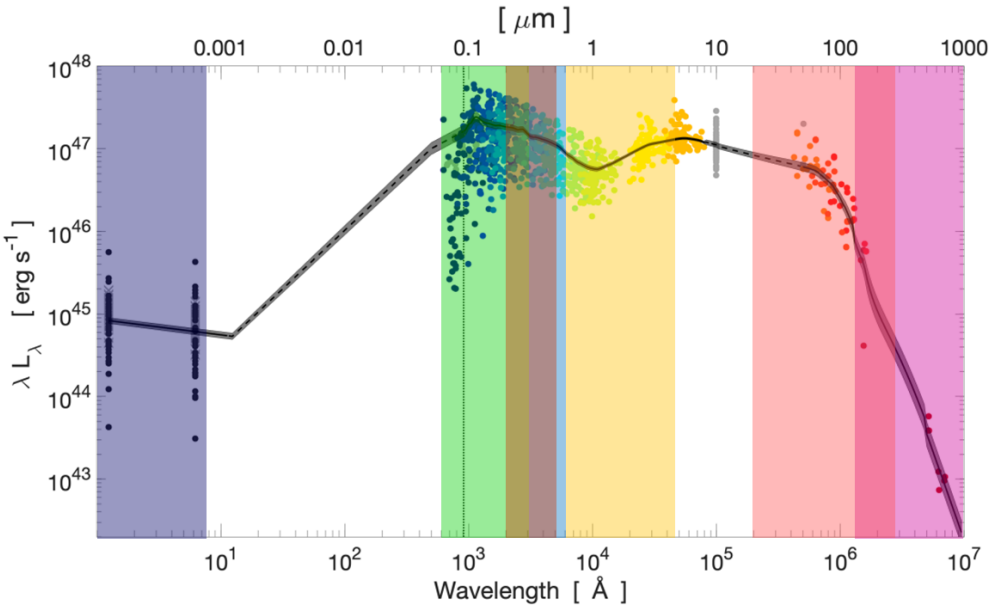

Figure 6.1: Mean SED derived for the WISSH sample from Saccheo et al. 2023. The shaded area gives the 68 % confidence interval. The colored circles represent available data points, color-coded according to the filter in which they were observed. The grey crosses indicate X-ray luminosities reconstructed from the α_{OX} relationship. Overlaying rectangles highlight spectral coverage of several telescopes used to acquire WISSH data. From left to right: Chandra/XMM-Newton in blue; SDSS facilities in green; VLT/SINFONI in brown; LBT/LUCI in light blue; WISE in yellow; Herschel in red; ALMA/VLT in pink.

Once the offset $\Delta(\alpha_{OX})$ of measured X-ray - to - optical index from the expected value (based on M17 best fit relation) is defined, the threshold $\Delta(\alpha_{OX}) < -0.2$ (Luo et al. 2015) is adopted to identify X-ray weak quasars. About 22 % of WISSH QSOs fall below the threshold: in particular, $\sim$ 30 % of BAL and $\sim$ 16 % of non-BAL sources (Figure 5.8).

Further investigation is needed to draw robust conclusions, due also to the small number of sources (85). Being them quite rare, future wide-field surveys are advisable. In any case, such X-ray weakness compared to the UV emission seems to be fundamental to avoid nuclear gas over-ionisation, which would prevent radiation pressure from producing radiative-driven winds (e.g. Leighly 2004, Proga 2003, Proga 2007).

Γ dependences

The X-ray spectral slope is a degenerate parameter with N_H, i.e. a strong absorption can cause Γ flattening. Figure 5.9 shows that the inclusion of absorption in the spectral modelling steepens Γ, and it occurs, in particular, in X-ray weaker sources. Indeed, besides flattening the X-ray spectral index, N_H also causes $L_{2\,keV}$,

thus $\Delta(\alpha_{OX})$, weakening. Gas shielding the corona would translate into harder X-ray spectrum, as is indeed visible in Figure 5.9. Some authors (e.g. Proga et al. 2004, Proga 2005, Zappacosta et al. 2020, Nomura et al. 2020) suggest outflows themselves or failed winds to be responsible for coronal destruction or obscuration. However, when including the intrinsic column density, no correlation is found between $\Delta(\alpha_{OX})$ and Γ. Additional non-revealed obscuration may be present in X-ray weaker sources. Moreover, Laurenti et al. 2022 notice that it is not possible to rule out the presence of highly-ionised gas cloud with large N_H and small covering factor. This medium would scatter a large amount of radiation, causing a decrease of the X-ray flux without altering significantly the spectral shape.

The X-ray spectral index has been claimed to be a proxy for the Eddington ratio, as a positive relation seems to emerge between the two quantities in previous works (e.g. Liu et al. 2021, Brightman et al. 2013, Trakhtenbrot et al. 2017). Thus, Γ is also studied as a function of λ_{Edd}, for the 19/85 sources with ≥ 20 counts and an available Hβ-derived M_{BH} estimate. Nonetheless, it is evident from Figure 5.11 that data around $\lambda_{Edd} \approx 1$ are highly dispersed and no correlation can be found. Indeed, a non-negligible fraction ($\sim 28\,\%$) of WISSH sources with ≥ 20 counts exhibits flat ($\Gamma \approx 1.2 - 1.7$) spectral index, at odds with the expectations based on previously published $\lambda_{Edd} - \Gamma$ relations (e.g. Shemmer et al. 2008, Risaliti et al. 2009, Brightman et al. 2013), which predict $\Gamma \approx 2 - 2.3$ for AGN with $\lambda_{Edd} \approx 1$.

However, the wide range of spectral index values may be a further indication of a possible change in the properties of the accretion disk - corona system.

Blue quasars in the "forbidden region"

The theoretical AGN duty cycle can be drawn in the $\lambda_{Edd} - N_H$ plane. Consequently to a wet merger, quasars face an obscured-accretion phase, which triggers intense feedback processes, eventually sweeping up most of nuclear gas. Then, sources enter an unobscured regime during which sporadic accretion and star formation occur, evolving towards a passive red galaxy phase. The whole duty cycle is better outlined in Figure 2.4. High-λ_{Edd}/high-N_H conditions correspond to a "forbidden region" in the plane. It was introduced by Fabian et al. 2008 as a transitional state in AGN life, during which the nuclear source, previously obscured, is set free from absorbing gas thanks to feedback outflows.

Dust-obscured red QSOs, thought to be experiencing the obscured-accretion phase of AGN duty cycle, are expected to occupy the forbidden area in the $\lambda_{Edd} - \Gamma$ plane. 2/3 WISSH red sources (i.e. characterised by $E(B-V) > 0.15$) with available N_H and Hβ-derived M_{BH} estimate, are likely located in the forbidden region.

In Figure 5.12, the red quasars are surrounded by a circle: one well constrained source and one with an extreme N_H upper limit are visible in the forbidden region.

All of the five WISSH blue sources with statistically significant intrinsic column density also occupy the forbidden region, as well as most of the WISSH blue quasars with N_H upper limit only. This result is not completely unexpected, as previous publications (e.g. Ballo et al. 2014) report of blue objects in the $\lambda_{Edd} - N_H$ plane forbidden area. Different nature of obscuring material in red and blue QSOs is suggested. Dust-rich large-scale gas would originate the former, while dust-free small-scale medium would be responsible for the latter (e.g. Maiolino et al. 2001). Nonetheless, deeper X-ray observations and larger samples are needed to draw any firm conclusion.

6.1 Future perspectives

Future works will focus on three main research paths:

- Combined study of X-ray and radio emission (Bruni et al. in prep.);
- Link WISSH QSOs at the cosmic noon with $z \geq 6$ quasars (e.g. the HYPERION sample - Zappacosta et al. 2023);
- Deeper X-ray observations of WISSH sources.

X-ray - radio connection

The radio band is the last missing piece of WISSH puzzle for a multi-wavelength coverage. It may originate from synchrotron radiation emerging from small-scale jets or shock regions, which can be produced by the interaction of nuclear outflows with the surrounding ISM. Jet production and winds activity are thought to be related to BH accretion and the innermost regions of AGN, thus further investigation of radio emission correlation with nuclear processes is needed. As the X-ray emission component traces such phenomena, studying the X-ray - radio connection could further knowledge on the production of the latter and its relation with accretion.

In order to pursue this objective, Very Large Array (VLA) data are collected for the whole WISSH sample since 2022 (Bruni et al. 2023). At 3 GHz, at an RMS of $\sim$ 10 μJy/beam, $\sim$ 80 % detection rate is obtained. Moreover, three sources exhibit extended symmetric morphology, corresponding to about 30 kpc in projected linear size. This result opens the question on the possible presence of radio galaxies in WISSH sample.

HYPer-luminous quasars at the Epoch of ReionizatION - HYPERION

So far in the present thesis, WISSH sources have been compared to similar- or lower-redshift ones. However, an on-going observational campaign is collecting XMM-Newton data of HYPer-luminous quasars at the Epoch of ReionizatION (HYPERION - $L_{bol} \approx 10^{46} - 10^{48}$ erg s^{-1}). The 18 objects have been selected for having $M_{BH} \approx 10^8 - 10^{10}$ $M_\odot$ at $z > 6$, therefore requiring initial seed BH mass of $M_{BH}^{seed} > 1000\,M_\odot$ accreting via continuous exponential growth at the Eddington rate. They will be targeted by the 2.4 Ms XMM-Newton Multi-Year Heritage program over three years.

Zappacosta et al. 2023 present results of the first year of the program: X-ray data of ten new sources, along with two archival ones. Several peculiar properties emerge:

- Steep X-ray spectral slope. Large majority of HYPERION sources exhibits $\Gamma \geq 2.3$, with an average value of $\Gamma \approx 2.4 \pm 0.1$ which is not consistent with L_{bol}- and λ_{Edd}-analogs at $z < 6$. Lower-redshift sources typically show $\Gamma = 2$, which is flatter than HYPERION values at $> 4\sigma$ level. For a further comparison, WISSH QSOs mean X-ray spectral index is 1.89 ± 0.04.

  Such a discrepancy is interpreted by Zappacosta et al. 2023 as an evolutionary effect, maybe due to extremely rapid SMBH mass assembly undergone by these quasars. However, a standard $\Gamma = 1.9$ power-law with high-energy cut-off at particularly low energies cannot be excluded by the available low statistic;

- No absorption ($N_H \leq 10^{22}$ cm^{-2}) is derived in HYPERION QSOs, contrarily to $\sim$ 24 % of WISSH QSOs exhibiting a moderate/strong absorption ($N_H \geq 10^{22}$ cm^{-2});

- Higher 2 keV luminosity, resulting from similar hard X-ray luminosity but steeper spectral slope compared to lower-z samples. This result translates into the flatter α_{OX} visible in Figure 6.2, where almost all HYPERION QSOs (red stars) fall above the M17 relation. Thus, the X-ray weakness property characterising the WISSH sample (Figures 5.7 and 5.8) does not seem to be present. HYPERION data result in an average $\Delta(\alpha_{OX}) = 0.08$, compared to $\Delta(\alpha_{OX}) = -0.05$ for WISSH sources.

Moreover, Zappacosta et al. 2023 study the $L_{bol} - k_{bol}$ plane, where HYPERION QSOs fall within 1σ spread of the D20 relation, as evident in Figure 6.3.

Such distribution differs from that of WISSH QSOs, once the sample is completed (Figures 5.4 and 5.5).

A detailed comparison of HYPERION quasars with lower-luminosity samples will provide information on possible cosmological evolution of X-ray properties of these hyper-luminous sources and will shed further light on the accretion processes.

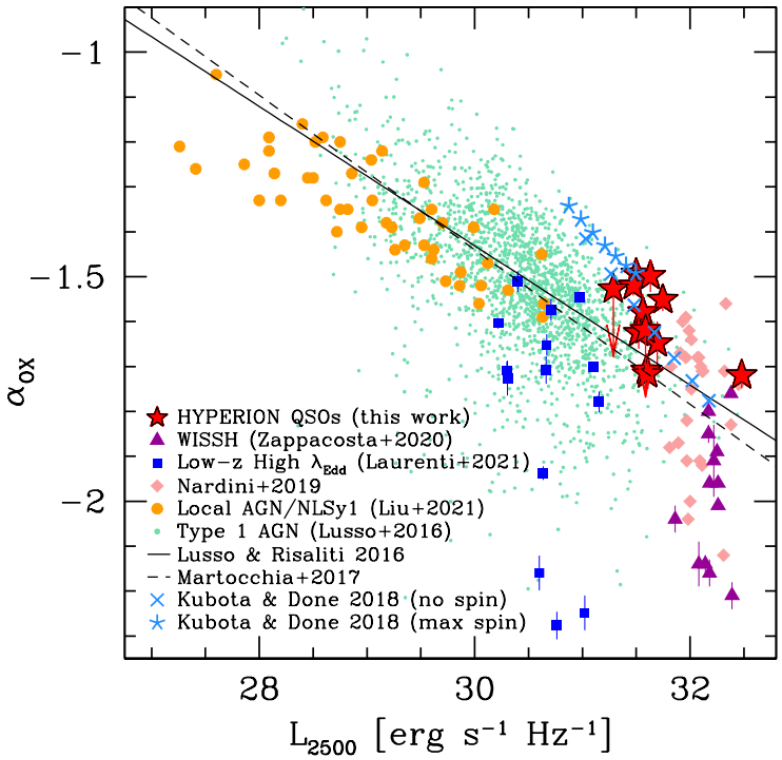

Figure 6.2: From Zappacosta et al. 2023 - α_{OX} vs. L_{2500} for a compilation of AGN catalogs. Red stars are the HYPERION QSOs. Green four-pointed stars are other $z > 6$ QSOs, detected with $\gtrsim 30$ net-counts, from the X-ray spectral analysis performed by Vito et al. 2019 and not included in the HYPERION sample. Quasars at the cosmic noon ($z = 2 - 4$) are reported in purple triangles (the WISSH QSOs from Zappacosta et al. 2020) and pink diamond (Nardini et al. 2019, Trefoloni et al. 2023). Local high-λ_{Edd} QSOs from Laurenti et al. 2022 and local AGN/NLSy1 (Liu et al. 2021) are reported respectively as blue square and yellow circles. Green dots are detected AGN with signal-to-noise ratio SNR > 5 from Lusso et al. 2016. Upper limits for the HYPERION QSOs are estimated assuming a power-law with fixed $\Gamma = 2.4$. Dashed line is the linear fit from M17 while solid line refers to the best-fit relation from Lusso et al. 2016 and for the sub-sample with SNR > 5, $E(B - V) \geq 0.1$ and $1.6 \leq \Gamma_{1-5} \leq 2.8$ (Γ_{1-5} being the photon index estimated between the luminosities at 1 keV and 5 keV). Light blue crosses and asterisks present the values predicted by the `QSOSED` model (Kubota et al. 2018) assuming average HYPERION parameters and spin a = 0 and a = 1, respectively. They are reported from top-left to bottom-right from $\mathrm{Log}(\dot{m}) = -1$ to $\mathrm{Log}(\dot{m}) = 0.2$ in steps of $\Delta(\mathrm{Log}(\dot{m})) = 0.2$.

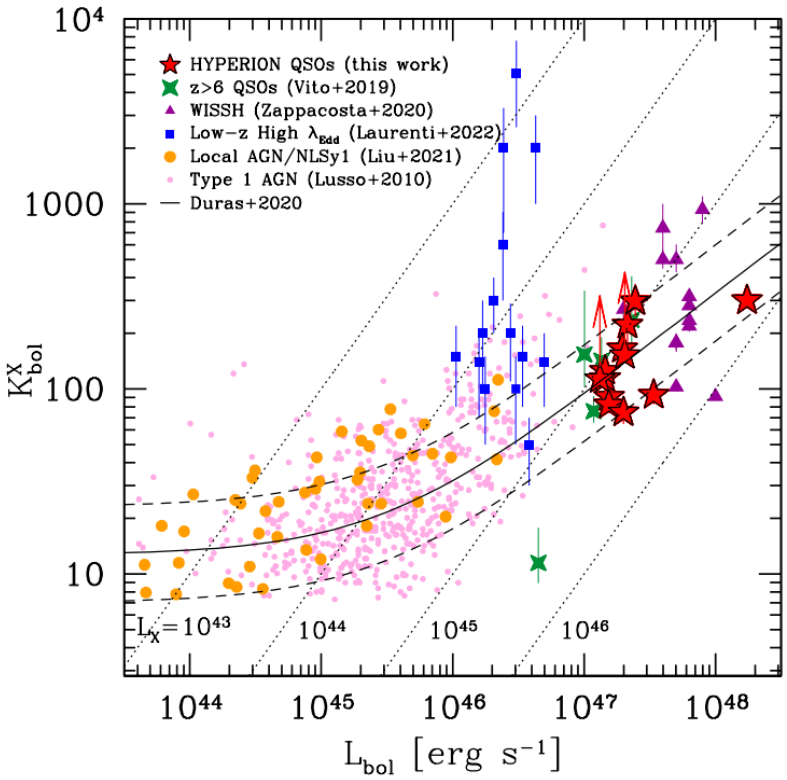

Figure 6.3: From Zappacosta et al. 2023 - k_{bol} vs. L_{bol} for a compilation of broad-line mostly high-z QSOs and local AGN. Symbols are the same as in Figure 6.2, except for COSMOS Type 1 AGN (pink dots) from Lusso et al. 2010. Solid and dashed black lines represent the fitting relation reported in D20 and its 1σ spread. Dotted lines report fixed value of $2-10$ keV luminosity in units of erg s^{-1} in the k_{bol} vs. L_{bol} plane.

Deeper X-ray observations

The available X-ray data for WISSH QSOs result in 8/85 undetected sources, while detections range from 1 up to $\sim$ 2340 counts (in $0.3-7$ keV and $0.3-10$ keV energy range for Chandra and XMM-Newton, respectively). The median number of photons is 16, meaning that the majority of the quasars has too few counts to perform a solid spectral analysis. Then, for most of the WISSH sample Γ is not available, and N_H can be derived for $\sim 65\,\%$ of it (for 16/55 from HR$-N_H$ relation and not spectral analysis).

To accurately study parameters space in hyper-luminous quasars and possibly relate various spatial scales and frequency bands, deeper X-ray observations are therefore needed. For example, higher photon statistics could allow thick absorbers in currently undetected sources to be revealed, possibly indicating the presence of outflows. Indeed, some authors (e.g. Proga et al. 2004, Proga 2005, Zappacosta et al. 2020, Nomura et al. 2020) suggest outflows themselves or failed winds to be responsible for coronal obscuration. This scenario is also coherent with the results

for higher-counts sources in the $\lambda_{\rm Edd} - {\rm N_H}$ plane, where most of WISSH QSOs occupy the blowout region at high $\rm N_H$ (see Section 5.4).

As highlighted by M17, ESA next X-ray observatory *Athena* will provide higher sensibility and spectral resolution than any telescope so far. Then, relatively short exposures will supply with hundreds of counts, and features corresponding to UFOs will emerge in X-ray spectra. Moreover, they envisage a program to investigate the link between UFOs and their outflow manifestation, based on several theoretical models (e.g. King 2010, Faucher-Giguère and Quataert 2012 Zubovas and King 2012) proposing that the kpc-scale outflows routinely observed in AGN are triggered by relativistic UFOs originating in the nuclear regions.

A

Data analysis results

The parameters derived from data analysis (Chapter 5), along with their uncertainties, are presented in Table A.1. Errors are reported at 1σ confidence level for k_{bol} and α_{OX}. λ_{Edd} spread is derived from bolometric luminosity 1σ error and 0.3 dex systematic uncertainty on M_{BH}.

Table A.1: X-ray WISSH sample: data analysis results. (1) ID; (2) SDSS ID; (3) bolometric luminosity (in units of $\mathrm{Log(L/erg\,s^{-1})}$) from Saccheo et al. 2023; (4) bolometric correction; (5) X-ray - to - optical index; (6) $\Delta(\alpha_{\mathrm{OX}}) = \alpha_{\mathrm{OX,\,exp}} - \alpha_{\mathrm{OX,\,M17}}$; (7) Eddington ratio for available Hβ-derived black hole masses. Errors and upper (lower) limits are reported at 1σ confidence level for $\mathrm{k_{bol}}$ and α_{OX}, while λ_{Edd} spread is derived from bolometric luminosity 1σ error and 0.3 dex systematic uncertainty on $\mathrm{M_{BH}}$.

ID	SDSS ID	$\mathrm{L_{bol}}$	$\mathrm{k_{bol}}$	α_{OX}	$\Delta(\alpha_{\mathrm{OX}})$	λ_{Edd}
(1)	(2)	(3)	(4)	(5)	(6)	(7)
WISSH01	J0045+1438	47.53 ± 0.13	1380 ± 481	-2.14 ± 0.04	-0.36	1.79 ± 1.89
WISSH02	J0124+0044	47.55 ± 0.06	134 ± 19	-1.72 ± 0.05	0.05	–
WISSH03	J0125−1027	47.48 ± 0.08	79 ± 16	-1.63 ± 0.04	0.13	–
WISSH04	J0209−0005	47.67 ± 0.06	295 ± 43	-1.93 ± 0.09	-0.13	1.09 ± 1.1
WISSH05	J0216−0921	47.53 ± 0.06	275 ± 166	-1.86 ± 0.08	-0.08	–
WISSH06	J0414+0609	47.59 ± 0.07	1348 ± 1363	-2.14 ± 0.12	-0.35	0.49 ± 0.5
WISSH07	J0735+2659	47.66 ± 0.05	338 ± 41	-1.94 ± 0.11	-0.13	2.42 ± 2.43
WISSH08	J0745+4734	47.96 ± 0.15	38 ± 15	-1.56 ± 0.38	0.31	0.46 ± 0.5
WISSH09	J0747+2739	47.5 ± 0.06	257 ± 38	-1.89 ± 0.13	-0.11	–
WISSH10	J0801+5210	47.81 ± 0.05	316 ± 38	-1.89 ± 0.18	-0.07	0.83 ± 0.83
WISSH11	J0818+0958	47.48 ± 0.06	257 ± 155	-1.86 ± 0.08	-0.08	0.31 ± 0.31
WISSH12	J0846+2411	47.27 ± 0.09	> 316	< -1.92	< -0.17	–
WISSH13	J0900+4215	47.89 ± 0.08	44 ± 9	-1.55 ± 0.14	0.29	2.93 ± 2.98
WISSH14	J0904+1309	47.85 ± 0.08	93 ± 18	-1.63 ± 0.01	0.19	–
WISSH15	J0928+5340	47.47 ± 0.12	> 288	< -1.94	< -0.14	–

Continues in next page

ID	SDSS ID	L_{bol}	k_{bol}	α_{OX}	$\Delta(\alpha_{OX})$	λ_{Edd}
(1)	(2)	(3)	(4)	(5)	(6)	(7)
WISSH16	J0941+3257	47.61 ± 0.07	295 ± 51	-1.88 ± 0.06	-0.08	0.51 ± 0.52
WISSH17	J0947+1421	47.67 ± 0.05	120 ± 14	-1.71 ± 0.02	0.1	–
WISSH18	J0950+4329	47.66 ± 0.07	31 ± 5	-1.54 ± 0.1	0.26	2.27 ± 2.29
WISSH19	J0958+2827	47.59 ± 0.1	912 ± 236	2.07 ± 0.03	-0.27	0.88 ± 0.91
WISSH20	J0959+1312	47.81 ± 0.1	64 ± 16	-1.5 ± 0.24	0.32	–
WISSH21	J1013+5615	47.61 ± 0.07	257 ± 44	-1.83 ± 0.06	-0.05	0.37 ± 0.38
WISSH22	J1014+4300	47.81 ± 0.13	218 ± 76	-1.83 ± 0.15	0.02	0.61 ± 0.64
WISSH23	J1015+0020	47.29 ± 0.07	58 ± 10	-1.59 ± 0.04	0.14	–
WISSH24	J1020+0922	47.26 ± 0.08	223 ± 162	-1.86 ± 0.09	-0.11	–
WISSH25	J1025+2454	47.29 ± 0.51	> 2951	< -2.24	< -0.51	–
WISSH26	J1026+0329	47.38 ± 0.14	> 323	< -1.86	< -0.12	–
WISSH27	J1027+3543	47.99 ± 0.07	158 ± 27	-1.73 ± 0.01	0.12	0.56 ± 0.57
WISSH28	J1048+4407	47.74 ± 0.11	630 ± 411	-2.02 ± 0.08	-0.19	–
WISSH29	J1051+3107	47.53 ± 0.08	371 ± 75	-1.91 ± 0.07	-0.13	–
WISSH30	J1057+4555	47.89 ± 0.08	138 ± 27	-1.73 ± 1.12	0.12	–
WISSH31	J1103+1004	47.51 ± 0.06	> 524	< -1.97	< -0.2	–
WISSH32	J1106−1731	47.42 ± 0.15	416 ± 274	-1.92 ± 0.07	-0.16	–
WISSH33	J1106+6400	47.71 ± 0.13	95 ± 33	-1.69 ± 0.48	0.14	0.41 ± 0.43
WISSH34	J1110+1930	47.75 ± 0.4	407 ± 615	-1.92 ± 0.04	-0.1	0.43 ± 0.78
WISSH35	J1110+4831	47.84 ± 0.06	269 ± 39	-1.83 ± 0.27	-0.0	–

Continues in next page

ID	SDSS ID	L_{bol}	k_{bol}	α_{OX}	$\Delta(\alpha_{OX})$	λ_{Edd}
(1)	(2)	(3)	(4)	(5)	(6)	(7)
WISSH36	J1110+4305	47.96 ± 0.16	39 ± 17	-1.55 ± 0.37	0.31	–
WISSH37	J1111+1336	47.72 ± 0.05	213 ± 26	-1.84 ± 0.18	-0.02	0.49 ± 0.49
WISSH38	J1122+1645	47.61 ± 0.13	446 ± 304	-1.92 ± 0.08	-0.13	–
WISSH39	J1130+0732	47.7 ± 0.15	52 ± 21	-1.59 ± 0.2	0.21	–
WISSH40	J1157+2724	47.58 ± 0.07	489 ± 85	-1.99 ± 0.24	-0.2	1.16 ± 1.17
WISSH41	J1159+1337	47.75 ± 0.06	407 ± 306	-1.96 ± 0.09	-0.13	–
WISSH42	J1200+3126	47.79 ± 0.15	173 ± 71	-1.82 ± 0.03	0.02	–
WISSH43	J1201+0116	47.64 ± 0.07	691 ± 120	-1.98 ± 0.96	-0.18	1.08 ± 1.09
WISSH44	J1201+1206	47.75 ± 0.09	128 ± 29	-1.74 ± 0.04	0.08	0.69 ± 0.7
WISSH45	J1204+3309	47.76 ± 0.1	> 912	< -2.07	< -0.25	0.77 ± 0.8
WISSH46	J1210+1741	47.82 ± 0.15	> 933	< -2.14	< -0.27	–
WISSH47	J1215−0034	47.64 ± 0.06	218 ± 32	-1.86 ± 0.26	-0.06	–
WISSH48	J1219+4940	47.62 ± 0.07	125 ± 22	-1.72 ± 0.08	0.09	–
WISSH49	J1220+1126	47.81 ± 0.07	181 ± 31	-1.73 ± 0.49	0.09	5.12 ± 5.18
WISSH50	J1236+6554	47.68 ± 0.06	147 ± 21	-1.69 ± 0.1	0.12	0.88 ± 0.89
WISSH51	J1237+0647	47.4 ± 0.08	151 ± 30	-1.74 ± 0.04	0.01	–
WISSH52	J1245+0105	47.42 ± 0.16	316 ± 140	-1.87 ± 0.05	-0.11	–
WISSH53	J1249−0159	47.59 ± 0.07	346 ± 262	-1.91 ± 0.09	-0.11	0.31 ± 0.31
WISSH54	J1250+2631	47.86 ± 0.2	77 ± 45	-1.65 ± 0.07	0.2	3.03 ± 3.49
WISSH55	J1250+2046	47.45 ± 0.12	524 ± 548	-1.94 ± 0.12	-0.18	–

Continues in next page

ID	SDSS ID	L_{bol}	k_{bol}	α_{OX}	$\Delta(\alpha_{OX})$	λ_{Edd}
(1)	(2)	(3)	(4)	(5)	(6)	(7)
WISSH56	J1305+0521	47.53 ± 0.15	144 ± 59	-1.77 ± 0.03	0.02	–
WISSH57	J1310+4601	47.59 ± 0.09	75 ± 17	-1.52 ± 0.11	0.27	0.77 ± 0.79
WISSH58	J1326−0005	47.67 ± 0.2	213 ± 125	-1.83 ± 0.22	−0.02	1.77 ± 2.04
WISSH59	J1328+5818	47.37 ± 0.2	371 ± 217	-1.9 ± 0.04	−0.15	–
WISSH60	J1333+1649	47.68 ± 0.12	69 ± 22	-1.73 ± 0.08	0.09	–
WISSH61	J1421+4633	47.68 ± 0.05	537 ± 65	-2.05 ± 0.16	−0.25	0.61 ± 0.61
WISSH62	J1422+4417	47.96 ± 0.09	1000 ± 230	-2.08 ± 0.06	−0.21	1.65 ± 1.68
WISSH63	J1426+6025	48.04 ± 0.06	223 ± 33	-1.85 ± 0.19	0.02	0.35 ± 0.35
WISSH64	J1433+0227	47.57 ± 0.07	354 ± 216	-1.96 ± 0.08	−0.15	1.55 ± 1.57
WISSH65	J1441+0454	47.37 ± 0.1	389 ± 100	-1.91 ± 0.77	−0.16	–
WISSH66	J1447+1038	47.55 ± 0.08	301 ± 186	-1.9 ± 0.08	−0.1	–
WISSH67	J1451+1441	47.66 ± 0.12	478 ± 318	-1.94 ± 0.08	−0.14	0.14 ± 0.14
WISSH68	J1506+5220	47.66 ± 0.11	1023 ± 736	-2.05 ± 0.08	−0.26	–
WISSH69	J1513+0855	47.86 ± 0.09	131 ± 30	-1.71 ± 0.03	0.13	1.31 ± 1.33
WISSH70	J1521+5202	47.85 ± 0.09	870 ± 200	-2.16 ± 0.34	−0.29	0.56 ± 0.58
WISSH71	J1538+0855	47.83 ± 0.07	891 ± 641	-2.07 ± 0.09	−0.23	0.98 ± 0.99
WISSH72	J1544+4120	47.57 ± 0.09	489 ± 360	-1.98 ± 0.09	−0.18	0.13 ± 0.13
WISSH73	J1549+1245	47.74 ± 0.13	346 ± 120	-1.86 ± 0.2	−0.03	0.35 ± 0.37
WISSH74	J1554+1109	47.8 ± 0.26	> 1698	< -2.14	< -0.32	–
WISSH75	J1555+1003	47.41 ± 0.14	478 ± 509	-2.02 ± 0.12	−0.23	–

Continues in next page

ID	SDSS ID	L_{bol}	k_{bol}	α_{OX}	$\Delta(\alpha_{OX})$	λ_{Edd}
(1)	(2)	(3)	(4)	(5)	(6)	(7)
WISSH76	J1559+4828	47.5 ± 0.05	398 ± 297	-1.94 ± 0.09	-0.16	0.36 ± 0.36
WISSH77	J1559+1923	47.64 ± 0.09	630 ± 644	-2.02 ± 0.12	-0.21	–
WISSH78	J1621−0042	47.78 ± 0.09	63 ± 14	-1.63 ± 0.66	0.2	0.7 ± 0.72
WISSH79	J1633+3629	47.8 ± 0.08	371 ± 75	-1.91 ± 0.06	-0.08	0.4 ± 0.41
WISSH80	J1639+2824	48.07 ± 0.07	204 ± 35	-1.81 ± 0.06	0.06	1.1 ± 1.11
WISSH81	J1650+2507	47.62 ± 0.14	630 ± 501	-1.98 ± 0.09	-0.19	–
WISSH82	J1701+6412	47.96 ± 0.13	102 ± 35	-1.67 ± 0.08	0.19	2.78 ± 2.94
WISSH83	J2123−0050	47.69 ± 0.06	100 ± 14	-1.69 ± 0.01	0.13	1.0 ± 1.0
WISSH84	J2238−0808	47.47 ± 0.06	512 ± 366	-1.96 ± 0.09	-0.19	0.21 ± 0.21
WISSH85	J2346−0016	47.53 ± 0.05	269 ± 160	-1.82 ± 0.08	-0.06	0.63 ± 0.63

B

Multiple observations

24/85 WISSH QSOs have multiple observations with either Chandra and/or XMM-Newton (as mentioned in Section 4.2 - Figure 4.3), which have been performed during different Cycles of observation. Nuclear emission variations between the two data collections, either intrinsic or due to changes in the absorbing material, are possible. Such variability could, for example, justify the observed X-ray weakness in terms of a transitional obscured state.

Figure B.1 shows the comparison of the observed $0.5 - 10$ keV flux *(top)* and intrinsic $2 - 10$ keV luminosity *(bottom)* derived from data collected at different epochs, which have been analysed as in Section 4.2. It is evident that both quantities are broadly consistent between the two observations, with some exceptions. In particular, J1701+6412 (z = 2.753) and J2123−0050 (z = 2.282), indicated in the Figure, exhibit $F_{0.5-10}$ and L_{2-10} that are inconsistent at $> 3\sigma$ level between the two observations.

The present analysis suggests that WISSH QSOs are typically not strongly variable objects in the X-ray band, thus supporting the simplification of considering data from only one observation per source.

If ≥ 6 counts are detected in both observations of a quasar, the two derived N_H can also be compared. Figure B.2 shows two WISSH sources in which a variation seems to occur in terms of the intrinsic column density. The rest-frame time interval Δt spanning between the two observations is also reported.

In J1513+0855 (z = 2.8883), spectral and HR analysis are performed for *Obs1* (i.e. the observation resulting in the higher number of counts, presented in Section 4.2) and *Obs2*, respectively. N_H of the latter observation is derived through the hardness ratio assuming $\Gamma = 1.8$ (Section 4.2.3), and resulting in the reduced obscuration. In J1521+5202 (z = 2.218), N_H is derived from spectral analysis for both the observations. Γ is modelled in *Obs1*, while fixed at $\Gamma = 1.8$ in *Obs2*.

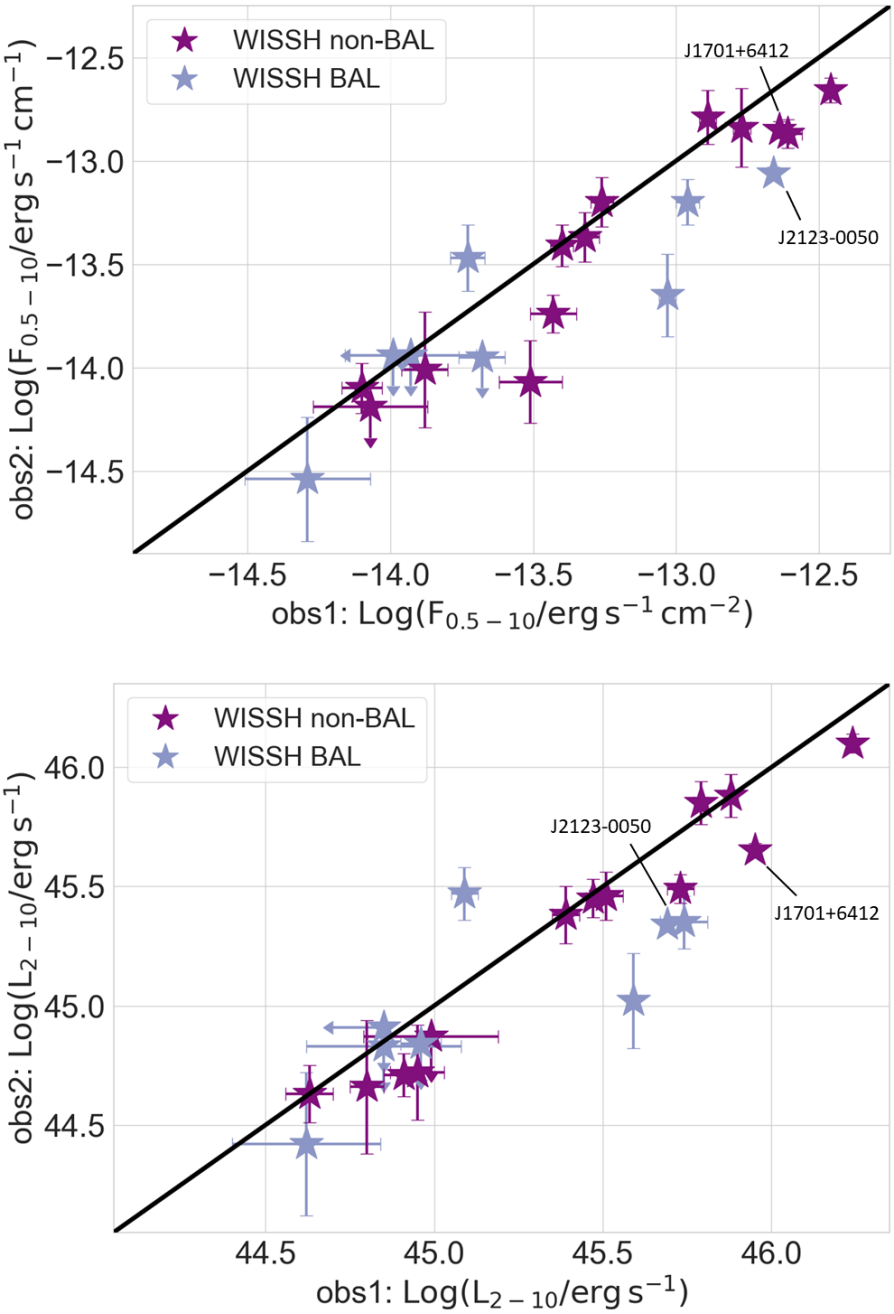

Figure B.1: Observed 0.5 − 10 keV flux *(top)* and intrinsic 2 − 10 keV luminosity *(bottom)* for the sources with multiple observations. x-axis reports the "primary" results (i.e. those derived from the observation with the highest number of counts, presented in Section 4.2). BAL and non-BAL quasars are shown as indigo and purple stars, respectively. Uncertainties and upper limits are reported at 1σ and 90 % confidence level, respectively. SDSS IDs of the quasars whose $F_{0.5-10}$ and L_{2-10} are inconsistent at $> 3\sigma$ level between the two observations are indicated.

Thus, in both sources, changes in *Obs2* X-ray spectral indix (which is a degenerate parameter with N_H) may account for the displayed incoherence.

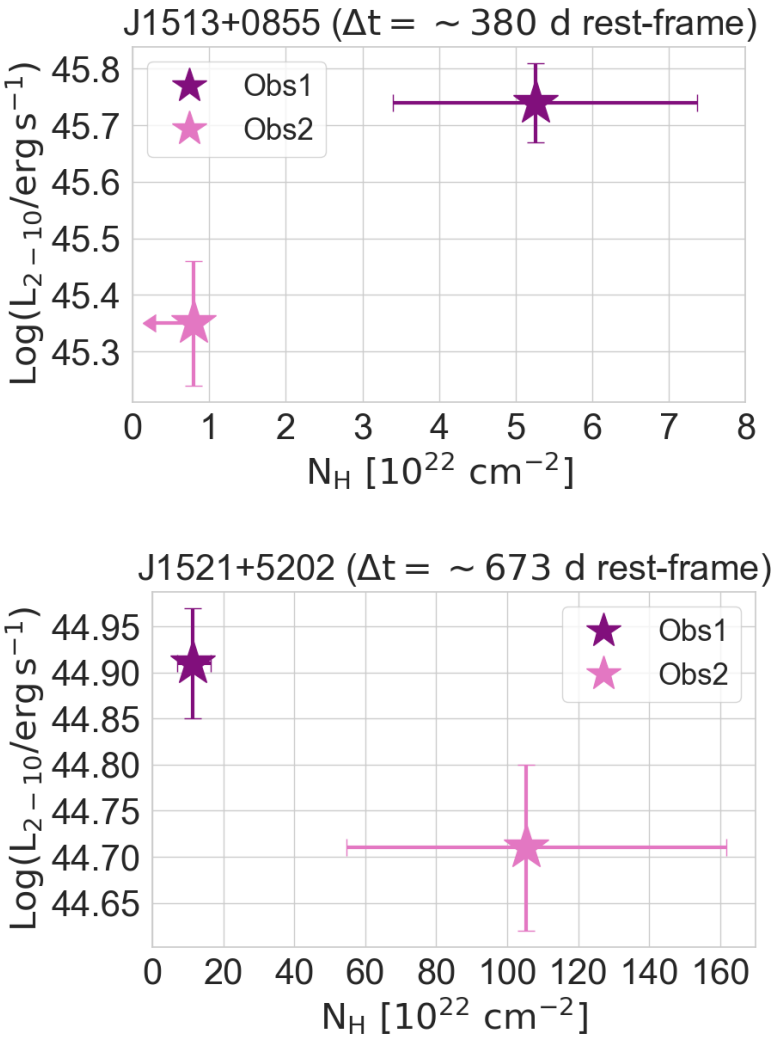

Figure B.2: Intrinsic $2-10$ keV luminosity (in units of $\mathrm{Log(L/erg\,s^{-1})}$) as a function of the intrinsic column density (in units of 10^{22} cm^{-2}) for two WISSH sources with multiple observations. In both exposures, the quasars are detected with ≥ 6 counts. Purple stars represent the the "primary" observation, i.e. that with the highest number of counts, which is presented in Section 4.2. Both uncertainties and upper limits are reported at 1σ confidence level. Δt is the rest-frame time interval spanning between the two observations.

C

An interesting source

Among the WISSH QSOs for which spectral analysis is performed (i.e. detected with ≥ 20 counts), J1310+4601 (z = 2.1423) exhibits the steepest X-ray spectral index. Indeed, the measured $\Gamma = 2.80 \pm 0.32$ is $\sim 3\sigma$ above the mean spectral index (1.89 ± 0.04) derived for the WISSH sample. Such a steep value can not be explained by the classical Comptonisation of AD photons by the hot corona, although, higher-redshift samples (e.g. the HYPERION sample - Zappacosta et al. 2023) exhibit Γ values closer to J1310+4601 one (Section 6.1). Table C.1 summarises the main properties of J1310+4601.

In order to deepen the knowledge about the origin of such a steep X-ray spectral slope, a 20 ks Swift proposal has been submitted by Enrico Piconcelli with the goal of collecting $\sim 150 - 200$ net counts in the observed $\sim 0.5 - 10$ keV band. The results of data analysis do not support those reported in the present thesis, however, the possibility of a variable X-ray spectral index will be further investigated.

J1310+4601, obsID = 25347			
Net counts	$\mathbf{N_H}$	**HR**	$\mathbf{F_{0.5-10}}$
48.0 ± 6.9	< 5.34	$-0.58^{+0.10}_{-0.13}$	-12.66 ± 0.07
$\mathbf{L_{2-10}}$	$\mathbf{k_{bol}}$	$\alpha_{\mathbf{OX}}$	$\lambda_{\mathbf{Edd}}$
45.71 ± 0.08	75 ± 17	-1.52 ± 0.11	0.77 ± 0.79

Table C.1: Summary of J1310+4601 properties: $0.3 - 7$ keV net counts; intrinsic column density (in units of 10^{22} cm^{-2}); Hardness ratio; observed $0.5 - 10$ keV flux (in units of Log(F/erg s^{-1} cm^{-2})); intrinsic $2 - 10$ keV luminosity (in units of Log(L/erg s^{-1})); bolometric correction; X-ray - to optical spectral index; Eddington ratio. Both uncertainties and upper limits are reported at 1σ confidence level.

Bibliography

Akritas, M. G. et al. (1996). "Linear Regression for Astronomical Data with Measurement Errors and Intrinsic Scatter". In: *The Astrophysical Journal*. DOI: 10.1086/177901.

Antonucci, R. (1993). "Unified models for active galactic nuclei and quasars". In: *Annual Review of Astronomy and Astrophysics*. DOI: 10.1146/annurev.aa.31.090193.002353.

Antonucci, R. R. J. et al. (1985). "Spectropolarimetry and the nature of NGC 1068". In: *The Astrophysical Journal*. DOI: 10.1086/163559.

Aravena, M. et al. (2016). "A survey of the cold molecular gas in gravitationally lensed star-forming galaxies at z $>$ 2". In: *Monthly Notices of the Royal Astronomical Society*. DOI: 10.1093/mnras/stw275.

Baade, W. et al. (1954). "Identification of the Radio Sources in Cassiopeia, Cygnus A, and Puppis A". In: *The Astrophysical Journal*. DOI: 10.1086/145812.

Ballo, L. et al. (2014). "The XMM-Newton Bright Survey sample of absorbed quasars: X-ray and accretion properties". In: *Monthly Notices of the Royal Astronomical Society*. DOI: 10.1093/mnras/stu1628.

Banerji, M. et al. (2012). "Heavily Reddened Quasars at z $\sim$ 2 in the UKIDSS Large Area Survey: A Transitional Phase in AGN Evolution". In: *Monthly Notices of the Royal Astronomical Society*. DOI: 10.1111/j.1365-2966.2012.22099.x.

— (2015). "Heavily reddened type 1 quasars at z $>$ 2. I. Evidence for significant obscured black hole growth at the highest quasar luminosities". In: *Monthly Notices of the Royal Astronomical Society*. DOI: 10.1093/mnras/stu2649.

— (2018). "The interstellar medium properties of heavily reddened quasars and companions at $z \sim 2.5$ with ALMA and JVLA". In: *Monthly Notices of the Royal Astronomical Society*. DOI: 10.1093/mnras/sty1443.

Baumgartner, W. H. et al. (2013). "The 70 month Swift-BAT all-sky hard X-ray survey". In: *The Astrophysical Journal Supplement Series*. DOI: 10.1088/0067-0049/207/2/19.

Beckmann, V. et al. (2012). "The AGN phenomenon: open issues". In: DOI: 10.22323/1.176.0069.

Bennett, C. L. et al. (2013). "Nine-Year Wilkinson Microwave Anisotropy Probe (WMAP) Observations: Final Maps and Results". In: *The Astrophysical Journal Supplement Series*. DOI: 10.1088/0067-0049/208/2/20.

Bianchi, S. et al. (2022). "Active Galactic Nuclei and Their Demography Through Cosmic Time". In: *Handbook of X-ray and Gamma-ray Astrophysics*. DOI: 10.1007/978-981-16-4544-0_113-1.

Bischetti, M. et al. (2017). "The WISSH quasars project. I. Powerful ionised outflows in hyper-luminous quasars". In: *Astronomy & Astrophysics*. DOI: 10.1051/0004-6361/201629301.

— (2018). "The WISSH quasars project. V. ALMA reveals the assembly of a giant galaxy around a z = 4.4 hyper-luminous QSO". In: *Astronomy & Astrophysics*. DOI: 10.1051/0004-6361/201833249.

— (2019). "The gentle monster PDS 456". In: *Astronomy & Astrophysics*. DOI: 10.1051/0004-6361/201935524.

— (2021). "The WISSH quasars project. IX. Cold gas content and environment of luminous QSOs at z $\sim$ 2.4˘4.7". In: *Astronomy & Astrophysics*. DOI: 10.1051/0004-6361/202039057.

Bisogni, S. et al. (2016). "Orientation effects on spectral emission features of quasars". In: *Monthly Notices of the Royal Astronomical Society*. DOI: 10.1093/mnras/stw2324.

Blandford, R. D. et al. (1978). "Extended and compact extragalactic radio sources: interpretation and theory". In: *Physica Scripta*. DOI: 10.1088/0031-8949/17/3/020.

Blandford, R. D. and D. G. Payne (1982). "Hydromagnetic flows from accretion disks and the production of radio jets". In: *Monthly Notices of the Royal Astronomical Society*. DOI: 10.1093/mnras/199.4.883.

Blandford, R. D. and R. L. Znajek (1977). "Electromagnetic extraction of energy from Kerr black holes". In: *Monthly Notices of the Royal Astronomical Society*. DOI: 10.1093/mnras/179.3.433.

Bolton, J. G. et al. (1949). "Positions of Three Discrete Sources of Galactic Radio-Frequency Radiation". In: *Nature*. DOI: 10.1038/164101b0.

Bongiorno, A. et al. (2014). "The $M_{BH} - M_*$ relation for X-ray obscured, red QSOs at $1.2 < z < 2.6$". In: *Monthly Notices of the Royal Astronomical Society*. DOI: 10.1093/mnras/stu1248.

Brandt, W. N. et al. (2000). "On the Nature of Soft X-Ray Weak Quasi-stellar Objects". In: *The Astrophysical Journal*. DOI: 10.1086/308207.

Brightman, M. et al. (2013). "A statistical relation between the X-ray spectral index and Eddington ratio of active galactic nuclei in deep surveys". In: *Monthly Notices of the Royal Astronomical Society*. DOI: 10.1093/mnras/stt920.

Bruni, G. et al. (2019). "The WISSH quasars project. VI. Fraction and properties of BAL quasars in the hyper-luminosity regime". In: *Astronomy & Astrophysics*. DOI: 10.1051/0004-6361/201834940.

— (2023). "Radio WISSH: tuning on the most luminous quasars in the Universe". In: *Proceedings of the International Astronomical Union*. DOI: 10.48550/arXiv.2307.02634.

Brusa, M. et al. (2014). "X-shooter reveals powerful outflows in z $\sim$ 1.5 X-ray selected obscured quasi-stellar objects". In: *Monthly Notices of the Royal Astronomical Society*. DOI: 10.1093/mnras/stu2117.

— (2015). "Evidence for feedback in action from the molecular gas content in the $z \sim 1.6$ outflowing QSO XID2028". In: *Astronomy & Astrophysics*. DOI: 10.1051/0004-6361/201425491.

Chartas, G. et al. (2020). "Linking the small scale relativistic winds and the large scale molecular outflows in the z = 1.51 lensed quasar HS 0810+2554". In: *Monthly Notices of the Royal Astronomical Society*. DOI: 10.1093/mnras/staa1534.

Chen, C.-T. J. et al. (2017). "The X-Ray and Mid-infrared Luminosities in Luminous Type 1 Quasars". In: *The Astrophysical Journal*. DOI: 10.3847/1538-4357/837/2/145.

Cheng, H. et al. (2020). "Magnetic reconnection-heated corona in active galactic nuclei: refined disc - corona model and application to broad-band radiation". In: *Monthly Notices of the Royal Astronomical Society*. DOI: 10.1093/mnras/staa1250.

Ciotti, L. and J. P. Ostriker (1997). "Cooling Flows and Quasars: Different Aspects of the Same Phenomenon? I. Concepts". In: *The Astrophysical Journal*. DOI: 10.1086/310902.

Coatman, L. et al. (2017). "Correcting CIV-based virial black hole masses". In: *Monthly Notices of the Royal Astronomical Society*. DOI: 10.1093/mnras/stw2797.

Cohen, R. D. (1983). "The narrow-line region of intermediate Seyfet galaxies". In: *The Astrophysical Journal*. DOI: 10.1086/161386.

Costa, T. et al. (2014). "Feedback from active galactic nuclei: energy- versus momentum-driving". In: *Monthly Notices of the Royal Astronomical Society*. DOI: 10.1093/mnras/stu1632.

Dai, X. et al. (2008). "2MASS Reveals a Large Intrinsic Fraction of BALQSOs". In: *The Astrophysical Journal*. DOI: 10.1086/523688.

Dannen, R. C. et al. (2019). "Photoionization Calculations of the Radiation Force Due To Spectral Lines in AGNs". In: *The Astrophysical Journal*. DOI: 10.3847/1538-4357/ab340b.

Denney, K. D. (2012). "Are Outflows Biasing Single-Epoch CIV Black Hole Mass Estimates?" In: *The Astrophysical Journal*. DOI: 10.1088/0004-637x/759/1/44.

Du, P. et al. (2015). "Supermassive black holes with high accretion rates in Active Galactic Nuclei. IV. Hβ time lags and implications for Super-Eddington accretion". In: *The Astrophysical Journal*. DOI: 10.1088/0004-637x/806/1/22.

— (2016). "Supermassive black holes with high accretion rates in Active Galactic Nuclei. V. A new size-luminosity scaling relation for Broad-Line Region". In: *The Astrophysical Journal*. DOI: 10.3847/0004-637x/825/2/126.

— (2018). "Supermassive black holes with high accretion rates in Active Galactic Nuclei. IX. 10 new observations of reverberation mapping and shortened Hβ lags". In: *The Astrophysical Journal*. DOI: 10.3847/1538-4357/aaae6b.

Duras, F. et al. (2017). "The WISSH quasars project. II. Giant star nurseries in hyper-luminous quasars". In: *Astronomy & Astrophysics*. DOI: 10.1051/0004-6361/201731052.

— (2020). "Universal bolometric corrections for Active Galactic Nuclei over seven luminosity decades". In: *Astronomy & Astrophysics*. DOI: 10.1051/0004-6361/201936817.

Eckart, M. E. et al. (2009). "A comparison of X-ray and mid-Infrared selection of obscured AGN". In: *The Astrophysical Journal*. DOI: 10.1088/0004-637x/708/1/584.

Elitzur, M. et al. (2006). "The AGN-obscuring Torus: The End of the 'Doughnut' Paradigm?" In: *The Astrophysical Journal*. DOI: 10.1086/508158.

Elitzur, M. (2008). "The toroidal obscuration of active galactic nuclei". In: *New Astronomy Reviews*. DOI: 10.1016/j.newar.2008.06.010.

Elvis, M. et al. (1994). "Atlas of Quasar Energy Distributions". In: *The Astrophysical Journal Supplement Series*. DOI: 10.1086/192093.

Fabian, A. et al. (2012). "Observational Evidence of Active Galactic Nuclei Feedback". In: *Annual Review of Astronomy and Astrophysics*. DOI: 10.1146/annurev-astro-081811-125521.

Fabian, A. C. et al. (2006). "Radiative pressure feedback by a quasar in a galactic bulge". In: *Monthly Notices of the Royal Astronomical Society: Letters*. DOI: 10.1111/j.1745-3933.2006.00234.x.

Fabian, A. C. et al. (2008). "The effect of radiation pressure on dusty absorbing gas around active galactic nuclei". In: *Monthly Notices of the Royal Astronomical Society: Letters*. DOI: 10.1111/j.1745-3933.2008.00430.x.

— (2015). "Properties of AGN coronae in the NuSTAR era". In: *Monthly Notices of the Royal Astronomical Society*. DOI: 10.1093/mnras/stv1218.

Fan, L. et al. (2008). "The correlation between X-ray and UV properties of BAL QSOs". In: *The Astrophysical Journal*. DOI: 10.1088/0004-637x/690/1/1006.

Fanaroff, B. L. and J. M. Riley (1974). "The morphology of extragalactic radio sources of high and low luminosity". In: *Monthly Notices of the Royal Astronomical Society*. DOI: 10.1093/mnras/167.1.31P.

Faucher-Giguère, C.-A. and E. Quataert (2012). "The physics of galactic winds driven by active galactic nuclei". In: *Monthly Notices of the Royal Astronomical Society*. DOI: 10.1111/j.1365-2966.2012.21512.x.

Fawcett, V. A. et al. (2020). "Fundamental differences in the radio properties of red and blue quasars: enhanced compact AGN emission in red quasars". In: *Monthly Notices of the Royal Astronomical Society*. DOI: 10.1093/mnras/staa954.

Ferrarese, L. et al. (2000). "A Fundamental Relation between Supermassive Black Holes and Their Host Galaxies". In: *The Astrophysical Journal*. DOI: 10.1086/312838.

Feruglio, C. et al. (2015). "The multi-phase winds of Markarian 231: from the hot, nuclear, ultra-fast wind to the galaxy-scale, molecular outflow". In: *Astronomy & Astrophysics*. DOI: 10.1051/0004-6361/201526020.

— (2017). "On the discovery of fast molecular gas in the UFO/BAL quasar APM 08279+5255 at z=3.912". In: *Astronomy & Astrophysics*. DOI: 10.1051/0004-6361/201731387.

Fiore, F. et al. (2008). "Unveiling Obscured Accretion in the Chandra Deep Field-South". In: *The Astrophysical Journal*. DOI: 10.1086/523348.

— (2009). "Chasing highly obscured QSOs in the COSMOS field". In: *The Astrophysical Journal*. DOI: 10.1088/0004-637x/693/1/447.

— (2017). "AGN wind scaling relations and the co-evolution of black holes and galaxies". In: *Astronomy & Astrophysics*. DOI: 10.1051/0004-6361/201629478.

Fukumura, K. et al. (2018). "Variable Nature of Magnetically Driven Ultra-fast Outflows". In: *The Astrophysical Journal*. DOI: 10.3847/2041-8213/aadd10.

Gallagher, S. C. et al. (2002). "X-Ray Spectroscopy of Quasi-Stellar Objects with Broad Ultraviolet Absorption Lines". In: *The Astrophysical Journal*. DOI: 10.1086/338485.

Gallagher, S. C. et al. (2007). "Radio through X-Ray Spectral Energy Distributions of 38 Broad Absorption Line Quasars". In: *The Astrophysical Journal*. DOI: 10.1086/519438.

Gandhi, P. et al. (2009). "Resolving the mid-infrared cores of local Seyferts". In: *Astronomy & Astrophysics*. DOI: 10.1051/0004-6361/200811368.

Garcia-Burillo, S. et al. (2019). "ALMA images the many faces of the NGC 1068 torus and its surroundings". In: *Astronomy & Astrophysics*. DOI: 10.1051/0004-6361/201936606.

Gebhardt, K. et al. (2000). "A Relationship between Nuclear Black Hole Mass and Galaxy Velocity Dispersion". In: *The Astrophysical Journal*. DOI: 10.1086/312840.

Georgantopoulos, I. et al. (2011). "On the $L_X - L_{6\,\mu m}$ ratio as a diagnostic for Compton-thick AGN". In: *Astronomy & Astrophysics*. DOI: 10.1051/0004-6361/201117400.

Giacconi, R. et al. (2002). "Chandra Deep Field South: the 1 Ms catalog". In: *The Astrophysical Journal Supplement Series*. DOI: 10.1086/338927.

Gibson, R. R. et al. (2009). "A catalogue of broad absorption line quasars in Sloan Digital Sky Survey Data Release 5". In: *The Astrophysical Journal*. DOI: 10.1088/0004-637x/692/1/758.

Glikman, E. et al. (2012). "FIRST-2MASS Red Quasars: Transitional Objects Emerging from the Dust". In: *The Astrophysical Journal*. DOI: 10.1088/0004-637x/757/1/51.

— (2015). "Major Mergers Host the Most Luminous Red Quasars at z $\sim$ 2: A Hubble Space Telescope WFC3/IR Study". In: *The Astrophysical Journal*. DOI: 10.1088/0004-637X/806/2/218.

Glikman, E. (2017). "Red Quasars are in a Radiatively Driven Blow-out Phase". In: *Research Notes of the AAS*. DOI: 10.3847/2515-5172/aaa0c0.

Glikman, E. et al. (2018). "Luminous WISE-selected Obscured, Unobscured, and Red Quasars in Stripe 82". In: *The Astrophysical Journal*. DOI: 10.3847/1538-4357/aac5d8.

Haardt, F. et al. (1991). "A Two-Phase Model for the X-Ray Emission from Seyfert Galaxies". In: *Astrophysical Journal Letters*. DOI: 10.1086/186171.

— (1993). "X-Ray Spectra from Two-Phase Accretion Disks". In: *The Astrophysical Journal*. DOI: 10.1086/173020.

Harrison, C. M. (2017). "Impact of supermassive black hole growth on star formation". In: *Nature Astronomy*. DOI: 10.1038/s41550-017-0165.

Heckman, T. M. et al. (2014). "The Coevolution of Galaxies and Supermassive Black Holes: Insights from Surveys of the Contemporary Universe". In: *An-*

nual Review of Astronomy and Astrophysics. DOI: 10.1146/annurev-astro-081913-035722.

Hewett, P. C. et al. (2010). "Improved redshifts for SDSS quasar spectra". In: *Monthly Notices of the Royal Astronomical Society*. DOI: 10.1111/j.1365-2966.2010.16648.x.

Horst, H. et al. (2007). "The mid-IR − hard X-ray correlation in AGN and its implications for dusty torus models". In: *Astronomy & Astrophysics*. DOI: 10.1051/0004-6361:20078548.

Hwang, H.-C. et al. (2018). "Winds as the origin of radio emission in z = 2.5 radio-quiet extremely red quasars". In: *Monthly Notices of the Royal Astronomical Society*. DOI: 10.1093/mnras/sty742.

Ishibashi, W. et al. (2018). "Revisiting the 'forbidden' region: AGN radiative feedback with radiation trapping". In: *Monthly Notices of the Royal Astronomical Society*. DOI: 10.1093/mnras/sty1620.

Ishibashi, W. and A. C. Fabian (2015). "AGN feedback: galactic-scale outflows driven by radiation pressure on dust". In: *Monthly Notices of the Royal Astronomical Society*. DOI: 10.1093/mnras/stv944.

— (2016). "AGN - starburst evolutionary connection: a physical interpretation based on radiative feedback". In: *Monthly Notices of the Royal Astronomical Society*. DOI: 10.1093/mnras/stw2063.

Jansen, F. et al. (2001). "XMM-Newton observatory. I. The spacecraft and operations". In: *Astronomy & Astrophysics*. DOI: 10.1051/0004-6361:20000036.

Jiang, Y.-F. et al. (2011). "Black hole mass and bulge luminosity for low-mass black holes". In: *The Astrophysical Journal*. DOI: 10.1088/2041-8205/737/2/l45.

Jin, C. et al. (2012). "A combined optical and X-ray study of unobscured type 1 active galactic nuclei. I. Optical spectra and spectral energy distribution modelling". In: *Monthly Notices of the Royal Astronomical Society*. DOI: 10.1111/j.1365-2966.2011.19805.x.

Just, D. W. et al. (2007). "The X-Ray Properties of the Most Luminous Quasars from the Sloan Digital Sky Survey". In: *The Astrophysical Journal*. DOI: 10.1086/519990.

Kellermann, K. I. (2014). "The road to quasars". In: *Proceedings of the International Astronomical Union*. DOI: 10.1017/s1743921315002185.

Kelly, B. C. et al. (2008). "Observational Constraints on the Dependence of Radio-Quiet Quasar X-Ray Emission on Black Hole Mass and Accretion Rate". In: *The Astrophysical Journal Supplement Series*. DOI: 10.1086/533440.

Kennicutt, R. C. (1998). "Star formation in galaxies along the Hubble sequence". In: *Annual Review of Astronomy and Astrophysics*. DOI: 10.1146/annurev.astro.36.1.189.

Kim, D. et al. (2015). "Accretion rates of red quasars from the hydrogen Pβ line". In: *The Astrophysical Journal*. DOI: 10.1088/0004-637x/812/1/66.

Kimball, A. E. et al. (2008). "A unified catalog of radio objects detected by NVSS, FIRST, WENSS, GB6, and SDSS". In: *The Astronomical Journal*. DOI: 10.1088/0004-6256/136/2/684.

King, A. (2003). "Black Holes, Galaxy Formation, and the $M_{BH} - \sigma$ Relation". In: *The Astrophysical Journal*. DOI: 10.1086/379143.

— (2005). "The AGN-starburst connection, Galactic superwinds, and $M_{BH} - \sigma$". In: *The Astrophysical Journal*. DOI: 10.1086/499430.

— (2010). "Black hole outflows". In: *Monthly Notices of the Royal Astronomical Society*. DOI: 10.1111/j.1365-2966.2009.16013.x.

King, A. and K. Pounds (2015). "Powerful Outflows and Feedback from Active Galactic Nuclei". In: *Annual Review of Astronomy and Astrophysics*. DOI: 10.1146/annurev-astro-082214-122316.

Klindt, L. et al. (2019). "Fundamental differences in the radio properties of red and blue quasars: evolution strongly favoured over orientation". In: *Monthly Notices of the Royal Astronomical Society*. DOI: 10.1093/mnras/stz1771.

Krawczyk, C. M. et al. (2013). "Mean Spectral Energy Distributions and bolometric corrections for luminous quasars". In: *The Astrophysical Journal Supplement Series*. DOI: 10.1088/0067-0049/206/1/4.

Kubota, A. et al. (2018). "A physical model of the broadband continuum of AGN and its implications for the UV/X relation and optical variability". In: *Monthly Notices of the Royal Astronomical Society*. DOI: 10.1093/mnras/sty1890.

Lamastra, A. et al. (2010). "The building up of the black hole mass - stellar mass relation". In: *Monthly Notices of the Royal Astronomical Society*. DOI: 10.1111/j.1365-2966.2010.16439.x.

Lansbury, G. B. et al. (2014). "NuSTAR Observations of Heavily Obscured Quasars at $z \sim 0.5$". In: *The Astrophysical Journal*. DOI: 10.1088/0004-637x/785/1/17.

— (2020). "X-ray observations of luminous dusty quasars at $z > 2$". In: *Monthly Notices of the Royal Astronomical Society*. DOI: 10.1093/mnras/staa1220.

Lanzuisi, G. et al. (2009). "Revealing X-ray obscured quasars in SWIRE sources with extreme mid-IR/optical flux ratios". In: *Astronomy & Astrophysics*. DOI: 10.1051/0004-6361/200811282.

Laor, A. et al. (1994). "The Soft X-Ray Properties of a Complete Sample of Optically Selected Quasars. I. First Results". In: *The Astrophysical Journal*. DOI: 10.1086/174841.

Laurenti, M. et al. (2022). "X-ray spectroscopic survey of highly accreting AGN". In: *Astronomy & Astrophysics*. DOI: 10.1051/0004-6361/202141829.

Lawson, A. J. et al. (1997). "Ginga observations of the X-ray spectra of quasars". In: *Monthly Notices of the Royal Astronomical Society*. DOI: 10.1093/mnras/288.4.920.

Lehmer, B. D. et al. (2005). "The Etended Chandra Deep Field South survey. Cha ndra point-source catalogs". In: *The Astrophysical Journal Supplement Series*. DOI: 10.1086/444590.

Leighly, K. M. (2004). "HST STIS Ultraviolet Spectral Evidence of Outflow in Extreme Narrow-line Seyfert 1 Galaxies. II. Modeling and Interpretation". In: *The Astrophysical Journal*. DOI: 10.1086/422089.

Liu, H. et al. (2018). "The Frequency of Intrinsic X-Ray Weakness among Broad Absorption Line Quasars". In: *The Astrophysical Journal*. DOI: 10.3847/1538-4357/aabe8d.

— (2021). "On the Observational Difference between the Accretion Disk-Corona Connections among Super- and Sub-Eddington Accreting Active Galactic Nuclei". In: *The Astrophysical Journal*. DOI: 10.3847/1538-4357/abe37f.

Luo, B. et al. (2008). "The Chandra Deep Field-South survey: 2 Ms source catalogs". In: *The Astrophysical Journal Supplement Series*. DOI: 10.1086/591248.

— (2013). "Weak Hard X-ray Emission from Two Broad Absorption Line Quasars Observed with NuSTAR: Compton-thick Absorption or Intrinsic X-ray Weakness?" In: *The Astrophysical Journal*. DOI: 10.1088/0004-637x/772/2/153.

— (2014). "Weak hard X-ray emission from Broad Absorption Line quasars: evidence for X-ray weakness". In: *The Astrophysical Journal*. DOI: 10.1088/0004-637x/794/1/70.

— (2015). "X-ray insights into the nature of PHL 1811 analogs and weak emission-line quasars: unification with a geometrically thick accretion disk?" In: *The Astrophysical Journal*. DOI: 10.1088/0004-637x/805/2/122.

Lusso, E. et al. (2010). "The X-ray to optical-UV luminosity ratio of X-ray selected type 1 AGN in XMM-COSMOS". In: *Astronomy & Astrophysics*. DOI: 10.1051/0004-6361/200913298.

— (2012). "Bolometric luminosities and Eddington ratios of X-ray selected active galactic nuclei in the XMM-COSMOS survey". In: *Monthly Notices of the Royal Astronomical Society*. DOI: 10.1111/j.1365-2966.2012.21513.x.

Lusso, E. et al. (2016). "The tight relation between X-ray and ultraviolet luminosity of quasars". In: *The Astrophysical Journal*. DOI: 10.3847/0004-637x/819/2/154.

— (2023). "The Dawn of Black Holes". In: *Handbook of X-ray and Gamma-ray Astrophysics*. DOI: 10.1007/978-981-16-4544-0_116-1.

Lutz, D. et al. (2004). "The relation between AGN hard X-ray emission and mid-infrared continuum from ISO spectra: Scatter and unification aspects". In: *Astronomy & Astrophysics*. DOI: 10.1051/0004-6361:20035838.

Lyke, B. W. et al. (2020). "The Sloan Digital Sky Survey Quasar Catalog: Sixteenth Data Release". In: *The Astrophysical Journal Supplement Series*. DOI: 10.3847/1538-4365/aba623.

Maiolino, R. et al. (2001). "Dust in active nuclei. I. Evidence for 'anomalous' properties". In: *Astronomy & Astrophysics*. DOI: 10.1051/0004-6361:20000177.

Martocchia, S. et al. (2017). "The WISSH quasars project. III. X-ray properties of hyper-luminous quasars". In: *Astronomy & Astrophysics*. DOI: 10.1051/0004-6361/201731314.

Mateos, S. et al. (2015). "Revisiting the relationship between 6 μm and (2−10) keV continuum luminosities of AGN". In: *Monthly Notices of the Royal Astronomical Society*. DOI: 10.1093/mnras/stv299.

Matteo, T. Di et al. (2005). "Energy input from quasars regulates the growth and activity of black holes and their host galaxies". In: *Nature*. DOI: 10.1038/nature03335.

Matzeu, G. A. et al. (2017). "Evidence for a radiatively driven disc-wind in PDS456?" In: *Monthly Notices of the Royal Astronomical Society: Letters*. DOI: 10.1093/mnrasl/slx129.

— (2023). "Supermassive Black Hole Winds in X-rays: SUBWAYS. I. Ultra-fast outflows in QSOs beyond the local Universe". In: *Astronomy & Astrophysics*. DOI: 10.1051/0004-6361/202245036.

McNamara, B. R. et al. (2009). "An Energetic AGN Outburst Powered by a Rapidly Spinning Supermassive Black Hole or an Accreting Ultramassive Black Hole". In: *The Astrophysical Journal*. DOI: 10.1088/0004-637x/698/1/594.

Menci, N. et al. (2014). "Triggering Active Galactic Nuclei in hierarchical galaxy formation: disk instabilities vs. interactions". In: *Astronomy & Astrophysics*. DOI: 10.1051/0004-6361/201424217.

Meyer, R. A. et al. (2019). "New constraints on quasar evolution: broad-line velocity shifts over $1.5 \leq z \leq 7.5$". In: *Monthly Notices of the Royal Astronomical Society*. DOI: 10.1093/mnras/stz1504.

Monadi, R. et al. (2022). "Improved selection of extremely red quasars with boxy CIV lines in BOSS". In: *Monthly Notices of the Royal Astronomical Society*. DOI: 10.1093/mnras/stac294.

Moster, B. P. et al. (2012). "Galactic star formation and accretion histories from matching galaxies to dark matter haloes". In: *Monthly Notices of the Royal Astronomical Society*. DOI: 10.1093/mnras/sts261.

Nardini, E. et al. (2019). "The most luminous blue quasars at $3.0 < z < 3.3$. I. A tale of two X-ray populations". In: *Astronomy & Astrophysics*. DOI: 10.1051/0004-6361/201936911.

Netzer, H. (2015). "Revisiting the Unified Model of Active Galactic Nuclei". In: *Annual Review of Astronomy and Astrophysics*. DOI: 10.1146/annurev-astro-082214-122302.

Nomura, M. et al. (2020). "Line-driven disc wind in near-Eddington active galactic nuclei: decrease of mass accretion rate due to powerful outflow". In: *Monthly Notices of the Royal Astronomical Society*. DOI: 10.1093/mnras/staa948.

Osterbrock, D. E. (1978). "An Observational Model of the Ionized Gas in Seyfert and Radio-Galaxy Nuclei". In: *Bulletin of the American Astronomical Society*. DOI: 10.1073/pnas.75.2.540.

Padovani, P. (2016). "The faint radio sky: radio astronomy becomes mainstream". In: *The Astronomy and Astrophysics Review*. DOI: 10.1007/s00159-016-0098-6.

Padovani, P. et al. (2017). "Active Galactic Nuclei: what's in a name?" In: *The Astronomy and Astrophysics Review*. DOI: 10.1007/s00159-017-0102-9.

Pâris, Isabelle et al. (2014). "The Sloan Digital Sky Survey quasar catalog: tenth data release". In: *Astronomy & Astrophysics*. DOI: 10.1051/0004-6361/201322691.

Park, Taeyoung et al. (2006). "Bayesian Estimation of Hardness Ratios: Modeling and Computations". In: *The Astrophysical Journal*. DOI: 10.1086/507406.

Peacock, J. A. et al. (1981). "Multifrequency models for the cosmological evolution of extragalactic radio sources". In: *Monthly Notices of the Royal Astronomical Society*. DOI: 10.1093/mnras/196.3.611.

Perna, M. et al. (2018). "The molecular gas content in obscured AGN at $z > 1$". In: *Astronomy & Astrophysics*. DOI: 10.1051/0004-6361/201833040.

Perrotta, S et al. (2019). "ERQs are the BOSS of quasar samples: the highest velocity [OIII] quasar outflows". In: *Monthly Notices of the Royal Astronomical Society*. DOI: 10.1093/mnras/stz1993.

Peterson, B. M. (1997). *An Introduction to Active Galactic Nuclei*. Cambridge University Press.

Piconcelli, E. et al. (2005). "The XMM-Newton view of PG quasars I. X-ray continuum and absorption". In: *Astronomy & Astrophysics*. DOI: 10.1051/0004-6361:20041621.

Pounds, K. A. et al. (1995). "RE 1034+39: a high-state Seyfert galaxy?" In: *Monthly Notices of the Royal Astronomical Society*. DOI: 10.1093/mnras/277.1.L5.

Proga, D. (2003). "Numerical Simulations of Mass Outflows Driven from Accretion Disks by Radiation and Magnetic Forces". In: *The Astrophysical Journal*. DOI: 10.1086/345897.

Proga, D. et al. (2004). "Dynamics of Line-Driven Disk Winds in Active Galactic Nuclei. II. Effects of Disk Radiation". In: *The Astrophysical Journal*. DOI: 10.1086/425117.

Proga, D. (2005). "How Much X-Ray and UV Radiation Processes Are Coupled in Accretion Disks? The Active Galactic Nucleus Case". In: *The Astrophysical Journal*. DOI: 10.1086/462417.

— (2007). "Theory of winds in AGNs". In: *The Central Engine of Active Galactic Nuclei, ASP Conf. Ser.* DOI: 10.48550/arXiv.astro-ph/0701100.

Reeves, J. N. et al. (2000). "X-ray spectra of a large sample of quasars with ASCA". In: *Monthly Notices of the Royal Astronomical Society*. DOI: 10.1046/j.1365-8711.2000.03510.x.

Ricci, Claudio et al. (2017). "The close environments of accreting massive black holes are shaped by radiative feedback". In: *Nature*. DOI: 10.1038/nature23906.

Richards, Gordon T. et al. (2006). "Spectral Energy Distributions and Multiwavelength Selection of Type 1 Quasars". In: *The Astrophysical Journal Supplement Series*. DOI: 10.1086/506525.

Risaliti, G. et al. (2009). "The SDSS/XMM-Newton Quasar Survey: Correlation between X-ray spectral slope and Eddington ratio". In: *The Astrophysical Journal*. DOI: 10.1088/0004-637x/700/1/l6.

— (2011). "[O III] equivalent width and orientation effects in quasars". In: *Monthly Notices of the Royal Astronomical Society*. DOI: 10.1111/j.1365-2966.2010.17843.x.

Rivera, G. Calistro et al. (2021). "The multiwavelength properties of red QSOs: Evidence for dusty winds as the origin of QSO reddening". In: *Astronomy & Astrophysics*. DOI: 10.1051/0004-6361/202040214.

Rosario, D. J. et al. (2020). "Fundamental differences in the radio properties of red and blue quasars: insight from the LOFAR Two-metre Sky Survey (LoTSS)". In: *Monthly Notices of the Royal Astronomical Society*. DOI: 10.1093/mnras/staa866.

Rosario, D. J. et al. (2021). "Fundamental differences in the radio properties of red and blue quasars: kiloparsec-scale structures revealed by e-MERLIN". In: *Monthly Notices of the Royal Astronomical Society*. DOI: 10.1093/mnras/stab1653.

Rovilos, E. et al. (2013). "A wide search for obscured active galactic nuclei using XMM-Newton and WISE". In: *Monthly Notices of the Royal Astronomical Society*. DOI: 10.1093/mnras/stt2228.

Saccheo, I. et al. (2023). "The WISSH quasars project. XI. The mean spectral energy distribution and bolometric corrections of the most luminous quasars". In: *Astronomy & Astrophysics*. DOI: 10.1051/0004-6361/202244296.

Schmidt, M. (1963). "3C 273 : A Star-Like Object with Large Red-Shift". In: *Nature*. DOI: 10.1038/1971040a0.

Schneider, D. P. et al. (2007). "The Sloan Digital Sky Survey Quasar Catalog. IV. Fifth Data Release". In: *The Astronomical Journal*. DOI: 10.1086/518474.

— (2010). "The Sloan Digital Sky Survey Quasar Catalog. V. Seventh Data Release". In: *The Astronomical Journal*. DOI: 10.1088/0004-6256/139/6/2360.

Schneider, R. et al. (2015). "The origin od the Far-infrared continuum of $z \sim 6$ quasars: a radiative transfer model for SDSS J1148+5251". In: *Astronomy & Astrophysics*. DOI: 10.1051/0004-6361/20152610.

Seyfert, C. K. (1963). "Nuclear Emission in Spiral Nebulae". In: *The Astrophysical Journal*. DOI: 10.1086/144488.

Shakura, N. I. and R. A. Sunyaev (1973). "Black holes in binary systems. Observational appearance." In: *Astronomy & Astrophysics*.

Shankar, Francesco et al. (2008). "Dependence of the Broad Absorption Line Quasar Fraction on Radio Luminosity". In: *The Astrophysical Journal*. DOI: 10.1086/591488.

Shemmer, O. et al. (2006). "Chandra Observations of the Highest Redshift Quasars from the Sloan Digital Sky Survey". In: *The Astrophysical Journal*. DOI: 10.1086/503543.

— (2008). "The Hard X-Ray Spectrum as a Probe for Black Hole Growth in Radio-Quiet Active Galactic Nuclei". In: *The Astrophysical Journal*. DOI: 10.1086/588776.

Somerville, R. S. et al. (2008). "A semi-analytic model for the co-evolution of galaxies, black holes and active galactic nuclei". In: *Monthly Notices of the Royal Astronomical Society*. DOI: 10.1111/j.1365-2966.2008.13805.x.

Spergel, D. N. et al. (2003). "First Year Wilkinson Microwave Anisotropy Probe (WMAP) Observations: Determination of Cosmological Parameters". In: *The Astrophysical Journal Supplement Series*. DOI: 10.1086/377226.

Steffen, A. T. et al. (2006). "The X-Ray-to-Optical Properties of Optically Selected Active Galaxies over Wide Luminosity and Redshift Ranges". In: *The Astronomical Journal*. DOI: 10.1086/503627.

Stern, D. et al. (2014). "NuSTAR and XMM-Newton Observations of Luminous, Heavily Obscured, WISE-Selected Quasars at z $\sim$ 2". In: *The Astrophysical Journal*. DOI: 10.1088/0004-637x/794/2/102.

Stern, D. (2015). "The X-ray to Mid-Infrared relation of AGN at high luminosity". In: *The Astrophysical Journal*. DOI: 10.1088/0004-637x/807/2/129.

Tacconi, L. J. et al. (2018). "PHIBSS: Unified Scaling Relations of Gas Depletion Time and Molecular Gas Fractions". In: *The Astrophysical Journal*. DOI: 10.3847/1538-4357/aaa4b4.

Temple, Matthew J. et al. (2019). "[OIII] Emission line properties in a new sample of heavily reddened quasars at z $>$ 2". In: *Monthly Notices of the Royal Astronomical Society*. DOI: 10.1093/mnras/stz1420.

Tombesi, F. et al. (2010). "Evidence for ultra-fast outflows in radio-quiet AGNs. I. Detection and statistical incidence of Fe K-shell absorption lines". In: *Astronomy & Astrophysics*. DOI: 10.1051/0004-6361/200913440.

— (2012). "Evidence for ultra-fast outflows in radio-quiet AGNs. III. Location and energetics". In: *Monthly Notices of the Royal Astronomical Society: Letters*. DOI: 10.1111/j.1745-3933.2012.01221.x.

— (2015). "Wind from the black-hole accretion disk driving a molecular outflow in an active galaxy". In: *Nature*. DOI: 10.1038/nature14261.

Trakhtenbrot, B. et al. (2017). "The Swift/BAT AGN Spectroscopic Survey (BASS). VI. The $\Gamma_X - L/L_{Edd}$ relation". In: *Monthly Notices of the Royal Astronomical Society*. DOI: 10.1093/mnras/stx1117.

Travascio, A. et al. (2020). "The WISSH quasars project. VIII. Outflows and metals in the circum-galactic medium around the hyper-luminous z $\sim$ 3.6 quasar J1538+08". In: *Astronomy & Astrophysics*. DOI: 10.1051/0004-6361/201936197.

Trefoloni, B. et al. (2023). "The most luminous blue quasars at 3.0 $<$ z $<$ 3.3. III. LBT spectra and accretion parameters". In: *arXiv e-prints*. DOI: 10.48550/arXiv.2305.07699.

Tremaine, S. et al. (2002). "The Slope of the Black Hole Mass versus Velocity Dispersion Correlation". In: *The Astrophysical Journal*. DOI: 10.1086/341002.

Tristram, K. R. W. et al. (2014). "The dusty torus in the Circinus galaxy: a dense disk and the torus funnel". In: *Astronomy & Astrophysics*. DOI: 10.1051/0004-6361/201322698.

Urrutia, T. et al. (2008). "Evidence for Quasar Activity Triggered by Galaxy Mergers in HST Observations of Dust-reddened Quasars". In: *The Astrophysical Journal*. DOI: 10.1086/523959.

— (2009). "The FIRST-2MASS red quasar survey. II. An anomalously high fraction of LoBALs in searchers for dust-reddened quasars". In: *The Astrophysical Journal*. DOI: 10.1088/0004-637x/698/2/1095.

Urry, C. M. and P. Padovani (1995). "Unified Schemes for Radio-Loud Active Galactic Nuclei". In: *Publications of the Astronomical Society of the Pacific*. DOI: 10.1086/133630.

Vayner, A. et al. (2021). "Powerful winds in high-redshift obscured and red quasars". In: *Monthly Notices of the Royal Astronomical Society*. DOI: 10.1093/mnras/stab1176.

Veilleux, S. et al. (2017). "Quasar Feedback in the Ultraluminous Infrared Galaxy F11119+3257: Connecting the Accretion Disk Wind with the Large-Scale Molecular Outflow". In: *The Astrophysical Journal*. DOI: 10.3847/1538-4357/aa767d.

Venemans, Bram P. et al. (2017). "Molecular gas in three $z \sim 7$ quasar host galaxies". In: *The Astrophysical Journal*. DOI: 10.3847/1538-4357/aa81cb.

Vietri, G. et al. (2018). "The WISSH quasars project. IV. Broad line region versus kiloparsec-scale winds". In: *Astronomy & Astrophysics*. DOI: 10.1051/0004-6361/201732335.

— (2020). "SUPER III. Broad line region properties of AGN at $z \sim 2$". In: *Astronomy & Astrophysics*. DOI: 10.1051/0004-6361/202039136.

— (2022). "The WISSH quasars project. X. Discovery of a multi-component and highly variable UV ultra-fast outflow in a z = 3.6 quasar". In: *Astronomy & Astrophysics*. DOI: 10.1051/0004-6361/202243285.

Vito, F. et al. (2019). "The X-ray properties of z > 6 quasars: no evident evolution of accretion physics in the first Gyr of the Universe". In: *Astronomy & Astrophysics*. DOI: 10.1051/0004-6361/201936217.

Wall, J. V. (1975). "The quasars from the Parkes 2700-MHz survey". In: *The Observatory*.

Weedman, Daniel et al. (2012). "Infrared classification and luminosities for dusty active galactic nuclei and the most luminous quasars". In: *The Astrophysical Journal*. DOI: 10.1088/0004-637x/761/2/184.

Weisskopf, Martin C. et al. (2007). "A Chandra Search for Coronal X-Rays from the Cool White Dwarf GD 356". In: *The Astrophysical Journal*. DOI: 10.1086/510776.

Whittle, M. (1985). "The narrow line region of active galaxies. II. Relations between OIII profile shape and other properties". In: *Monthly Notices of the Royal Astronomical Society*. DOI: 10.1093/mnras/213.1.33.

Willott, C. J. et al. (2001). "The radio luminosity function from the low-frequency 3CRR, 6CE and 7CRS complete samples". In: *Monthly Notices of the Royal Astronomical Society*. DOI: 10.1046/j.1365-8711.2001.04101.x.

Wright, Edward L. et al. (2010). "The Wide-field Infrared Survey Explorer (WISE): Mission Description and Initial On-orbit Performance". In: *The Astrophysical Journal*. DOI: 10.1088/0004-6256/140/6/1868.

Wu, Jianfeng et al. (2011). "A population of X-ray weak quasars: PHL 1811 analogs at high redshift". In: *The Astrophysical Journal*. DOI: 10.1088/0004-637x/736/1/28.

Xue, Y. Q. et al. (2011). "The Chandra Deep Field-South survey: 4 Ms source catalogs". In: *The Astrophysical Journal Supplement Series*. DOI: 10.1088/0067-0049/195/1/10.

Yang, C. et al. (2017). "Molecular gas in Herschel-selected strongly lensed submillimeter galaxies at $z \sim 2-4$ as probed by multi-J CO". In: *Astronomy & Astrophysics*. DOI: 10.1051/0004-6361/201731391.

Yi, Weimin et al. (2020). "Spectroscopy of Broad Absorption Line Quasars at $3 \leq z \leq 5$. I. Evidence for Quasar Winds Shaping Broad/Narrow Emission Line Regions". In: *The Astrophysical Journal*. DOI: 10.3847/1538-4357/ab7eb8.

Young, M. et al. (2009). "The fifth Data Realease of the Sloan Digital Sky Survey/XMM-Newton quasar survey". In: *The Astrophysical Journal Supplement Series*. DOI: 10.1088/0067-0049/183/1/17.

Zakamska, N. L. et al. (2019). "Host galaxies of high-redshift extremely red and obscured quasars". In: *Monthly Notices of the Royal Astronomical Society*. DOI: 10.1093/mnras/stz2071.

Zappacosta, L. et al. (2020). "The WISSH quasars project. VII. The impact of extreme radiative field in the accretion disc and X-ray corona interplay". In: *Astronomy & Astrophysics*. DOI: 10.1051/0004-6361/201937292.

— (2023). "HYPerluminous quasars at the Epoch of ReionizatION (HYPERION). A new regime for the X-ray nuclear properties of the first quasars". In: *arXiv e-prints*. DOI: 10.48550/arXiv.2305.02347.

Zubovas, K. and A. King (2012). "Clearing out a galaxy". In: *The Astrophysical Journal*. DOI: 10.1088/2041-8205/745/2/l34.